Microneedle Mediated Optical Detection of Glucose Concentration in Aqueous Solutions

Dean Nicholas MPharm

Faculty of Life and Health Sciences

Ulster University

Thesis Submitted for the Degree of

Doctor of Philosophy

Feb 2019

I confirm that the word count of this thesis is less than

100,000 words

Declaration

I hereby declare that with effect from the date on which the dissertation is deposited in the Library of the University of Ulster I permit the Librarian of the University to allow the dissertation to be copied in whole or in part without reference to me on the understanding that such authority applies to the provision of single copies made for study purposes or for inclusion within the stock of another library. This restriction does not apply to the copying or publication of the title and abstract of the dissertation.

IT IS A CONDITION OF USE OF THIS DISSERTATION THAT ANYONE WHO CONSULTS IT MUST RECOGNISE THAT THE COPYRIGHT RESTS WITH THE AUTHOR AND THAT NO QUOTATION FROM THE DISSERTATION AND NO INFORMATION DERIVED FROM IT MAY BE PUBLISHED UNLESS THE SOURCE IS PROPERLY ACKNOWLEDGED

I declare that this thesis and the work presented in it are my own and have been generated by me as the result of my own research, with the exception of the aid of the mechanical workshop in Ulster University in the manufacture of centrifuge accessories and the aid of Dr. Dorian Dixon in axial load compression investigations.

Table of Contents

Table of Figures

7

14

Acknowledgements

Summary

The detection and quantification of biologically important blood analytes plays a crucial role in the screening, diagnosis and management of disease. However the extraction of blood using hypodermic needles brings with it a plethora of issues. Two million cases of needle stick injuries in healthcare staff occur annually and approximately 10% of adults have needle phobia. Microneedles (MNs) have demonstrated potential in the extraction of interstitial fluid (ISF) in a minimally invasive manner due to their short length, thus avoiding stimulating pain receptors in the skin. ISF contains many of the same analytes that are found in the blood including glucose, which is critical in the management of diabetes. However, a large proportion of diabetics do not measure their blood glucose levels as often as recommended due to the pain and inconvenience of conventional methods. Therefore, there is great potential for a minimally invasive MN based approach in the extraction and determination of the concentration of glucose within the ISF to increase patient compliance and mitigate the negative effects of chronic hyperglycaemia.

Chapter 1 discusses the history of blood diagnostics with a focus on the detection of hyperglycaemia in diabetes. The negative consequences of chronic hyperglycaemia and the issues with conventional blood glucose determination are discussed. The potential of MNs to overcome these issues through indirect measurement of blood analytes by sampling ISF is introduced. **Chapter 2** details the materials and methods used in the experimental chapters**.**

Hydrogel forming MNs made from crosslinked polymers have previously demonstrated their ability to withdraw ISF containing glucose in human studies. **Chapter 3** investigates improving the swelling capability of these hydrogel MNs by including sodium carbonate in the formulation. A colorimetric glucose sensor is developed based on glucose oxidase, horseradish peroxidase and a colour forming dye. This sensor is then interfaced with the hydrogel MNs, initially in a hydrogel backplate and successfully demonstrates a visually apparent colour change in response to the extraction of glucose in simulated ISF *in vitro*. The time taken for the

colour change to occur is substantially decreased by embedding the sensor in a paper based backplate and increasing the length of the MN projections.

Chapter 4 involves the fabrication of a single hollow MN device that can successfully withdraw simulated ISF extremely rapidly through capillary action. This device was then coupled to the paper based glucose sensor used in **Chapter 3.** A method to quantify the intensity of the colour change on the sensor backplate is developed and optimisation of the sensor to produce a linear colour change in response to glucose concentration is successfully carried out, thus increasing its potential as diagnostic point of care (POC) tool.

Chapter 5 addresses some of the limitations of the device in **Chapter 4** through the production of a single metal hollow MN device with a silicone housing that aids the flow of fluid from the MN tip and into the paper based sensor backplate through suction. The sensor backplate is also modified with an antioxidant to produce an "OFF-ON" signal response for the detection of hyperglycaemia within the simulated ISF.

Finally**, Chapter 6** contains the conclusions of the results chapters and discusses opportunities for further work.

Abbreviations

AA	Ascorbic acid
CAD	Computer Aided Design
ChromB	Blue Chromaticity
GMA	Glycidyl Methacrylate
GOx/HRP	Glucose Oxidase/Horseradish Peroxidase
H_2O_2	Hydrogen Peroxide
HA	Hyaluronic acid
MN	Microneedle
NICE	National Institute of Clinical Excellence
OCT	Optical Coherence Tomography
PBS	Phosphate Buffered Saline
PDMS	Poly(dimethylsiloxane)
PEG	Poly(ethylene glycol)
PMVE/MA	Poly(Methyl Vinyl Ether-co-Maleic Acid)
PMVE/MAH	Poly(Methyl Vinyl Ether-co-Maleic Anhydride)
POC	Point of Care
PVA	Poly(vinyl alcohol)
RTV	Room Temperature Vulcanising
SMBG	Self-monitoring of blood glucose
SLA	Stereolithographic
TEGDMA	Tri(ethylene glycol) dimethacrylate

TMB	3,3',5,5'-Tetramethylbenzidine
TPME	Tri(propylene glycol) methyl ether
TRIM	Tri(methylolpropane) trimethacrylate
VAS	Visual Analogue Scale

Chapter 1

1.0 Introduction

1.1 Prologue

Diagnosis and monitoring of disease through blood analysis is ubiquitous in modern healthcare, with the market value for global blood testing in 2015 being $51.5 billion[2]. Diabetes is an example of one disease in which frequent blood monitoring is essential for decreasing the long term negative effects such as cardiovascular disease and stroke as well as avoiding hypoglycaemia which can lead to coma and death. In 2013, self-monitoring of blood glucose (SMBG) using electronic personal glucometers was valued at $3.99 million[3].

Healthcare guidelines recommend SMBG four times daily in Type 1 diabetes and insulin dependent Type 2 diabetes, which can be increased up to ten times daily in periods of illness or poor control[4]. However, patient compliance is an issue with 40% of Type 1 diabetes performing less SMBG than recommended. This is partially due to the pain and inconvenience of blood sampling multiple times daily through the conventional method of using a lancet needle to obtain capillary blood on the fingertip.

Microneedles (MNs) are a minimally invasive alternative to conventional needles for sampling interstitial fluid (ISF), which has been shown to contain analyte concentrations that correlate well to plasma concentrations[5,6]. Therefore, MNs may provide a painless and blood-free method of measuring plasma glucose indirectly and replace capillary blood sampling in SMBG, thus increasing patient compliance while decreasing the healthcare burden resulting from the long term complications of hyperglycaemia.

Current advancements using MNs for sampling ISF has successfully demonstrated glucose responsive insulin delivery[7,8], as well as single readings of ISF glucose in animals[9] and humans[10]. However, these methods are currently restricted by long application times and the requirement of several processing steps post application to remove the ISF from the MNs and subsequent determination of the concentration

of glucose contained therein. This is time consuming, requires training and is therefore unsuitable for a patient Point-of-care (POC) device.

The work undertaken in this thesis focussed on the development of a MN based device designed to rapidly withdraw ISF and determine the concentration of glucose via an integrated colorimetric system. Such an approach would enable the potential development of a POC device that enables the user to obtain glucose levels within the ISF rapidly and without the need for external processing, with the primary goal of reducing the incidence of hyperglycaemia in diabetes.

1.2 Blood Diagnostics

The invention of the compound microscope enabled some of the first scientific investigations of blood components. The Dutch microscopist Jan Swammerdan described the presence of "red corpuscles" in 1658 (**Figure 1.1**) which are now understood to be erythrocytes or red blood cells[11]. It was not until over 150 years later in 1843 that leukocytes or white blood cells were first reported by Gabriel Andral, a French Professor of Medicine, who linked abnormalities in the quantity and morphology of the cells to disease[12]. By the 1880s, microbiologists had isolated bacteria from the blood of patients suffering from tuberculosis, cholera, typhoid and diphtheria, isolating the organisms responsible for causing disease with the highest global mortality rates at that time. However, the antibiotic agents necessary to treat these bacterial infections would not be discovered for another 40 years.
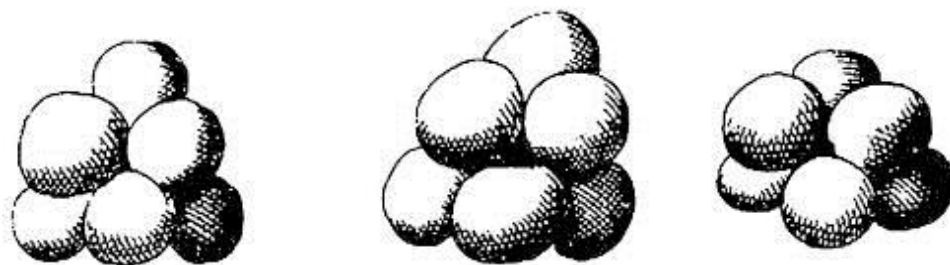
Figure 1.1: Illustration of "red corpuscles" of blood by van Leeuwenhoek in 1695, acquaintance of Swammerdan. Reproduced from Haju et al.[13]

During the early 20th Century, analytical techniques to identify and quantify chemical entities within the urine and blood were developed by clinical chemists. Major strides made by Otto Folin between 1904 and 1922 allowed the quantification of urea, creatinine, phosphorous and chloride amongst others from the urine alongside methods to quantify ammonia and creatinine concentrations in the blood. By 1920, venepuncture was in widespread use throughout the world of medicine and clinical chemistry in order to obtain blood from patients for analysis. In 1930, Kay reported the first clinical laboratory method for the determination of the enzyme alkaline phosphatase[14] and linked its elevated presence in the blood to Osteitis deformans, known as Paget disease in modern medicine, which is characterised by abnormal bone growth due to excessive breakdown and formation of bone tissue. This spurred investigations into enzymology in clinical laboratories and soon after Cherry and Crandall had developed a method to quantify lipase activity in blood serum[15].

Measurement of the common metal cations such as sodium, potassium, calcium and magnesium within biological fluids was aided by the introduction of the flame photometer in the 1940s[16]. Relying on the relatively low excitation energies of the Group I and II alkali and alkali earth metals, a flame was used to provide sufficient thermal energy to an atomised sample of metal ions in order to raise an electron from a lower energy state to a raised excited state[17]. Electrons in the excited state are unstable over time therefore they will return to a lower energy state and the subsequent energy released is emitted as visible radiation that can be measured and the concentration of the metal cations within the sample can be quantified.
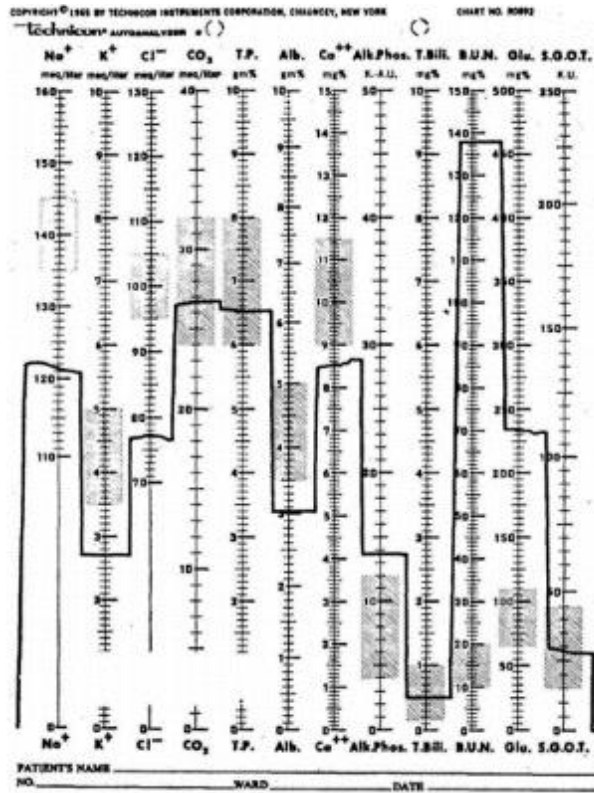
Figure 1.2: Results report of Technicon SMA-12 AutoAnalyzer available in 1966 showing multiple analyte measurements and reference values simultaneously. Reproduced from Peitzman et al.[16]

While the flame photometer provided a more convenient and less costly alternative to quantify the electrolytes in the serum and urine than the previous methods available, which could take between 24 - 48 hours for a single measurement of sodium concentration in serum[18], integration of flame photometers to automated systems provided a revolution in biological electrolyte measurements in the form of the AutoAnalyzer manufactured by Technicon during the 1960s. The AutoAnalyzer allowed higher throughput of samples and provided a means of measuring multiple blood analytes simultaneously (**Figure 1.2**).

Modern clinical laboratories in hospitals are able to perform a plethora of blood tests in extremely high numbers due to advances in automated systems. Routine blood tests include the Basic Metabolic Panel (BMP) also known and Urea and Electrolytes and the Comprehensive Metabolic Panel (CMP).

The CMP has a total of fourteen analytes and provides information on blood sugar, blood proteins, kidney function, liver function, acid/base balance and electrolytes. **Table 1.1a and 1.1b** shows the range of analytes included in the CMP. In 2014, 230 million biochemistry and 47 million haematology laboratories tests were carried out by the NHS in the UK, incurring a cost of £415 million.[19]

Table 1.1a Analytes included in CMP and possible indications causing measurements outside of reference ranges.[20]

Analyte	Elevated Levels Indicate	Decreased Levels Indicate
Glucose	Diabetes mellitus, adrenal hyperfunction	Excess insulin, hepatic failure, starvation, adrenal hypofunction
Calcium	Thyroid and parathyroid hyperfunction, bone disorders, elevated vitamin D, cancers.	Renal failure, parathyroid hypofunction, vitamin D deficiency
Sodium	Dehydration, adrenal hyperfunction, renal dysfunction, diabetes insipidus.	Renal failure, diuretics, overhydration, renal, hepatic and heart failure.
Potassium	Renal failure, adrenal hypofunction, acid-base imbalance	Diuretics, diarrhoea, vomiting, adrenal hypofunction, acid-base imbalance
Chloride	Acid-base imbalance from GI, adrenal and renal disease	Renal disease, adrenal hyperfunction, acid-base imbalance
Albumin	n/a	Hepatic failure, renal failure, malnutrition

Table 1.1b Analytes included in CMP and possible indications causing measurements outside of reference ranges.[20]

Analyte	Elevated Levels Indicate	Decreased Levels Indicate
Total Protein	Chronic infection, inflammation, multiple myeloma	Malnutrition, hepatic or renal failure.
Blood Urea Nitrogen (BUN)	Renal failure, dehydration, GI haemorrhage.	Hepatic failure
Creatinine	Renal failure, dehydration	n/a
Alkaline Phosphatase	Hepatic disease, heart failure, parathyroid hyperfunction	n/a
Alanine Amino Transferase	Hepatic disease	n/a
Aspartate Amino Transferase	Hepatic disease, heart injury, muscle injury	n/a
Total Bilirubin	Hepatic disease, haemolytic anaemia	n/a
Total CO_2	Acid-base imbalance	Acid-base imbalance

1.3 Diabetes

Diabetes mellitus is a chronic condition that involves the dysfunctional regulation of glucose in the bloodstream. The prevalence of diabetes in adults has increased globally since 1980, when 4.7% of the population were diagnosed, to 8.5% of the population being diagnosed in 2014[21]. Across the UK, the average prevalence of diabetes in adults was 6.0% in 2013. (**Table 1.2**).

Table 1.2: Prevalence of diabetes in UK in 2013 broken down by country.[22]

Country	Prevalence	Diabetic Population
England	6.0%	2,703,044
Northern Ireland	5.3%	79,072
Scotland	5.2%	252,599
Wales	6.7%	173,299

Diabetes can be categorised into several different types according to its aetiology. Type 1 diabetes, previously known as insulin dependent or childhood onset diabetes, is characterised by a significantly decreased or a total lack of insulin production by the pancreas. This is caused by a T cell dependent autoimmune response by the body that leads to infiltration of the pancreas by $CD4^+$, CD8 and $CD11c^+$ T cells[23] and subsequent destruction of islet β cells that are responsible for endogenous insulin production[24]. If left untreated, Type 1 diabetics exhibit symptoms such as excessive thirst and urination, constant hunger, weight loss, and vision changes which are all due to chronic hyperglycaemia and ketoacidosis[25]. Without endogenous insulin production, Type 1 diabetics require exogenous insulin replacement therapy to survive as chronic hyperglycaemia will lead to organ failure, coma and death[26].

The exact cause of Type 1 diabetes is not fully understood[27], although it has been linked to inherited genetic factors. However, studies of identical twins with Type 1 diabetes has provided evidence that susceptibility to the disease is not wholly genetic indicating that environmental factors also play a role in the pathogenesis of the disease[28]. Among the environmental factors influencing the onset of Type 1 diabetes are modulation of the intestinal microbiota in birth by caesarean section, antibiotic

use in early stage life[29], viral infection with enterovirus[30], higher birth weight and increased weight gain between the ages of 12 – 18 months[31].

Accounting for approximately 90% of global cases, Type 2 diabetes is the most prevalent form of the disease[32]. Unlike Type 1 disease, the pancreatic islet cells remain functional but they fail to compensate for the insulin resistance of the body that is caused by increased body mass and adipose tissue[33] as well as the inflammatory response to hyperglycaemia[34]. This failure to produce enough endogenous insulin, coupled with decreased insulin sensitivity, leads to chronic hyperglycaemia that can remain undetected for years until the complications of Type 2 diabetes manifest themselves.

Intermediate conditions such as impaired glucose tolerance and impaired fasting glycaemia are diagnosed according to the degree of hyperglycaemia found in the bloodstream and while they are reversible, patients can progress into the overt chronic hyperglycaemia of diabetes, especially Type 2.

Gestational diabetes occurs in pregnant women who have not previously had diabetes but are found to have hyperglycaemia after routine screening, normally at 28 weeks into the pregnancy[35]. While it can be a temporary condition that lasts throughout the pregnancy, it does increase the long term risk of Type 2 diabetes. A meta-analysis of 20 studies carried out on a total of 675,000 pregnant women found that women with gestational diagnosed diabetes had a 7.43 fold increased risk (CI 4.79-11.51) of a subsequent diagnosis of Type 2 diabetes at a later point in life compared to women without gestational diabetes[36].

1.4 Hyperglycaemia

Chronic hyperglycaemia causes damage to the vasculature tissue. It has been suggested that the mechanism of this damage is caused by the overproduction of reactive oxygen species (ROS) and superoxides by the mitochondria in response to hyperglycaemia[37] that influences five major metabolic pathways. These are an increased flux of glucose and other sugars through the polyol pathway, increased intracellular formation of advanced glycation end-products (AGEs), increased expression of the receptor for AGEs and its activating ligands, activation of protein

kinase C isoforms and over activity of the hexosamine pathway[38]. Through these mechanisms, the action of intracellular ROS is increased, which can cause defective angiogenesis in response to ischemia and activate pro-inflammatory pathways, leading long term vascular damage[39].

The deleterious effect of hyperglycaemia are commonly separated into microvascular and macrovascular complications. Microvascular complications include diabetic retinopathy, nephropathy and neuropathy. Macrovascular damage leads to coronary artery disease, peripheral artery disease and stroke.

1.4.1 Microvascular Complications

1.4.1.1 Diabetic Retinopathy

Almost all Type 1 diabetics and 58% of Type 2 diabetics develop retinopathy within twenty years of diagnosis[40]. The extent of the retinopathy is correlated to the severity of hyperglycaemia and the presence of hypertension[41]. Early stage background retinopathy is indicated by the presence of microaneurysms and small haemorrhages of the blood vessels in the middle layers of the retina[42]. More severe proliferative retinopathy involves pathological angiogenesis on the surface of the retina and can lead to vitreous haemorrhage and retinal detachment. Vision loss occurs in 25 – 35% of high risk cases of proliferative retinopathy[43].

1.4.1.2 Diabetic Nephropathy

Through a combination of hyperglycaemia and hypertension, progressive loss of renal function is observed in 30 – 40% of the diabetic population 25 years after diagnosis[44]. Atrophy of the renal vasculature caused by thickening of the basement membrane, interstitial fibrosis and arteriosclerosis leads to microalbuminuria which is the presence of elevated levels of albumin in the urine, indicating early stage renal damage. Approximately 20% of patients progress to more serious proteinuric nephropathy which has a poor prognosis that leads to end stage renal failure and cardiac disease[45].

1.4.1.3 Diabetic Neuropathy

Peripheral nerve dysfunction affects approximately 50% of the diabetic population. In distal sensory neuropathy, the most common form that accounts for 80% of

diabetic neuropathy cases, typical symptoms experienced include tingling, burning, "electric" pain and numbness[46]. This loss of the protective sensation through numbness can increase the risk of peripheral limb injury and infection and can lead to diabetic foot ulceration[47].

Diabetic foot ulcers are caused by a combination of neuropathy, peripheral vascular disease and minor trauma[48] and are the cause of 85% of lower extremity amputations in non-traumatic cases[49].

1.4.2 Macrovascular Complications

While there is strong evidence to suggest that intensive blood glucose control decreases the risk of microvascular complications, the evidence that macrovascular complications such as stroke and cardiovascular disease are decreased through strict glucose control is still debated[50]. However, the 10 year follow up on the initial UKPDS trial in which Type 2 diabetics received intensive glucose lowering therapy compared to conventional therapy[51] has shown that better glucose control can decrease the risk of myocardial infarction by 15% (p = 0.01) and all-cause mortality by 13% (p = 0.007).

The underlying cause of the macrovascular complications involves the increased risk of atherosclerosis, which is the build-up of a plaque consisting of lipids and fibrous elements in the arteries[52]. This plaque is a result of chronic inflammation of the epithelial cells of the vasculature causing an immune response involving monocytes, T-lymphocytes, macrophages and mast cells[53] and ultimately leads to the narrowing of the blood vessels and the propensity for thrombotic formation[54]. Additionally, evidence suggests that there is increased platelet adhesion and increased coagulability in Type 2 diabetics[55]. This further exacerbates the risk of thrombosis formation, cardiovascular events and stroke. In fact, a study on a Finnish diabetic population concluded that the risk of myocardial infarction amongst the diabetic population was on par with those who had previously experienced myocardial infarction[56].

1.5 Glycaemic Monitoring Requirements

Single measurements and measurements of long term blood glucose levels are routinely monitored in medical settings by healthcare professionals and at home by diabetics. In the clinic, the levels of glycated haemoglobin is measured to give an indication of the glucose control over a prolonged time period. The measurement of glycated haemoglobin is used to determine the average levels of glucose in the blood over the previous two to three months[57] and is less prone to be affected by short term postprandial fluctuations. A component of the haemoglobin (Hb A1c) present in erythrocytes, reacts with glucose in the plasma wherein the aldehyde group on glucose covalently bonds to the free amine groups present on the peptide chain of the Hb A1c forming a Schiff base[58]. Unlike other specific glycosylation reactions of peptides that serve to functionalise them for specific roles, this glycosylation is not catalysed enzymatically and, therefore, the rate of reaction is determined by the concentration of free glucose in the plasma over the entire course of an erythrocyte's lifespan (approx. 120 days[59]). In this way, an indication of the average glucose concentration over the previous 3-4 months can be obtained. The National Institute of Clinical Excellence (NICE) currently recommends that HbA1c should be measured every three to six months in persons with Type 1 diabetes and every six months in persons with Type 2 diabetes[4]. The target concentration is 48mmol/mol in most diabetics, however, it can vary depending on the treatment regime[60]. In general, a concentration of >75mmol/mol is a sign of hyperglycaemia over a prolonged period and would result in a patient being recommended to carry out SMBG up to ten times per day to achieve control[4].

The current guidelines by NICE recommend people living with Type 1 diabetes to routinely undertake SMBG four times per day, however, it is recommended to check as often as ten times per day in periods of poor glucose control, exercise or illness.[61] In Type 2 diabetes, glucose monitoring is a requirement if the person is taking hypoglycaemic agents such as sulphonylureas or insulin. Such pharmacological agents are given as second or third line interventions when adequate glucose control cannot be achieved through lifestyle changes or the use of a first line agent such as Metformin.

SMBG by people living with diabetes is commonly performed using an electronic glucose meter to obtain a reading of the concentration of glucose within the blood at that single point in time. There are many different types of glucose monitors available to the public, however, most systems are comprised of a handheld device with a display screen. Propriety test strips are inserted into the device and a sample of blood is applied to the test strip. The plasma component of the blood then diffuses through an enzyme and electroactive chemical reagent layer that coats an electrode. The glucose present in the blood is oxidised by the reagents to produce an electrical current which is used to calculate the concentration of glucose via amperometric means. Although the exact mechanisms vary between proprietary devices, in most cases an electrical current is produced proportional to the amount of glucose present in the sample via the reduction of an electroactive chemical such as ferricyanide[62]. When glucose is oxidised by enzymes such as glucose oxidase[63], glucose dehydrogenase or hexokinase[64,65], the ferricyanide present in the strip is reduced to ferricyanide and the resulting change in electric potential is measured by the electrode. This change is used to calculate the concentration of glucose and is displayed to the user.

The most common method to obtain this blood sample is through the use of a lancet needle that can be up to 6 mm long. The needle is inserted into the fingertip via the spring-loaded mechanism and a small volume of capillary blood is presented to the sample inlet on each test strip. This method has been reported to be inconvenient and painful[66-68] and leads to compliance issues in the diabetic population. 40% of Type 1 diabetics do not undertake SMBG as often as recommended[69] and this can have negative consequences due to the complications of hyperglycaemia described in **Section 1.4.** Minimally invasive methods to determine the concentration of glucose within the plasma through the measurement of ISF have been proposed as alternatives[70,71] which seek to increase the convenience and decrease the pain associated with SMBG, leading to better compliance and long term outcomes for people living with diabetes.

1.6 Microneedles

Microneedles (MNs) are an intradermal technology first proposed in in 1976[72] for the purpose of enhancing drug delivery through the skin. The US patent granted to Gerstel and Place states that through the aid of a plurality of puncturing projections a drug could be percutaneously delivered from a reservoir through the *stratum corneum* and into the epidermis (**Figure 1.3**).
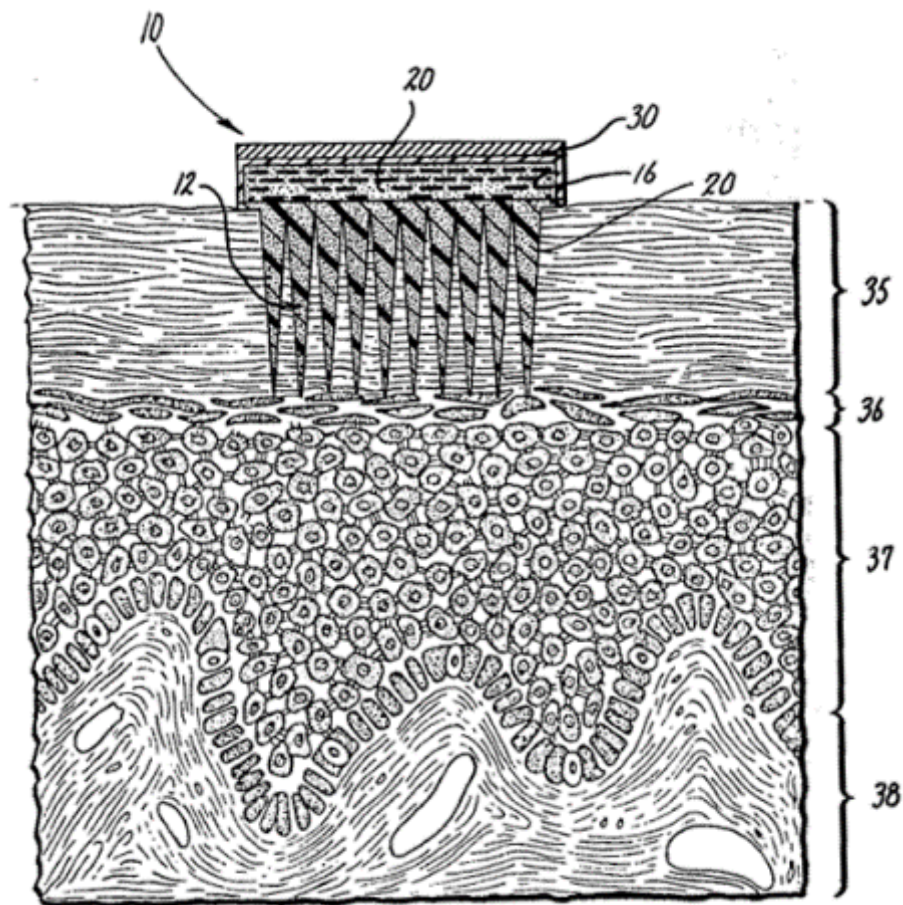
Figure 1.3: Original diagram from Gerstel and Place 1976 patent suggesting use of MN as a drug delivery device, showing penetration through the *stratum corneum*.

However, the technology required to produce the first proof-of-concept device that was capable of drug delivery only became widely available in the late 1990's with the rise of microelectronics industry. In 1998, the first publication using MNs to deliver a model hydrophilic compound, calcein, through human skin was published by Henry et. al[73].

There have been many subsequent iterations of MNs following this initial application by Henry et al., however, MNs can broadly be described as consisting of one or more needle-like structures projecting from a supporting baseplate. The needles are generally between the length of 25 µm and 2000 µm[74] and can be produced in a range of 3D geometries including conical, cylindrical, pyramidal and various 2D planar designs. Additionally, MNs can be fabricated with a central hollow channel through which fluid can pass, similar to a hypodermic needle.

One of the major benefits of MNs are their minimally invasive nature due to their small dimensions. The application of MNs is commonly reported to cause little or no pain compared to conventional hypodermic needles due to their short length and narrow profile, thus avoiding the stimulation of dermal nociceptors[75]. This will be discussed further in **Section 1.9.**

1.7 Classification of MNs

Depending on the shape and design, MNs can be classified into a number of different categories: solid MNs, coated MNs, dissolving MNs, hollow MNs, and hydrogel forming MNs, each of which will be discussed below.

1.7.1 Solid MNs

Solid MNs can be used as a "pre-treatment" method for skin in order to create pores through which a target compound can passively diffuse into the epidermis for local action or systemic absorption[76].

Henry et al. produced the first solid MN array from silicon in order to enhance the skin permeability of a model fluorescent compound calcein as previously mentioned. By mounting human epidermis skin on Franz diffusion cells the transport of the fluorescent dye from the donor compartment to the receiver compartment after one hour was measured by fluorescent spectroscopy. The ability of the MNs to enhance the permeability of the epidermis was then shown by the application of a solid silicon 20 x 20 MN array with conical MNs approximately 150 µm in length (**Figure 1.4**) for various lengths of time.
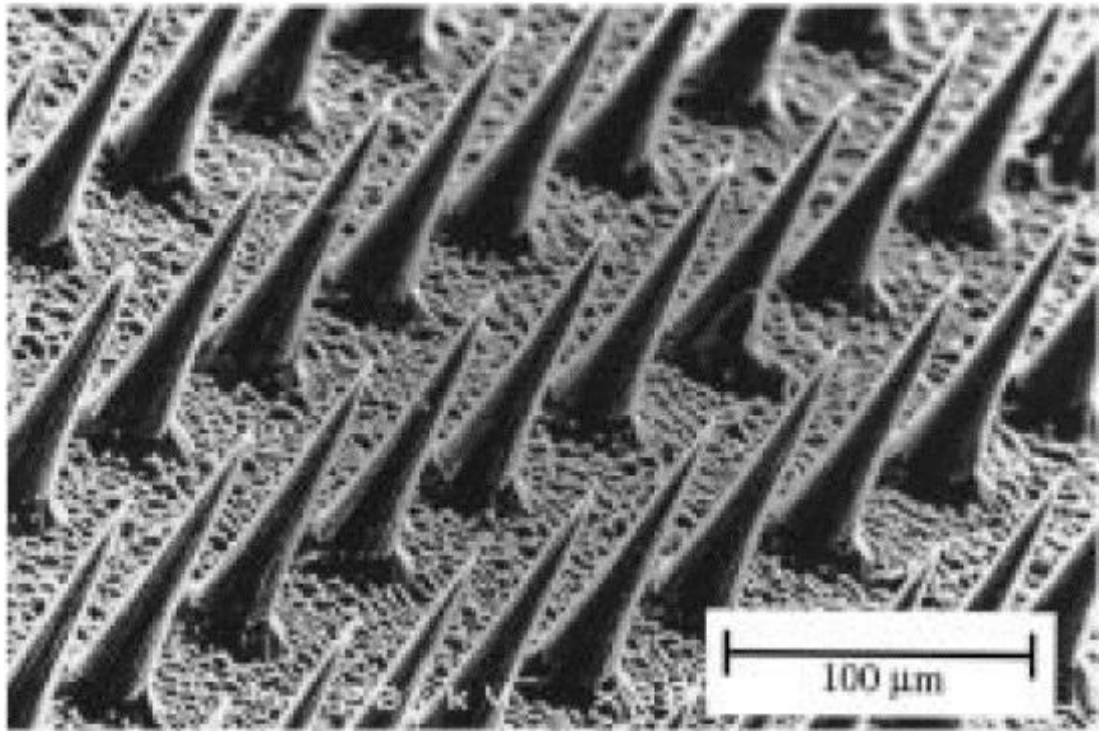
Figure 1.4: Scanning electron microscope (SEM) images of 20 x 20 solid silicon MN array fabricated by Henry et al.

It was found that leaving the MN array in place on the epidermis, the rate of transport of the calcein was approximately three orders of magnitude greater than the untreated epidermis. When the MN array was applied for ten seconds and then removed, the rate of transport was increased by four orders of magnitude and subsequently it was shown that by leaving the MN applied for one hour before removal, the transport was increased by a further order of magnitude. The suggested mechanism of this increase in permeability was due to micropores formed in the epidermis by the MN arrays, which was evidenced by examination of the skin sample by light microscopy after MN application. Micropores approximately 1 µm in diameter were found penetrating the epidermis, thus bypassing the main barrier to drug diffusion - the *stratum corneum*.

McAllister et al.[77] have demonstrated fabrication techniques to produce solid MNs from a range of materials including silicon, metal, polymers and glass (**Figure 1.5**). Reactive ion etching of a silicon substrate was used to produce large arrays of MNs

150 µm in length, while metal arrays were fabricated via electroplating of Ni or NiFe on to silicon moulds to produce MNs 120 µm in height. Polyglycolic acid and polylactic acid MNs were fabricated using polydimethylsiloxane (PDMS) negative moulds and glass MNs were produced using conventional glass micropipette pulling apparatus.
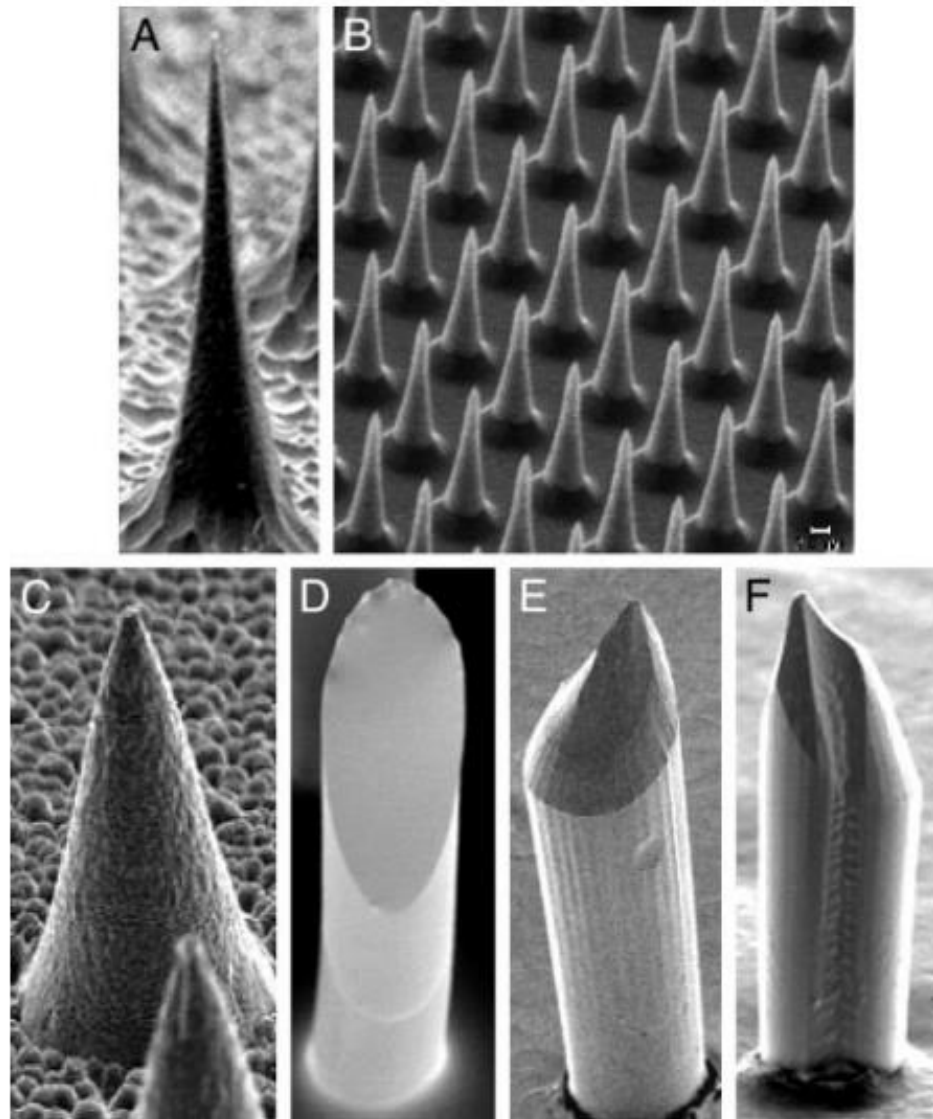
Figure 1.5: SEM images of MNs of different morphologies fabricated from various materials - (A-B) Silicon (C) Metal (D-F) Polylactic and polyglycolic acid

Oh et al.[78] have investigated the use of solid MNs alongside the application of a drug loaded hydrogel patch in order to deliver calcein through excised rat skin utilising a similar *in vitro* Franz diffusion set up as Henry et al. MN arrays manufactured from polycarbonate were produced by first creating so called "in-plane" MNs which were

then grouped together to create 2D arrays of MNs, or "out-of-plane" MNs of various lengths and densities (**Figure 1.6**).
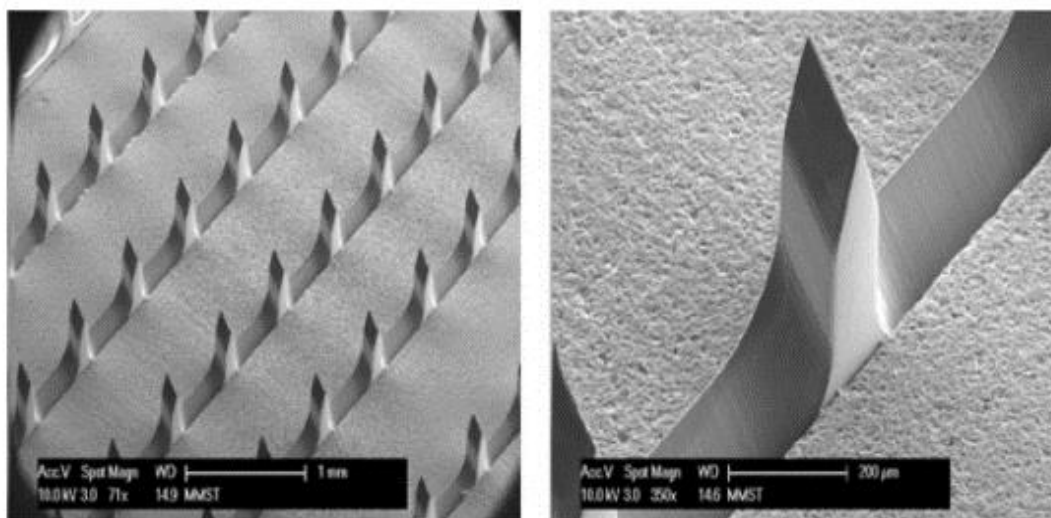
Figure 1.6: Out-of-plane MN array (left) created from grouping several in-plane MNs fabricated from polycarbonate. Magnified image of single MN projection from array (right).

The arrays comprised of 200 μm and 500 μm long projections with densities of 45, 99 and 154 MNs/cm^2. The hydrogel patch loaded with 1mM calcein was formulated from carbopol 940 and triethanolamine. The investigators determined that the delivery rate of the target compound was positively affected by increased MN length and density, with the greatest rate of diffusion observed with 500 μm MNs with a density of 154 MNs/cm^2.

This approach of pre-treating the skin with solid MNs and then placing a drug loaded patch over the area has been termed the "poke and patch" method and has been successfully demonstrated in human subjects to enhance transdermal delivery of hydrophilic drug molecules that would otherwise not permeate through the hydrophobic *stratum corneum*. Wermeling et al.[79] carried out a small scale human trial (six treated and three control subjects) to demonstrate the delivery of Naltrexone, an opioid receptor antagonist for the treatment of opiate and alcohol dependence, using the poke and patch method.

Arrays consisting of 50 stainless steel MNs (**Figure 1.7**) were inserted into the skin of the subjects across four patch sites for a few seconds before removal. Subsequently, adhesive patches containing (% w/w) 16% Naltrexone HCl, sterile water for injection (20.25%), propylene glycol (60.75% USP), 2% hydroxyethyl cellulose and 1% benzyl alcohol were placed over the application sites for the study duration. Steady state plasma concentrations of Naltrexone were detected in the treatment groups after 2 hours and this was maintained for at least 48 hours, whereas no detectable quantity of drug in the plasma was found in the control group that did not have skin pre-treatment.
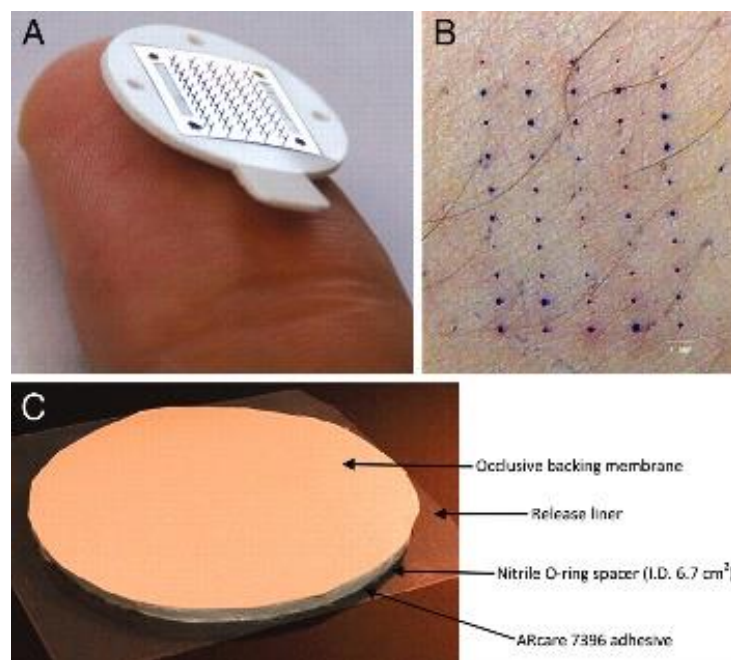
Figure 1.7: (A) MN array of 50 stainless steel projections for pre-treatment of skin. (B) Resultant micropores created by application of MN array on human volunteers visualised with gentian violet (C) Adhesive drug loaded patch for subsequent application to pre-treated skin

1.7.2 Coated MNs

The poke and patch method of using solid MN arrays to create transient micropores in the skin followed by drug application has been shown as a feasible method to enhance the transdermal delivery of otherwise skin impermeable hydrophilic drugs. However, it is inherently inconvenient for the patient as it requires two distinct steps, which could negatively affect patient compliance and increase the risk of improper use.

Coating MNs with the target drug or material that is to be delivered circumvents the need for two steps, as the target compound is delivered to the skin during the MN application step. However, due to the small surface area of MN arrays the total amount of target compound that can be delivered is dependent on the array size. Therefore, the type of payload suitable for coated MN arrays is limited to extremely potent materials where the clinically effective dose is extremely low. Suitable payloads include vaccines[80,81], steroids[82], peptides[83] and genetic material[84,85].

1.7.3 Dissolvable MNs

MN arrays composed of water soluble polymers have been used as drug delivery vehicles via incorporation of the target compound into the polymeric matrix of the MN. When the MN is applied, the ISF in the epidermis dissolves the polymer and the target compound is released from the MN and into the skin. From there the target compound can exert its effect locally or can be absorbed into the blood stream for systemic effect. Some example materials include carboxymethylcellulose[86,87], maltose[88], chitosan[89] and poly(vinyl alcohol) (PVA)[90,91].

As the objective of these devices is for the polymer matrix to dissolve in the skin, it is necessary for the polymer material to be biocompatible. Hyaluronic acid (HA) and poly(vinylpyrrolidone) (PVP) which are approved for use by the Food and Drug Administration have been used to fabricate dissolvable MNs containing gentamicin[92], an aminoglycoside typically used to treat severe gram negative infections[93]. The MNs consisted of a 19 x 19 arrays of needles, 500 μm in height (**Figure 1.8)** and exhibited complete dissolution 5 mins after insertion into neonatal porcine skin. In a murine animal model, successful delivery of gentamicin was observed with the maximum plasma levels achieved between one and six hours post application.
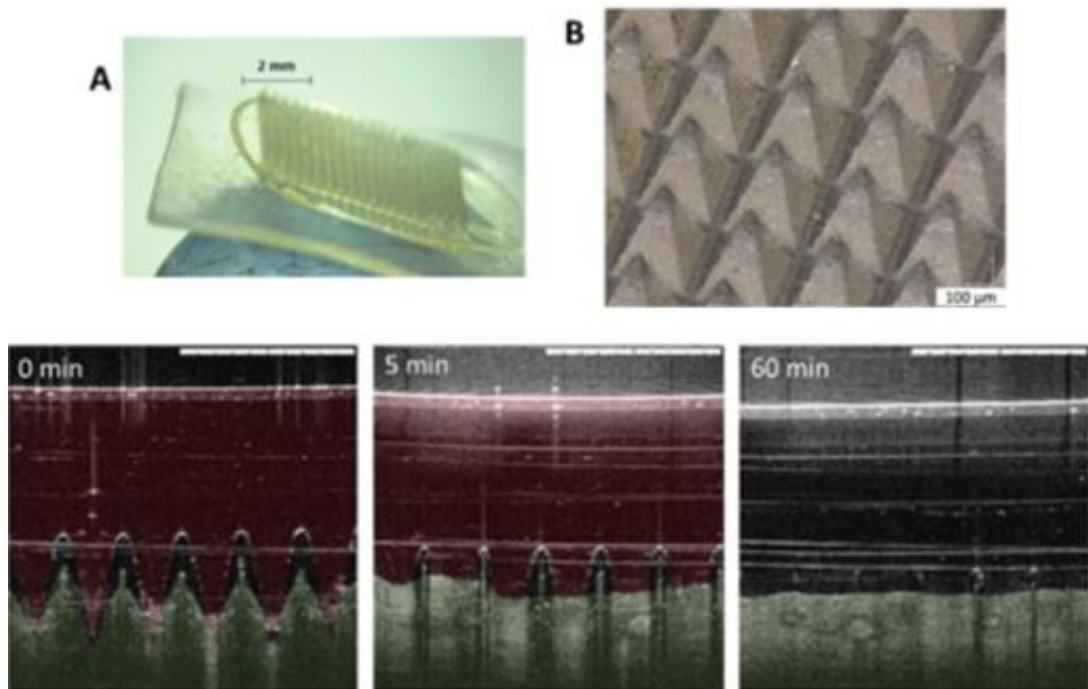
Figure 1.8: (Above) Photograph of dissolvable MN arrays containing gentamicin (Below) OCT images of insertion and subsequent dissolution of 19 x 19 MN array in neonatal porcine skin. Reproduced from González-Vázquez et al.[91]

The delivery of insulin has also been investigated using dissolvable MNs[94]. A formulation composed of starch and gelatin was used to encapsulate insulin before formation into MN arrays that were robust enough to withstand penetration into porcine skin *in vitro*. The hypoglycaemic effect of the insulin delivered from the MNs was observed to be similar to a subcutaneous injection of the insulin in a rat animal model.

1.7.4 Hydrogel forming MNs

Swellable hydrogels can be prepared from polymers that are initially water soluble but when crosslinked become water insoluble. Rather than dissolving, the polymer will swell with fluid that is drawn into the structure by hydrophilic or ionised groups such as hydroxyl (−OH), carboxylic (−COOH), amine (-NH$_2$) and amidic (−CONH-) residues present in the polymer chains[95]. Swellable hydrogels that are used in MN manufacture generally consist of a crosslinked polymer network that forms a mechanically robust structure when in the dry state (xerogel) which then rapidly

imbibes fluid and swells in volume when placed in contact with aqueous solutions. In this way, hydrogel MNs can be used to pierce through the outermost layers of the skin and swell with ISF. This provides a path for any drugs loaded within the MN to diffuse into the skin and exert their effect locally or be delivered systemically.

For drug delivery purposes a number of different polymers have been used to create hydrogel MNs. Arrays consisting of PVA crosslinked by freeze thaw cycles[96] has successfully demonstrated *in vitro* delivery of insulin in a Franz diffusion cell experiment with porcine skin. Approximately 50% of the insulin loaded into the MNs was released over 6 h. The swelling of the MN with ISF can be seen in **Figure 1.9** wherein blank crosslinked PVA hydrogel MNs were inserted into the arms of human volunteers for up to 3 hours.
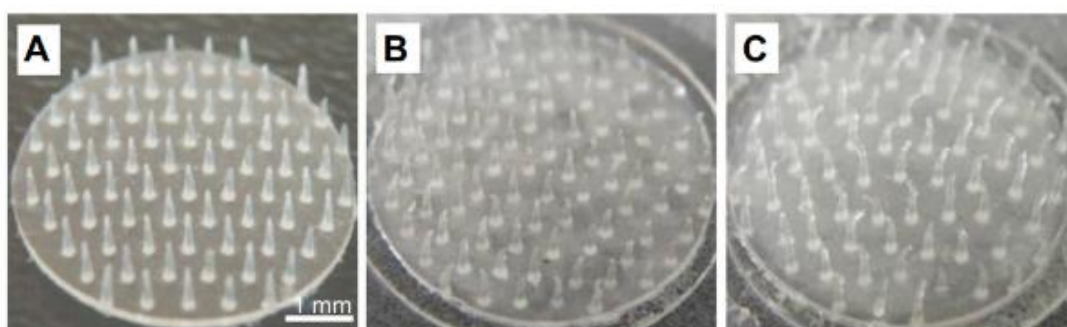
Figure 1.9: PVA MN arrays fabricated from crosslinked PVA swelling due to insertion into human skin (A) Before insertion (B) 1 h after insertion (C) 3 h after insertion

1.8 Anatomy of the skin

The skin can be stratified into two layers - the epidermis and the dermis, which are delineated by the epidermal-dermal junction. Below the dermis exists a layer of subcutaneous fatty tissue known as the panniculus adiposus which is separated from the deeper regions of the rest of the body by a layer of striated muscle known as the *panniculus carnosus*. The main anatomical features of the skin are conserved across the entire surface of the body however the glabrous skin present on the soles of the feet and the palms of the hands has a thicker epidermis, is devoid of hair follicles and sebaceous glands and has encapsulated sensory organs in the dermis[97]. The non-glabrous skin, or hairy skin, that is present on the rest of the body, is marked by the

presence of hair follicles and sebaceous glands. Sweat glands are present on all skin surfaces at a density ranging between 100 - 400 glands / cm^2.

1.8.1 Epidermis

The most superficial skin layer, the epidermis, consists almost entirely of keratinocytes which produce numerous fibrous proteins named keratins which add mechanical rigidity to the cells as well as long chain saccharides named glycosaminoglycans[98]. Keratinocytes form 95% of the cellular mass of the epidermis and originate from the basement membrane at the epidermal-dermal junction. Initially keratinocytes are formed attached to the basement membrane, however, as they mature they migrate progressively toward the surface of the skin and as such the epidermal keratinocytes are grouped into four distinct layers – the *stratum basale, stratum spinosum, stratum granulosum, stratum lucidum* and the *stratum corneum* (**Figure 1.10**). The layers are differentiated from each other by the morphology and function of the keratinocytes which are in different stages of maturity.
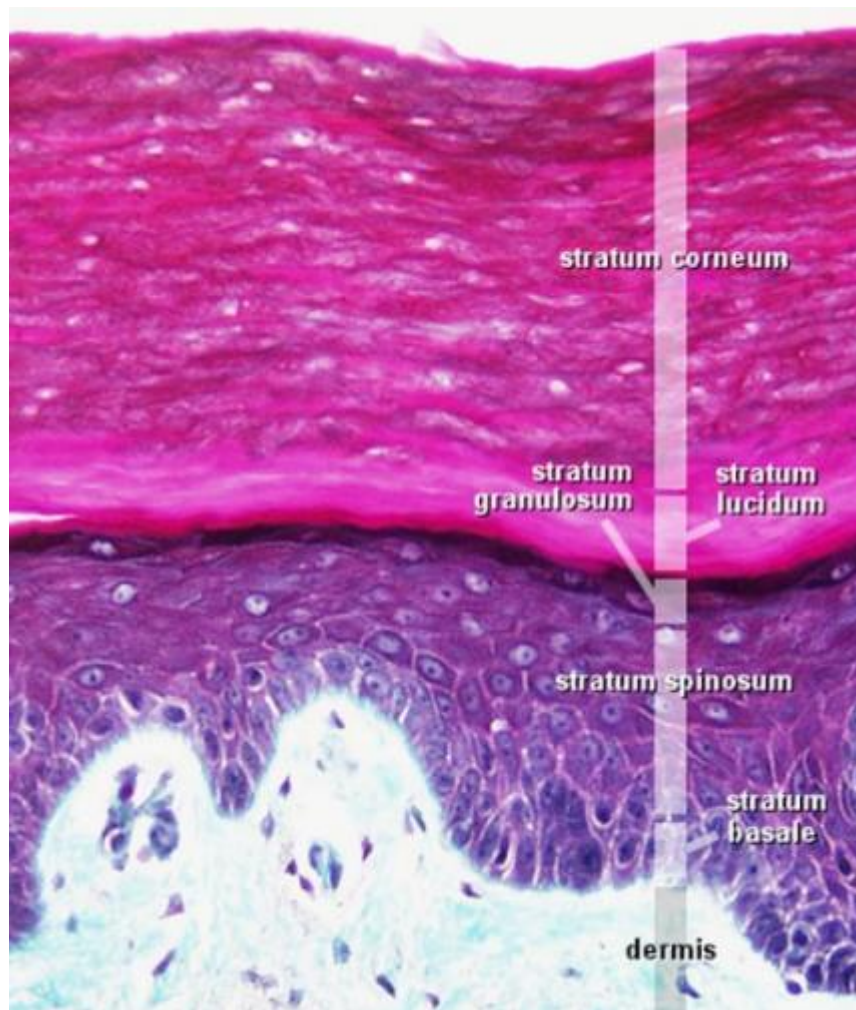
Figure 1.10: Human skin histological image showing layers of epidermis and dermis[99]

The *stratum basale* is the deepest later of the epidermis and largely consists of a single layer of stem cell keratinocytes at the epidermal-dermal junction[100], however, it may be two or three cells thick in glabrous or hyperproliferative skin[97]. Mitosis of the keratinocytes in this layer produces daughter cells, of which half migrate toward the skin surface and the other half remain at the basement membrane. As the keratinocytes move into the *stratum spinosum* they lose the ability to divide and begin to join together through intracellular bridges to form desmosomes that add strength and flexibility to the skin[101]. Cessation of metabolic activity and apoptosis of the keratinocytes is observed in the *stratum granulosum* leading to an almost complete keratinisation of the cells[102]. The *stratum corneum* is the outermost layer of the epidermis and is comprised of dead, flattened keratinocytes that are each attached to its neighbour forming a barrier against external stimuli such as chemicals,

heat and microorganisms. The entire process of the migration of the keratinocytes from the *stratum basale* to the *stratum corneum* takes approximately 28 days in a 0.1 mm epidermis[103]. The remaining 5% of cells in the epidermis consist of melanocytes, Langerhans' cells and Merkel cells. Melanocytes give the skin its pigmentation through the production of melanin. Langerhans' cells are dendritic immune cells that present antigens to naïve T cells in the lymph nodes in order to trigger an immune response. They also play a role in hypersensitivity of the skin and chronic inflammatory conditions such as eczema and psoriasis[104]. The function of Merkel cells is not universally agreed upon[105]. Conventionally thought to play a role in mechanoreception, as they can be found associated with nerve terminals, more recent research has shown that not all Merkel cells are in contact with neurons and it has been suggested that they may serve as a diffuse endocrine system throughout the skin[106].

1.8.2 Dermis

The dermis is situated below the epidermis and is mainly composed of polysaccharides and proteins. Fibroblasts, mast cells, histiocytes, monocytes and macrophages are all present in the dermis[107]. The proteins within the dermis are comprised mainly of collagen and elastin which are produced by the fibroblasts. In fact, 70% of the dry weight of dermis is comprised from collagen which increases the tensile strength of the skin. Elastin is much more flexible and aids the skin to return to its natural shape after stretching. The dermis is classified into two layers: the papillary and the reticular layer (**Figure 1.11**).
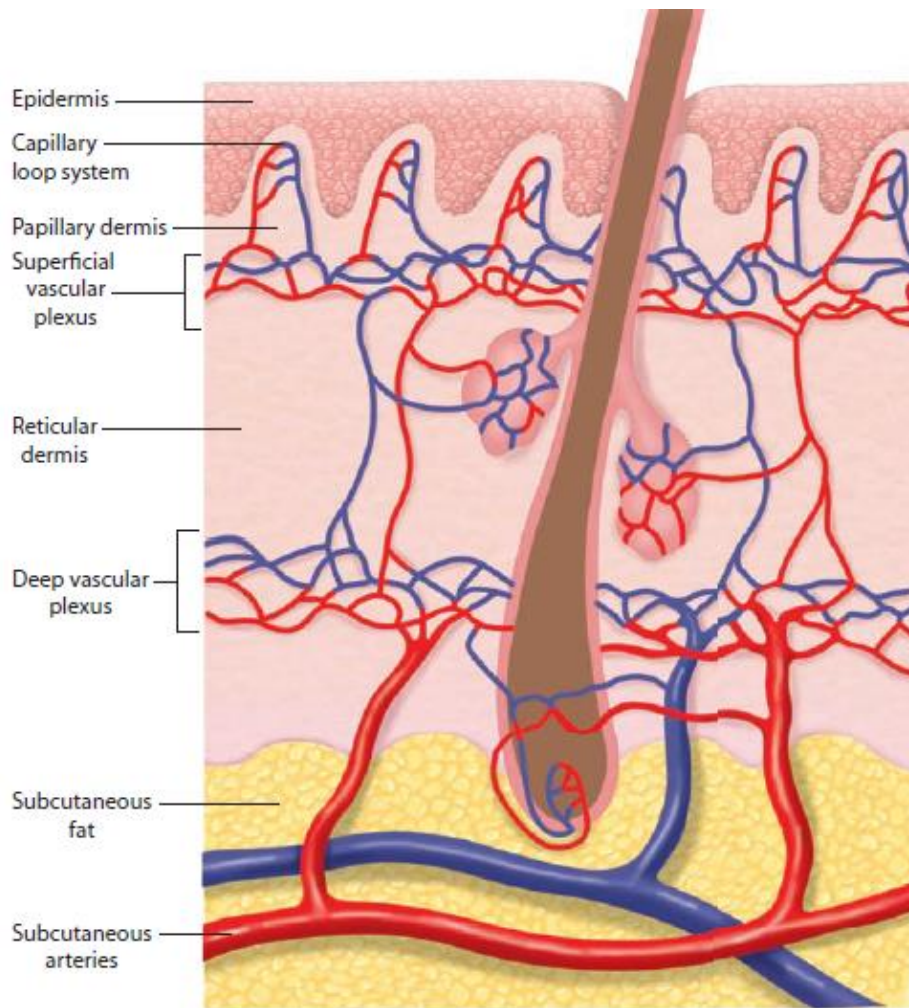
Figure 1.11: Vasculature organisation of the dermis. Subcutaneous vessels reach into the dermal layer to form the deep vascular plexus and superficial vascular plexus[108]

The papillary layer is closest to the epidermal-dermal junction and contains less neurons and capillaries, while the reticular layer is deeper and contains more connective tissue and blood capillaries. Larger blood vessels in the subcutaneous fat layer below the dermis branch off into the reticular dermis and form a network of capillaries known as the deep vascular plexus[109] which supplies hair follicles and glands. Vessels also connect this network to the superficial vascular plexus which is situated closer to the epidermal-dermal junction in the papillary layer.

1.9 Pain associated with MNs

One of the major advantages of MNs over conventional drug delivery and fluid withdrawal is the lack of pain associated with MN insertion into the skin. There have been a number of studies undertaken to investigate the difference in the perceived

pain of MNs compared to hypodermic needles when used in humans. These will now be discussed below.

To compare the pain caused by different intradermal devices, the magnitude of the pain or discomfort upon application must be quantified. However, the inherent subjectivity of measuring pain levels in a given individual means this can prove difficult. To facilitate this, investigators commonly ask the subjects to rate the severity of the pain on a Visual Analogue Scale (VAS) with each end of the scale marked with descriptors or a numerals (**Figure 1.12**).

Figure 1.12: VAS scale for quantification of subjective pain experienced by human subjects. Reproduced from Melzack et al.[110]

Originally used to rate a patient's perceived wellbeing[111] VAS has also been adapted to score other indications. The subject is usually asked to mark on the scale the intensity of the pain experienced and the distance along the scale is determined[112] in order to provide a quantifiable measurement.

Kaushik et al.[113] conducted a small scale trial on 12 subjects in order to evaluate the pain caused by the application of a silicon MN array containing 400 needles that were 150 μm in length. The needles had an approximately 80 μm wide base and tapered to a 1 μm wide tip. As a positive control, a 26 gauge hypodermic needle was inserted into the skin to a depth of 2 mm which was controlled via modification of the needle cover to expose only 2 mm of the needle. A negative control was also employed for comparison which consisted of a smooth silicon wafer with no MN projections.

The subjects were blinded to the treatment devices and each subject was exposed to each treatment four times in a random order. The subjects were asked to rate the intensity of the pain on a 100 mm long VAS that included the terminal descriptors "No pain" (0) and "Worst Pain" (100). The mean pain score for the MN array was

extremely low (0.67) and was not found to be statistically different from the negative control (0.42) (p = 0.09), whereas the hypodermic needle was reported to cause the most pain (mean pain score = 23.9) which was statistically different to the mean pain score of the MN array (p < 0.001). These results demonstrated that this particular MN array was indistinguishable from the application of a blank silicon wafer and, therefore, could justifiably be described as painless. An important consideration is the 150 µm length of the MNs used in this study, which is relatively short in comparison to other MNs that have ranged up to 1400 µm in length[114].

The pain associated with MNs of greater length was investigated using a solid MN array and hollow MN array in 18 human subjects[115] . The solid MNs were composed of stainless steel wire that had been cut in order to give it a bevelled edge (**Figure 1.13**).
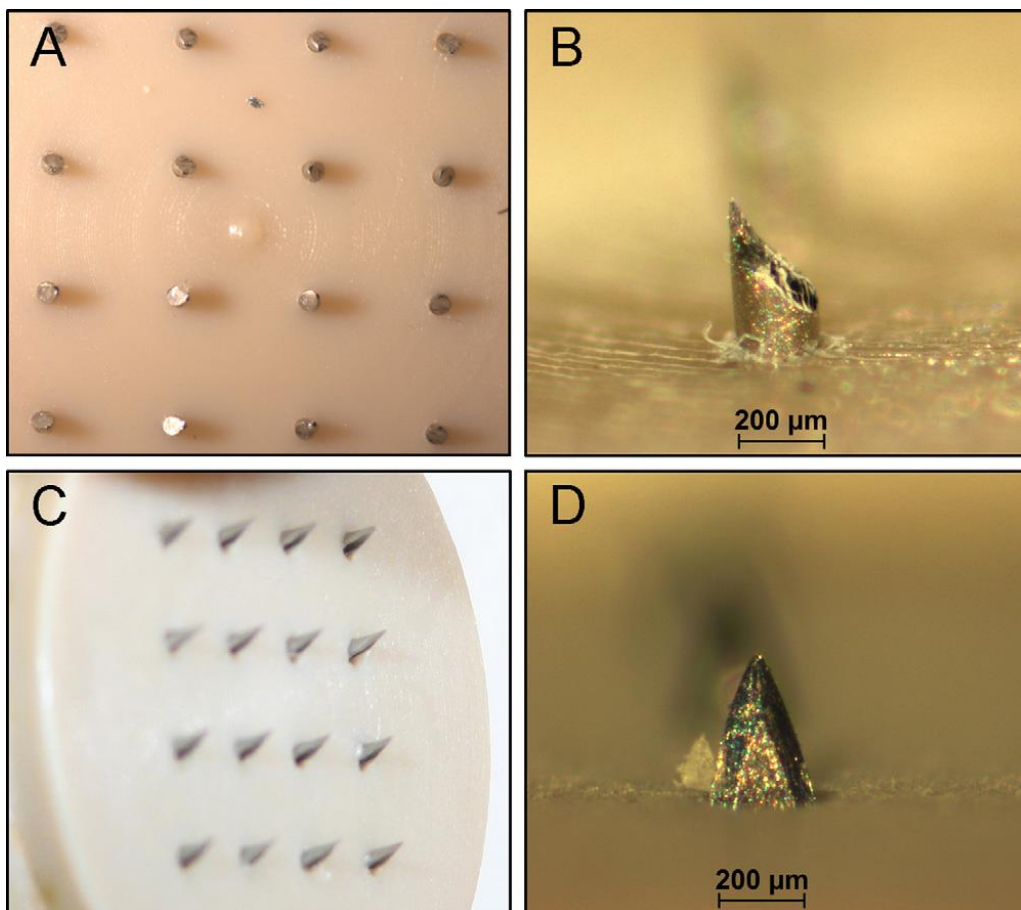
Figure 1.13: (A) 4x4 MN array fabricated from solid stainless steel wires (B) individual MN from solid MN array (C) 4x4 MN array fabricated from hypodermic needles (D) individual MN from hollow MN array

The 4 x 4 arrays were made with MNs of either 200 μm, 300 μm or 400 μm in length (200S, 300S and 400S). The 4 x 4 hollow array was fabricated using stainless steel hypodermic needles and were either 300 μm or 550 μm in length (300A and 550A). The subjects were asked to rate the intensity of the pain immediately after application of each MN (**Figure 1.14**). Blank baseplates were used as negative controls.
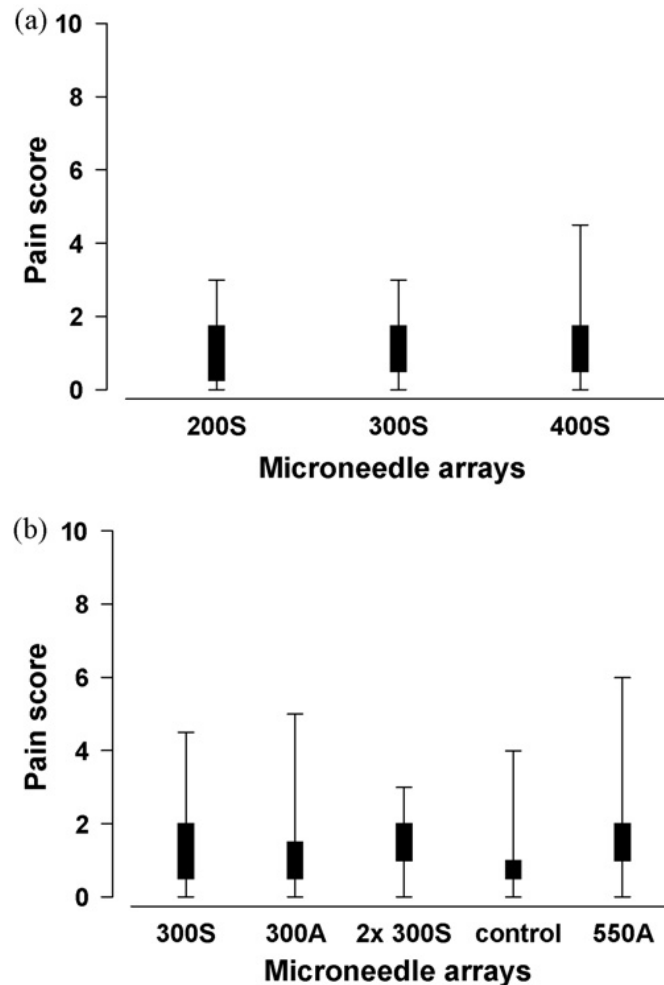
Figure 1.14: (a) Pain scores for solid MN arrays with increasing MN height (200μm – 400 μm) (b) Pain scores for solid MN 300 μm in height compared to hollow MN 300 μm and 550 μm in height.

As **Figure 1.14** shows, the average pain scores were quite low, with the median for all MNs rated as 1 out of 10 apart from the longest MN of 550 μm, which was 2. There was no significant difference found between the negative control compared to any other MN array irrespective of the length, diameter or whether it was comprised of solid or hollow MNs. This study demonstrated that MNs of a greater length than the

previous investigations by Kaushik et al.[113] did not cause any significant pain compared to the control.

In a 12 human subjects trial[116] comparing the pain response of a 25 gauge hypodermic needle to two solid MN arrays of 180 µm and 280 µm long needles a sensory questionnaire was undertaken to describe the types of sensation experienced by the subjects (**Figure 1.15**).
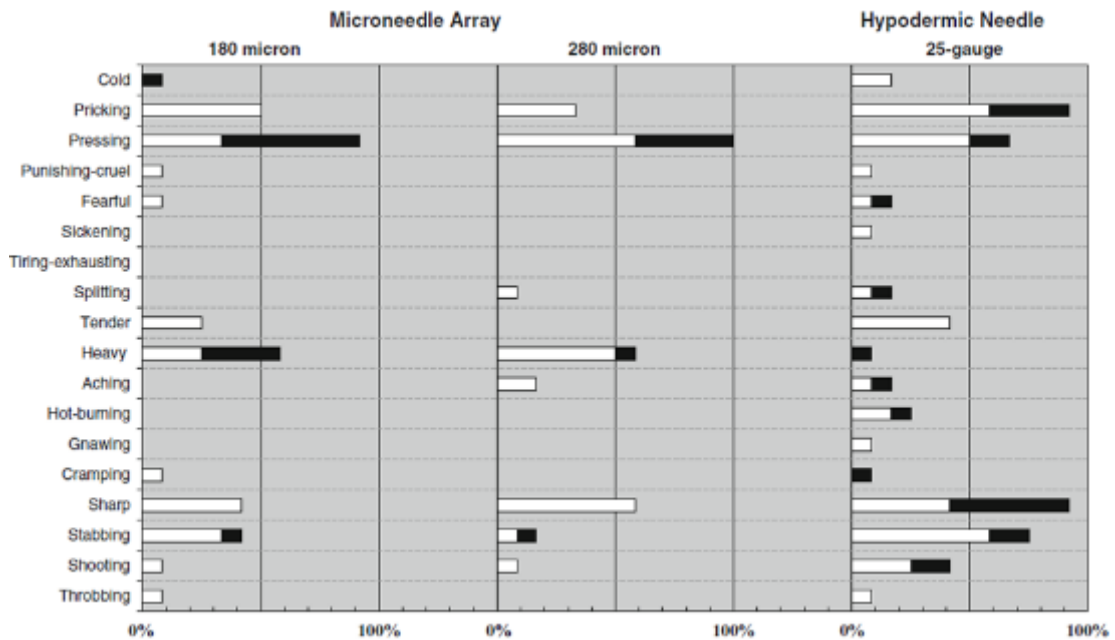
Figure 1.15: Results from sensory questionnaire designed to determine the types of sensation experienced from human subjects after application of two types of solid MN arrays (180 µm and 280 µm in height) compared to a 25 gauge hypodermic needle. White and black sections of each bar represent reported mild and moderate sensations respectively.

The subjects commonly chose the descriptors of "Pressing" and "Heavy" in relation to the application of the MN arrays whereas the terms "Pricking", "Sharp" and "Stabbing" was chosen more frequently and were more often described as moderate in intensity rather than mild for the 25G hypodermic needle. "Sharp" was chosen by subjects to describe the MN arrays however this was universally classed as a mild intensity unlike the hypodermic needle treatment. Results on the pain rating of the devices using a 100 mm VAS indicated that both the 180 µm and 280 µm MN arrays caused statistically significant less pain that the hypodermic needle (p = 0.027 and p = 0.0005 respectively). Interestingly, the VAS score of the shorter MNs was

significantly greater than the longer MN array (p < 0.05). The investigators suggested that this may have been due to the increased force necessary to penetrate the *stratum corneum* using the shorter MN array and so the pressure felt by the subjects was greater upon application of the 180 μm array compared to the 280 μm.

When discussing the pain associated with MNs used to deliver drug or vaccines solution, it is useful to consider the stages of administration. The insertion of the MN into the skin may cause pain as the skin barrier is broken, however, the subsequent delivery of a liquid into the superficial layers of the skin may also cause separate discomfort or pain. Van Damme et. al.[117] investigated this concept with the MicronJet device, which is a hollow MN designed to replace conventional hypodermic needles for the delivery of target compounds and vaccines intradermaly rather than intramuscularly. The device consists of four inline silicon MNs 450 μm long (**Figure 1.16**). The MN array is attached to a plastic adaptor designed to fit a standard luer-slip disposable syringe conventionally used to deliver vaccines.
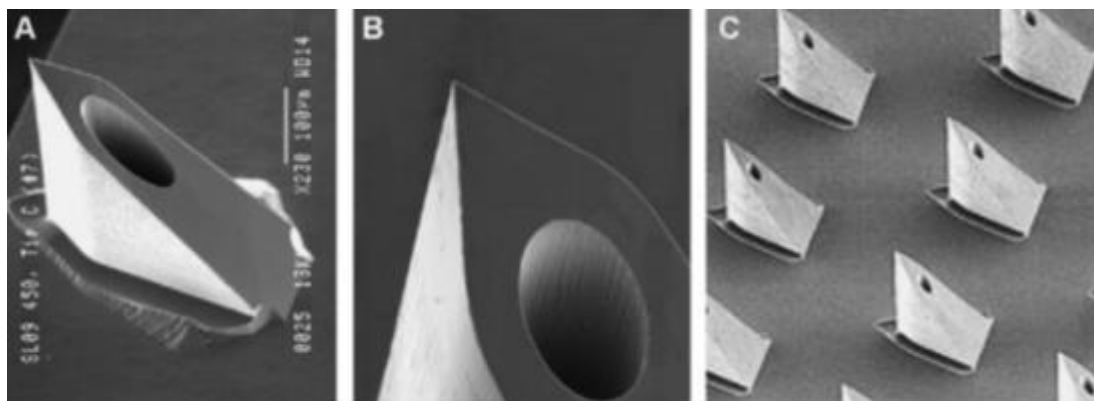
Figure 1.16: (Above) Micronjet device for attachment to standard syringe. (Below) SEM images of silicon MNs from Micronjet device showing morphology of MN tip and array.

In this study, one hundred and eighty subjects were allocated evenly into three groups with each group receiving either a 0.1 ml dose of a seasonal influenza vaccine using the MicronJet device (ID1), a 0.2 ml dose of the vaccine using the MicronJet device (ID2) or a 0.5 ml dose of the vaccine using a conventional hypodermic syringe administered intramuscularly (IM). The subjects, who were blinded to the type of device that was used, were asked to rate the intensity of the pain upon insertion of the MN or hypodermic needle, denoted as the "prick-pain", and then asked to rate

the pain associated with the injection of the vaccine solution into the skin, denoted as the "administration pain", on a 100 mm VAS

The mean VAS score for the prick-pain of the ID1 and ID2 groups were 6.6 and 5.5 respectively whereas the IM group was 12.8. This was a statistically significant difference between the ID1 and ID2 group compared to the IM group (p < 0.001). However, the mean VAS scores for the administration pain were greater in the ID1 and ID 2 group (11.5 and 7.2 respectively) than in the IM group (5.6). There was a statistically significant difference between the ID1 and IM group (p = 0.001). This study highlighted the difference between pain associated with MN insertion compared to the administration of liquid formulations using hollow MNs. While the insertion of the MN device into the skin was deemed less painful than the insertion of a conventional hypodermic needle, the intradermal delivery of a smaller volume of a liquid (0.1 ml and 0.2 ml) was more painful than intramuscular delivery of a greater volume (0.5 ml). One limitation of this study was that each subject only experienced one of the treatment devices. Due to the inherently subjective nature of pain, each subject may have given a different rating to the device compared to each other and so a paired statistical analysis where every subject received each of the treatments may have strengthened the investigation into the pain response. However, this may not have been feasible as the efficacy of the influenza vaccine administered to each subject was also studied and, therefore, additional treatments could not be given to each patient. To overcome this, the additional treatments could have contained blank solutions with no vaccine material.

MNs as long as 2 mm have been investigated for the withdrawal of blood[118]. A single hollow MN fabricated from of silicon was used to withdraw whole blood from 62 subjects in order to compare its blood glucose measurement accuracy and associated pain compared to the standard practice of using a lancet needle and electronic handheld glucometer[119]. The tapered MN was 2 mm in length and 100 μm wide at the base and was fabricated with a hollow channel 25 μm in diameter that ran from the tip of the MN into the 5 mm^2 silicon cuvette housing (**Figure 1.17**). It was designed to allow the passage of the blood from the capillaries near the surface of the skin through the MN via capillary action and into the silicon cuvette where the

concentration of glucose within the blood sample could be determined using optical or electrochemical means.
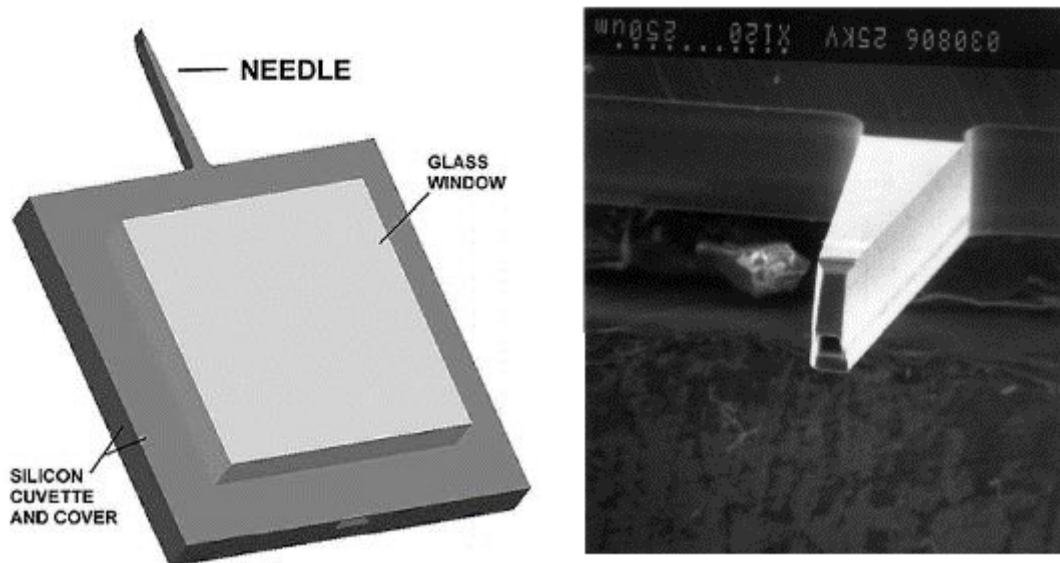
Figure 1.17: (Left) Diagram of single silicon MN with cuvette for blood collection and glass window to view sample. (Right) SEM image of MN tip with opening for fluid withdrawal

In order to compare the pain associated with the insertion of the single MN device to the standard finger prick method, each of the 62 subjects (41 diabetics and 21 non-diabetics) were exposed to three treatments. The first was using a standard lancet to pierce the fingertip to obtain a small volume of capillary blood. The second was the administration of the lancet into the arm of the subject and the third was the administration of the silicon MN device into the arm. Each subject was asked to rate the pain associated with each treatment from 1 – 5 with the following descriptors: 1 – Barely noticeable, 2 – Slightly painful, 3 – Somewhat painful, 4 – Painful, 5 – Very painful. As a significant number of subjects (15%) reported not feeling the silicon MN inserting into the skin at all, a rating of 0.5 – 'Could not feel insertion', was added to the scoring system in order to reflect this.
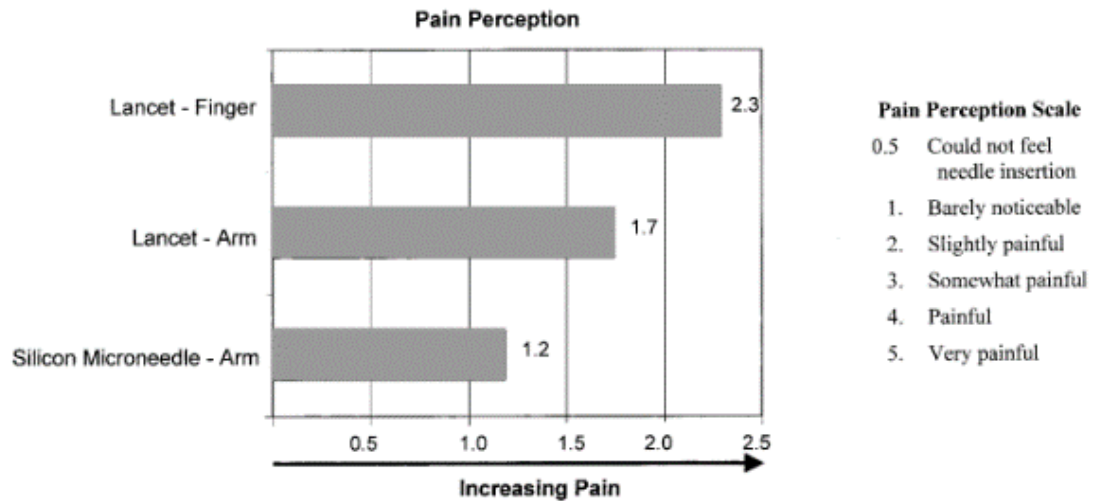
Figure 1.18: Pain scores after insertion of ametal lancet needle in finger and arm compared to hollow silicon MN in arm.

As can be seen in **Figure 1.18,** the treatment with the highest mean pain rating was the lancet applied to the fingertip (2.3), followed by the lancet applied to the arm (1.7) and the least painful was the MN device applied to the arm (1.2). Looking at the individual data (**Figure 1.19**), it was observed that 58% of the subjects responded that the silicon MN was barely noticeable whereas less subjects gave this response for the lancet in the arm (45%) and even less for the lancet in the fingertip (27%). In fact, 15% of the subjects responded that they did not notice insertion of the single MN into the arm at all.
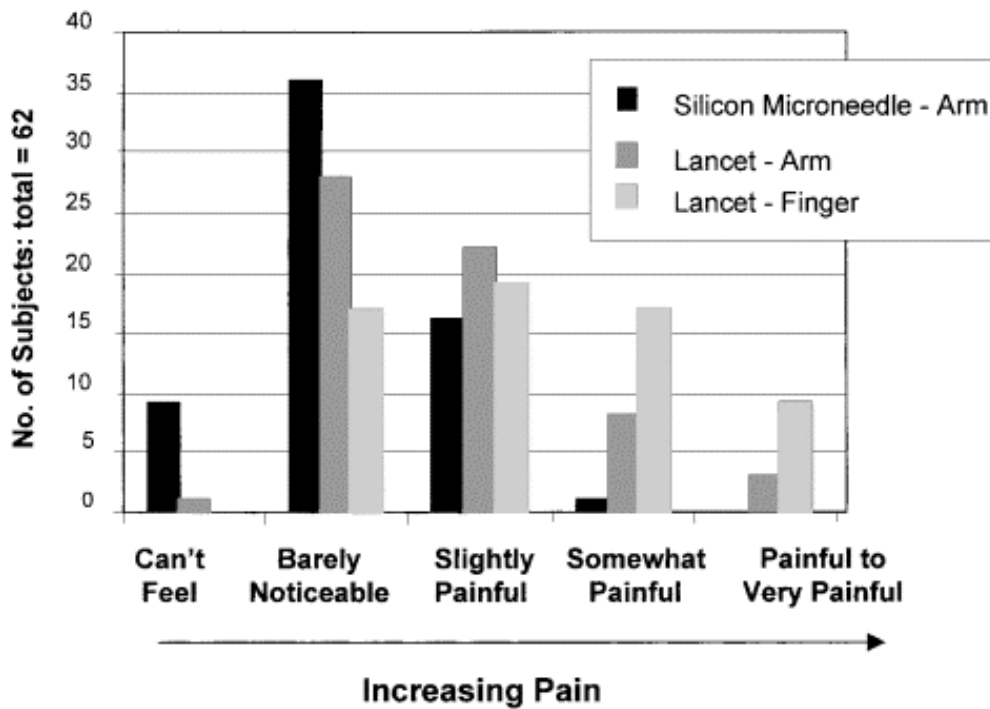
Figure 1.19: Individual break down of pain perception of lancet needle in finger and arm compared to hollow silicon MN in arm

1.10 Glucose Responsive MNs for delivery

Hu et al.[120] aimed to produce a detection-delivery system comprising a glucose responsive MN that modulated the release of insulin in a so called "closed-loop" system. This closed loop system of insulin delivery typically involved glucose monitoring coupled to deliver adequate quantities of insulin in order to maintain proper glucose levels over prolonged periods without causing hypoglycaemia though insulin overdose. Hu et al. incorporated H_2O_2 sensitive polymersomes containing GOx and insulin into the tips of a MN array composed of crosslinked HA. The polymersomes were formed from a block copolymer incorporating polyethylene glycol (PEG) and a phenylboronic ester-conjugated polyserine which was designed to degrade in response to increased concentrations of H_2O_2 caused by the oxidation of glucose by GOx contained within the polymersome. Therefore, in hyperglycaemic conditions, the glucose was oxidised to produce increased levels of H_2O_2 which caused the disassembly of the polymersome. This enabled the release of insulin and subsequent delivery into the skin to ultimately return the body to normal glycaemia.

When administered to streptozocin-induced type 1 diabetic mice the MNs containing the GOx and insulin loaded polymersomes (MN[PV(E+I)]) reduced the blood concentration of glucose to approximately 90mg/dL (5.0 mM) after 1hr and maintained this normal glycaemia for 5 hours compared to blank MNs (MN[HA]) which had no significant effect (**Figure 1.20**).
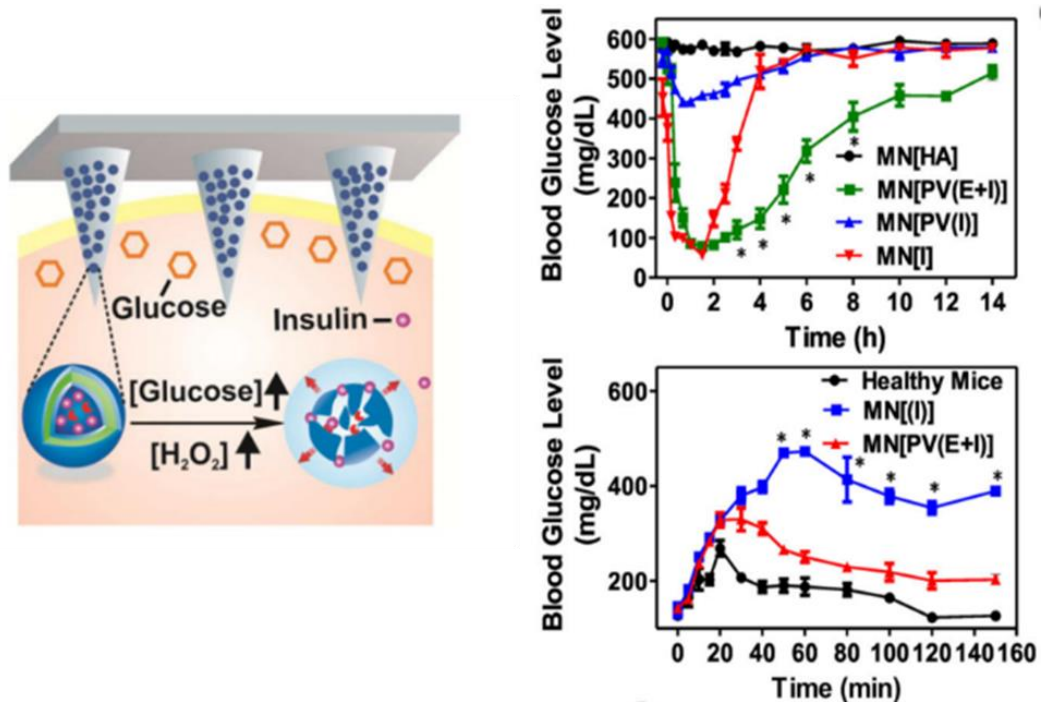
Figure 1.20: (Left) Schematic of HA MN array loaded with H_2O_2 responsive liposomes containing insulin. (Top right) Blood glucose lowering effect of HA MNs loaded with H_2O_2 responsive polymersomes containing insulin (MN[PV(E+I)] compared to blank MNs (MN[HA]), insulin loaded MNs (MN[I]) and MNs with insulin loaded polymersomes (MN[PV(I)]) in diabetic mice. (Bottom right) Blood glucose level in diabetes mice wearing MN[I] or MN[PV(E+I)]) patches challenged with IP glucose injection compared to healthy mice.

In contrast, MNs loaded with the equivalent amount of insulin (MN[I]) had a significantly reduced glucose lowering effect, achieving a blood concentration of approximately 400 – 500 mg/dL (22 – 27 mM). While MNs loaded with polymersomes containing insulin only (MN[PV(I)]) had a comparable glucose lowering effect to the dual loaded polymersome containing MNs,   the effect was significantly shorter lived (2 hours). When diabetic mice were treated with the MN arrays and subsequently challenged with an intraperitoneal (IP) injection of glucose, the MN array containing GOx / insulin had a superior glucose lowering effect compared to the MN array containing insulin only, and more closely resembled the

response to glucose in healthy mice (**Figure 1.20**) However, it was observed the blood glucose was still greater than the healthy mice over the time period of the study (160 min).

A further development by the same research group incorporated a hypoxia sensitive nitroimidazole group via a H_2O_2 sensitive thioether linkage in the same PEG / poly(serine) co-polymer matrix used to formulate the previous MNs[121]. Due to the consumption of oxygen by GOx mediated oxidation of glucose, hypoxic conditions are generated in the local microenvironment. This triggered the conversion of 2-nitrimidazole within the polymersomes to 2-aminoimidazole via native nitroreductases, which is more hydrophilic thus promoting polymersome disassembly and insulin release (**Figure 1.21**). Furthermore, the production of H_2O_2 from the oxidation of glucose triggered a second mechanism of polymersome disassembly as the thioether moiety of the copolymer reacts with the H_2O_2 to form water soluble sulfone groups. In this way, high glucose concentrations within the ISF
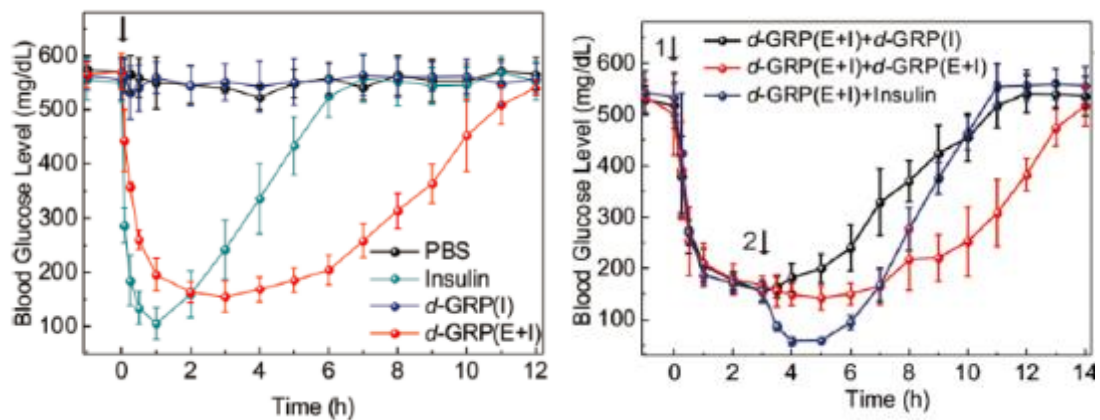
Figure 1.21: (Left) Blood glucose levels in diabetic mice after application of MNs loaded with dual responsive polymersomes containing insulin and enzyme (d-GRP(E+I)) or MNs loaded with d-GRPs containing insulin (d-GRP(I)) compared to PBS control or SC injection of insulin (Right) Effect on blood glucose due to second treatment after initial application of MN containing d-GRP(E+I). The second treatment consisted of either MN containing d-GRP(I), a second MN containing d-GRP(E+I) or a SC insulin.

triggered the release of insulin from the polymersome loaded MNs. The *in vivo* efficacy of the MNs was demonstrated as before in diabetic mice, where the administration of MNs containing the dual sensitive polymersome was decreased the blood glucose concentration after 1 hour and maintained normal glycaemia for approximately 6 hours (**Figure 1.21**), which was a superior duration of action than

the equivalent dose of free insulin. Moreover, in a separate experiment, application of a second polymersome loaded MN 3 hours after an initial MN was applied, did not cause hypoglycaemia to occur in diabetic mice, whereas an injection with the equivalent dose of free insulin caused rapid hypoglycaemia.

More recently, MNs based on crosslinked PVA have been reported to provide glucose responsive delivery of insulin to diabetic mice[122]. The MNs consisted of a crosslinked PVA gel core embedded with GOx and insulin coated with a PVA shell containing catalase. The PVA core was gelated with a H_2O_2 labile crosslinker based on phenylboronic acid thus providing a mechanism of gel degradation in hyperglycaemia as before. Similarly, the insulin contained within the core was covalently attached to the PVA backbone with the same H_2O_2 labile thioether linker therefore enabling elective insulin release in hyperglycaemia. The purpose of the catalase embedded shell of each MN was to provide a H_2O_2 scavenging layer in order to reduce local inflammation to the skin[123]. Diabetic murine experiments with the MNs showed their capability to decrease blood glucose to normal levels and maintain normal glycaemia for several hours without causing hypoglycaemia even after repeated application.

Xu et al.[124] have also utilised a H_2O_2 sensitive mechanism to modulate the release of insulin from mesoporous silica nanoparticles loaded into PVP MNs. GOx contained in the silica nanoparticles generated H_2O_2 that hydrolysed phenylboronic esters present in the structure, causing nanoparticle degradation and subsequent release of insulin that was stored in the nanopores of the silica nanoparticles. *In vivo* efficacy studies in diabetic mice showed a successful hypoglycaemic effect of the MNs due to insulin release and the MNs were able to maintain normal glycaemia in the mice for 4.5 hours compared to 2 hours for a subcutaneous injection of insulin.

1.11 MNs for single measurements of ISF glucose

An array of hollow MNs was produced from monocrystalline silicon by Mukerjee et al.[125] that demonstrated successful ISF withdrawal from a human subject with a subsequent detection of the ISF glucose demonstrated.

The sole driving force behind the ISF extraction was capillary action through the 20 x 20 array of "snake fang" designed MNs that ranged from 250 – 350 µm in length with 300 µm centre-to-centre interspacing (**Figure 1.22**). Upon application, the MN array remained embedded in the skin due to the friction between the MN projections and the upper layers of the epidermis. Initial *in vitro* experiments using a wide range of liquids such as glycerol, acetone and distilled water showed successful transport of liquid from the MN tips through capillary channels that were etched into device to a fluid reservoir.
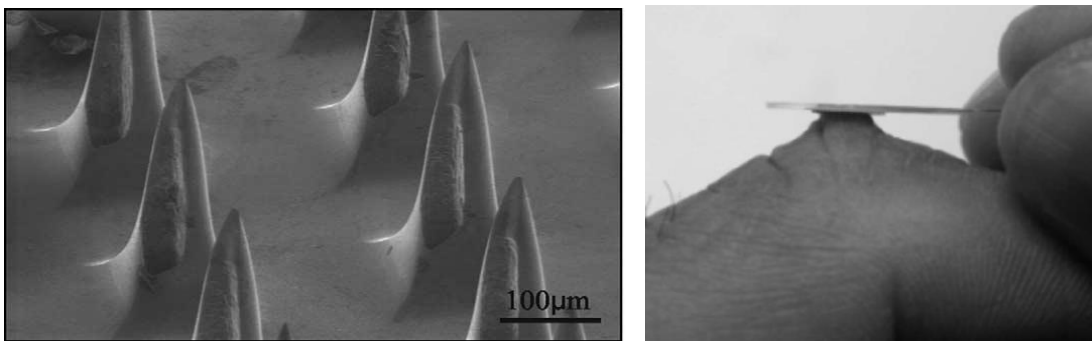
Figure 1.22: (Left) SEM image of hollow silicon MN array with "snake fang" design. (Right) Application of hollow silicon MN array to finger.

When applied to a human subject's skin, ISF was observed to travel from the MN array through the capillaries and into the reservoir after 15 – 20 minutes. The fluid was confirmed as ISF through examination using light microscopy which confirmed there was no visible cellular material as would be in whole blood. Additionally, a small section of a colorimetric glucose test strip was placed in contact with the fluid after extraction (**Figure 1.23**).
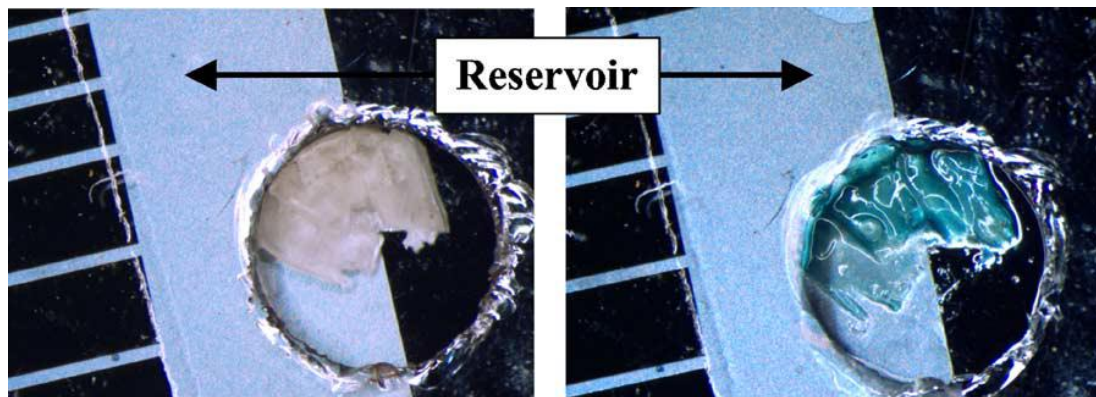
Figure 1.23: Photograph of segment of glucose test strip placed in ISF collection reservoir of hollow silicon MN array. (Left) Before extraction of ISF. (Right) After extraction of ISF

A blue colour change was observed after the test period which confirmed the presence of glucose in the ISF at an approximate concentration of 80 - 120 mg / dL (4.4 – 6.7 mM). Application of a solid MN array followed by collection of ISF using a hydrogel patch was used to monitor post-prandial glucose in human subjects within the ISF in order to compare against plasma glucose[126]. The polycarbonate MN consisted of a 305 array of 300 μm long MNs and was applied to a total of 47 subjects using a spring-loaded applicator with a speed of approximately 6 m/s. Of the 47 subjects tested, 37 were diabetic and 10 were non-diabetic. After MN application at two sites on each subject, a hydrogel patch composed of PVA was placed over the pre-treated area and left in place for 2 hours before subsequent analysis of the glucose using a commercial fluorescent based assay. From plasma glucose measurement taken throughout the study, the area under the curve (AUC) of glucose predicted from the ISF was shown to correlate well to the plasma glucose AUC (R = 0.93). However, the rapid variation in plasma glucose could not be predicted by the ISF due to a lag time between the changes in the plasma compared to the ISF.

Hydrogel forming MNs demonstrated successful extraction of ISF by Caffarel-Salvador et al.[127]. Using optical coherence tomography (OCT), it was confirmed that the hydrogel MNs became swollen with ISF after insertion into both rats and human volunteers (**Figure 1.24**). In this way, it was proposed that the analytes contained within the ISF in the MNs could be measured to provide a minimally invasive and blood free mechanism of therapeutic drug and glucose monitoring.
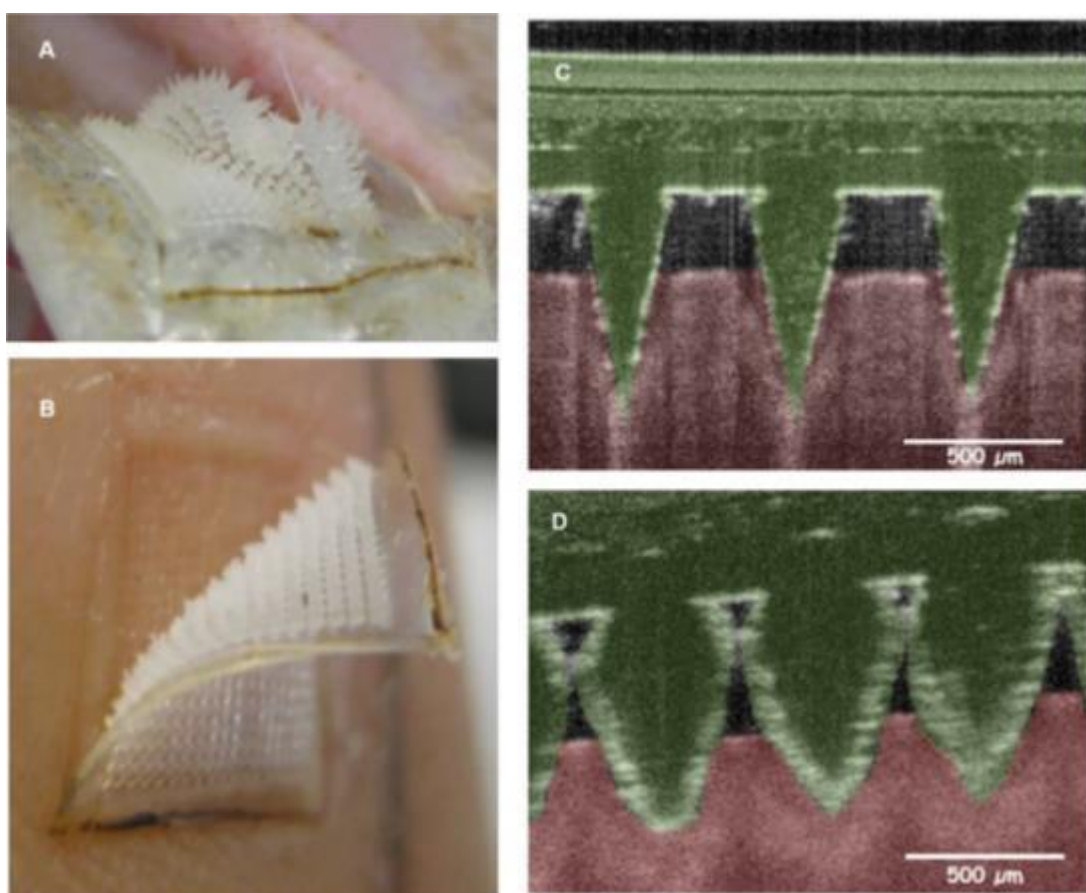
Figure 1.24: Swollen PMVE/MAH hydrogel MN after 1 h application to (A) back of rat (B) human volunteer's forearm. OCT images of PMVE/MA hydrogel MN in forearm of human volunteer (C) upon application (D) 1 h after application.

The MNs, composed of hydrolysed PMVE/MAH (11.1% w/w) crosslinked with PEG (5.6% w/w) were first applied to neonatal porcine skin in a Franz diffusion cell set-up that had been bathed on the underside with phosphate buffered saline (PBS) containing various concentrations of either caffeine, theophylline or glucose. For glucose, test solutions of 4.0 mM and 15.0 mM glucose were used, possibly to represent normal glycaemia and hyperglycaemia respectively. 5 mins and 60 mins post application, the glucose within the MNs was quantified using a proprietary kit after allowing the analytes contained within each MN to diffuse from the hydrogel into a volume of distilled water. After only 5 mins there was a detectable quantity of glucose within both MN arrays with a concentration of 19.46 nM in the 4.0 mM group, however there was no significant difference in the concentration measured in

the MNs exposed to the 15 mM glucose compared to MNs exposed to 4.0 mM glucose at either 5 mins or 60 mins post application.

In order to investigate the ability of the hydrogel MN to track changes in the ISF over time, MNs were also applied to human volunteers after ingestion of 75g of glucose powder. The concentration of glucose in the MNs was compared to plasma blood glucose determined using an electronic glucometer from fingertip blood samples. MNs were applied for one hour before the ingestion of the glucose (-1 – 0 h), for the first hour post ingestion (0 – 1 h), the second hour (1 – 2 h), the third hour (2 – 3 h) and for the entire three hours after ingestion (0 – 3h) (**Figure 1.25**).
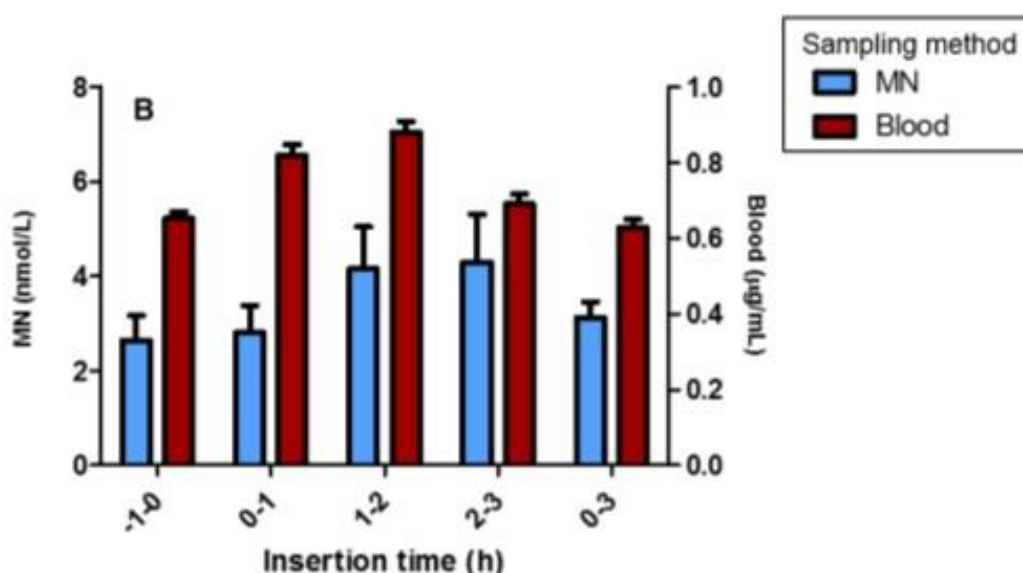
Figure 1.25: Concentrations of glucose measured in PMVE/MAH hydrogel MNs applied to human volunteers to measure ISF glucose compared to blood glucose measurements after ingestion of 75g of glucose at 0h time point.

While the concentrations within the MN were all significantly different than the plasma blood glucose concentrations, it was confirmed that they were capable of extracting ISF from the skin and the glucose could be quantified. The peak plasma glucose was observed 1 hour after ingestion of the glucose powder, with the peak ISF concentration 3 hours post ingestion. This demonstrated a lag time between changes in the plasma glucose and changes to the ISF glucose concentration of approximately 2 hours. This lag time has been observed in previous studies[126].

An alternative approach for the collection of analytes from hydrogel forming MNs was suggested by Romanyuk et al. to enable a higher throughput of samples[128]. Loading a model analyte, sulforhodamine into the tips of MN arrays composed of PMVE/MA (15% w/w) crosslinked with PEG (7.5% w/w), various methods of analyte recovery were investigated. Through attachment of the preloaded MN arrays to the underside of the lids of microtubes designed for centrifugation, the investigators added 100 µL of distilled water to each MN and incubated for 1, 5 and 10 mins followed by centrifugation for 20 s at 300G. After one centrifugation cycle, the fraction of analyte recovered was found to be dependent on the incubation time, i.e. more analyte was recovered after longer incubation periods, and 100% of the analyte was recovered after three successive cycles of centrifugation, independent of incubation time (**Figure 1.26**). A second method of analyte recovery more suited to high throughput of samples and subsequent analysis involved the use of microplates. The MNs were each fixed to a hard plastic backing material and placed on to the open top of microplates so as to act as lids for each well. The MNs were situated on the underside of plastic lids so they protruded into each well, which was filled with an aliquot of distilled water. The plates were then inverted in order to move the water into contact with each MN to allow the recovery of the model analytes into the distilled water. After incubation, the plates were returned to the original orientation and the MNs were removed. In this way, a large number of MNs could be processed simultaneously and the analyte solution could be further analysed in the microplate through enzymatic, UV/Vis or fluorescent assays as required.
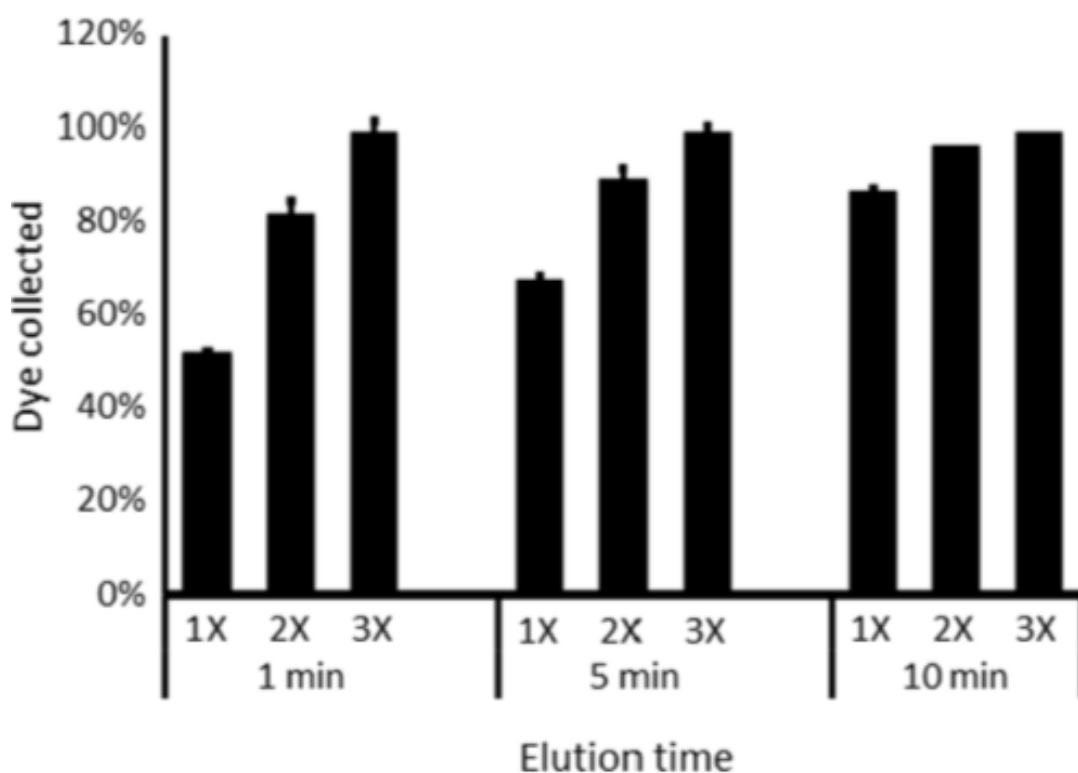
Figure 1.26: Percentage recovery of model analyte from PMVE/MAH hydrogel MNs utilising successive centrifugation cycles after 1 min, 5 min or 10 min elution times.

Another polymer used to produce hydrogel forming MNs is crosslinked HA[129] due to its excellent swelling capability and biocompatibility. In order to form a swellable hydrogel from water soluble HA, the structure was chemically modified through functionalisation with methacrylate groups[130], which can undergo facile polymerisation to form covalent crosslinks between the polymer chains. This enabled the polymer to swell and absorb large quantities of water instead of dissolving. Polymerisation was achieved through free radical catalysis with a photoinitiator activated with UV light. The degree of crosslinking enabled control of the swelling capability of the MNs prepared from this crosslinked HA, with MNs irradiated for longer periods becoming more densely crosslinked and thus capable of absorbing less water from agarose gel, which was used as a tissue surrogate (**Figure 1.27**).
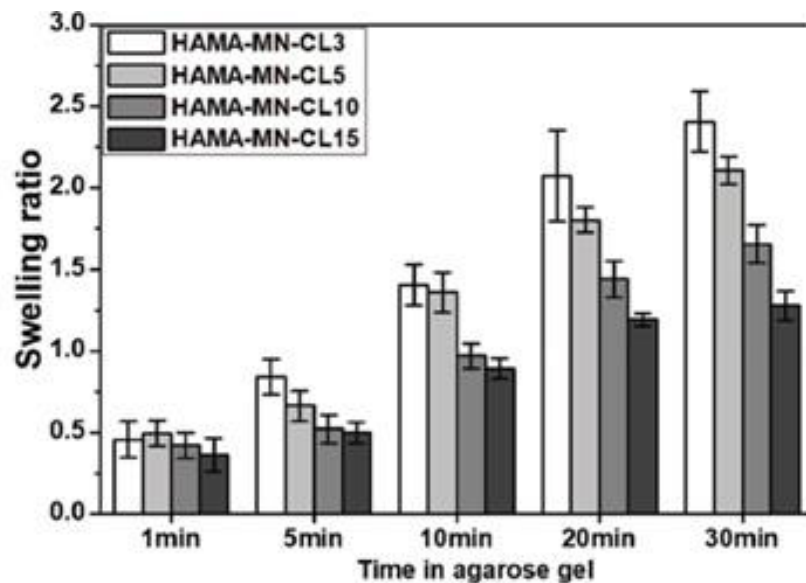
Figure 1.27: Swelling ratio of crosslinked HA MNs applied to agarose gels. MNs were crosslinked for either 3 mins (HAMA-MN-CL3), 5 mins (HAMA-MN-CL5), 10 mins (HAMA-MN-CL10) or 15 mins (HAMA-MN-CL15).

After successful extraction and recovery of the model compounds rhodamine B, glucose and cholesterol from the agarose gel tissue surrogate, the investigators evaluated the effectiveness of the MNs in a mouse model. Four 10 x 10 arrays with a MN height of 800 μm were pressed into the skin on the back of mice with thumb pressure. After 1 min, the total ISF extracted by MNs was measured to be 1.4 ± 0.3 mg. After 10 min, the mass of ISF was 2.3 ± 0.4 mg. This was substantially greater than the amount of ISF extracted in 1 hour reported by Romanyuk et. al.[128] using PMVE/MA (15.0%) and PEG (7.5%) MN arrays. The mice were administered an IP injection of glucose after 1 hour followed by an IP injection of insulin 1 hour later. MNs were applied 30 mins after each injection in order to determine if the change in glucose in the blood stream was observed in the ISF. In order to observe a change in the cholesterol, mice were fed on a high fat diet for up to three weeks prior to the experiment. After each 10 mins application the MNs were removed and the quantity of glucose and cholesterol were determined using a commercial glucose assay and cholesterol quantification kit respectively (**Figure 1.28**).
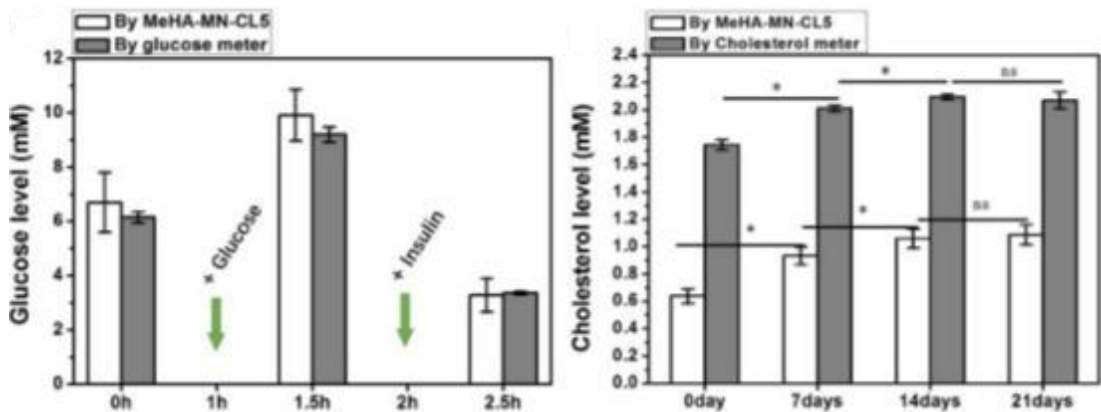
Figure 1.28: (Left) ISF and blood glucose concentration measured by application of crosslinked HA MN or blood glucose meter respectively in mice which were administered IP glucose followed 1 h later by IP insulin. (Right) ISF cholesterol and blood cholesterol measured by crosslinked HA MN or blood cholesterol meter respectively over 21 days of a high fat diet in order to increase cholesterol levels.

It was demonstrated that the crosslinked HA MNs were capable of providing a minimally invasive method to determine the concentration of glucose and cholesterol in the mice with good correlations between ISF glucose concentrations and plasma glucose measured. The ISF cholesterol was consistently lower than the plasma cholesterol and, therefore, the investigators suggested that calibration would be necessary in order to indirectly determine the plasma cholesterol from ISF measurements.

1.12 Flash glucose monitoring device

The Freestyle Libre is a flash glucose monitor that can provide a measurement of the glucose concentration in the ISF present in the dermal layer of the skin[131]. The sensor of the device is a filament that penetrates the epidermis skin layer and becomes embedded in the dermal layer to a depth of 5 mm (**Figure 1.29**). At this depth, the ISF is in equilibrium with the glucose present in the plasma with a lag time of approximately 5 minutes. Each sensor module can remain embedded in the skin for 14 days before being removed and replaced by a new unit. To display the ISF glucose concentration, a companion device or smart phone can be used to wirelessly transfer the data stored within the sensor unit to display to the user.
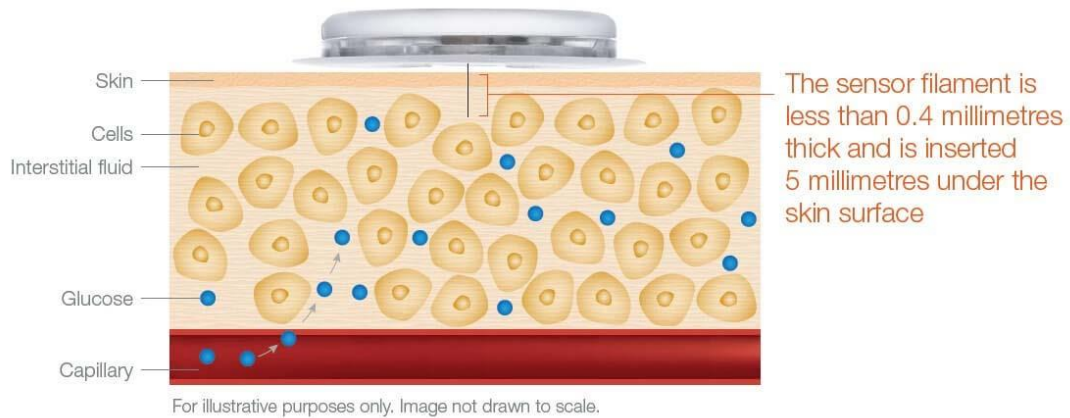
Figure 1.29: Schematic of Freestyle Libre sensor device embedded in skin to provide flash glucose measurements over 14 days[131]

The largest trial of the Freestyle Libre device to date is the IMPACT study[132] which included 242 participants with Type 1 diabetes. The aim of the multicentre, prospective, non-masked trial was to compare the rate of hypoglycaemic events in 120 participants using the Freestyle Libre to 121 participants that used conventional SMBG techniques over 6 months. A 30% or greater reduction in hypoglycaemia was predetermined as clinically relevant by the American Diabetes Association[133]. The mean time spent in hypoglycaemia for the Freestyle group decreased from 3.38 h/day to 2.03 h/day whereas the control group decreased from 3.44 h/day to 3.27 h/day after 6 months. Adjusting for the small decrease observed in the control group, the mean time in hypoglycaemia for the Freestyle Libre group reduced by 38% and so was deemed clinically relevant. There were four allergy related adverse events and four severe insertion site symptoms. Other adverse events were mild or moderate erythema or oedema.

Another trial investigated the accuracy of the ISF glucose measurements to the blood glucose measurements obtained in 72 participants with either Type 1 or Type 2 diabetes over 14 days[134]. The sensor was initially factory calibrated and not further calibrated with blood glucose measurements throughout the trial. Comparison between approximately 8 daily blood glucose readings to ISF glucose revealed a mean absolute difference of 11.4% and a mean lag time of 4.5 - 4.8 mins. On days 2, 7 and 14 the percentage of readings within the Consensus Error Grid Zone A was

88.4%, 89.2%, and 85.2% respectively, with 99.7% of reading within Zone A and B (**Figure 1.30**). As of November 2017 the Freestyle Libre is available on the NHS after initiation under diabetic specialist teams[135].
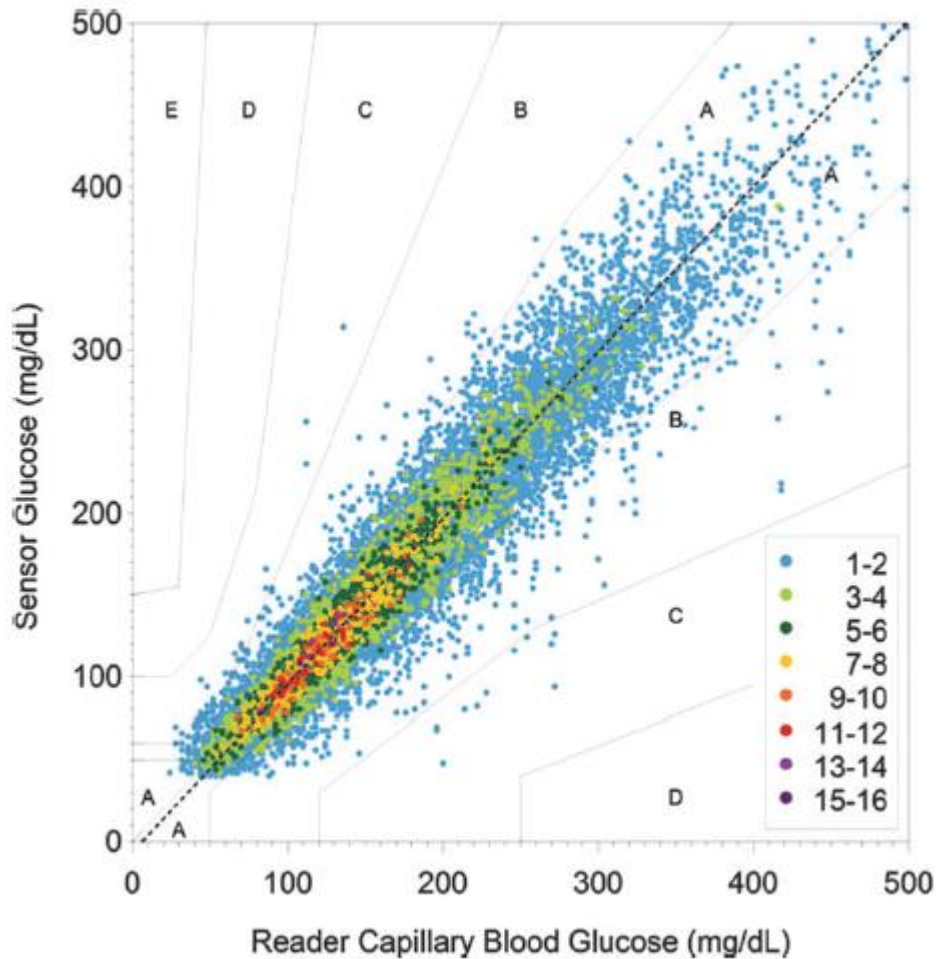
Figure 1.30: Consensus Analysis of Freestyle Libre ISF glucose readings and blood glucose readings with in-built glucose monitor over 14 days continuous use[134].

1.13 Aims and Objectives

The main aim of the work carried out in this thesis was to investigate the feasibility of a MN based approach to measure ISF glucose concentration. The specific objectives were:

1. To determine the most effective MN for the rapid extraction of glucose solution.

2. To develop and optimise an optical detection system for glucose that would provide a colorimetric response to glucose concentration.

3. To identify a suitable housing for the optical detection system that permits integration with the MN baseplate.

4. To test the feasibility of the resulting MN-sensor constructs for their ability to extract and determine glucose concentrations from the colour change in a timely manner.

Chapter 2

2.0 Materials and Methods

2.1 General

2.1.1 Materials, Equipment and Reagents

All chemicals were purchased from Sigma-Aldrich (Gillingham, UK) and used without further purification unless otherwise indicated. Solvents were also purchased from Sigma-Aldrich (Gillingham, UK). Poly(dimethylsiloxane) (PDMS) MN templates were purchased from Micropoint Technologies Pte Ltd. (Singapore). Custom centrifuge inserts to house the MN templates were fabricated from polypropylene. A Form 1+ SLA printer (Formlabs, MA USA) was used to print all CAD schematics using Formlabs' proprietary clear resin. For all digital photography a Canon EOS 100D DLSR camera (Canon Digital, Tokyo, Japan) was used with a Canon EFS 18 - 55mm lens. The following settings were used in manual mode - shutter speed: 1/30, aperture f/5.6 and ISO 400. An intervalometer was used with the camera for repeated photography at set time points. For axial load tests a single column load tester Instron® 3344 (Buckinghamshire, UK) was utilised. A Varian Cary UV-Vis spectrophotometer was used to obtain al UV-Vis spectroscopy data with a 10 mm pathlength quartz cuvette. UV irradiation of polymer solution was carried out using a UVGL-58 handheld UV lamp (UVP, Cambridge, UK). pH measurements were obtained using an electronic pH meter (Hanna Instruments). Hydrochloric acid and sodium hydroxide solutions were used to lower and increase pH respectively.

2.2 Polymeric Hydrogel Microneedles for the Extraction and Optical Detection of Glucose

2.2.1 Swelling studies of PMVE/MA hydrogels crosslinked with PEG

Pre-gel co-polymer blends were prepared consisting of PMVE/MA (20% w/w), PEG (MW 10,000 Da) (7.5% w/w) and increasing quantities of sodium carbonate (0-5%). PMVE/MA was added to distilled water and heated at 90°C for 1 h until fully dissolved. After cooling to 25°C, PEG and sodium carbonate were added and the solution stirred to obtain a homogenous pre-gel blend. To remove air bubbles, the

pre-gel blend was centrifuged at 1000 x g for 15 mins and then poured into square 13 mm x 13 mm silicon moulds. The gels were dried at ambient temperature for 48 h, removed from the moulds and cured at 80°C for 24 h to induce chemical crosslinking by esterification. To determine the swelling capability, each gel square was submerged in PBS (20 mL) at 25°C. The gel was removed after 0.5 h, 1 h, 2 h and 5 h, surface dried using filter paper and weighed. A plot of percentage swelling over time was generated for each formulation (**Figure 3.3**).

2.2.2 Manufacture of MNs prepared using polymer 2

Polymer **2**, consisting of PMVE/MA (20% w/w), PEG (MW 10,000 Da) (7.5% w/w) and sodium carbonate (3% w/w) was used to prepare MNs. The pre-gel blend was prepared as discussed in **Section 2.2.1**. This was then poured into silicon MN templates (Micropoint Technologies, Singapore) so as to exclude air bubble formation. The templates were centrifuged in a custom holder at 800 x g for 20 mins and allowed to dry at ambient temperature for 48 h. The MNs were removed from the templates and placed in an oven at 80°C for 24 hours to induce chemical crosslinking by esterification and yield hydrogel MNs.

Double filled MNs were produced by filling templates with 60 mg of polymer **2** before centrifugation at 800 x g for 20 mins. The templates were allowed to dry at room temperature for 24 h. A second addition of polymer **2** was added to each mould using a pipette until each mould was slightly overfilled. They were allowed to dry for a further 24 h at room temperature followed by heating in an oven at 80°C. The MNs were then removed from the moulds and the excess dried polymer was trimmed using a scalpel to yield MNs with a smooth backplate. Ten of the single and double filled MNs were weighed in order to determine the uniformity of weight using each method.

2.2.3 Development of the glucose sensor

For all photophysical experiments, stock solutions of 3,3',5,5'-Tetramethylbenzidine (TMB) in ethanol and D-Glucose in de-ionised water were prepared. The aqueous glucose stock was allowed to mutarotate for at least 2 h. Unless otherwise specified, for UV/Vis studies a solution of GOx/HRP (425 units/L) and TMB (42 µM) in sodium acetate buffer (pH 5.4) was used as the enzyme-dye system. Each 1 ml aliquot of the

enzyme-dye system was spiked with an aqueous glucose solution in order to give a final concentration of 200 μM glucose. The absorbance spectra between 200 nm – 800 nm were recorded at 60 s intervals over the course of 15 min (**Figure 3.10**)

To investigate how to modify the rate of blue charge transfer complex formation in **Figure 3.12**, four different solutions were prepared with a final concentration of either 850 U/L GOx/HRP and 84 μM TMB, 850 U/L GOx/HRP and 42 μM TMB, 425 U/L GOx/HRP and 84 μM TMB or 425 U/L GOx/HRP and 42 μM TMB in sodium acetate buffer (pH 5.4). Each solution was spiked to contain a final concertation of 200 μM glucose. The UV/Vis absorbance at 650 nm was measured at 60 s intervals for 15 mins.

In order to test the response to a range of glucose concentrations (**Figure 3.13**), eight solutions containing the enzyme-dye system (GOx/HRP (425 units/L) TMB (42 μM)) were spiked with aqueous glucose solutions in order to contain a final concentration of either 0 μM, 10 μM, 50 μM, 100 μM, 150 μM, 200 μM, 300 μM, 500 μM, 750 μM or 1000 μM glucose. The absorbance spectrum for each was recorded after 8 mins.

To increase the linear range of the sensor, solutions containing 42 μM TMB in sodium acetate buffer (pH 5.4) and either 425 U/L, 212 U/L or 106 U/L GOx/HRP were spiked with glucose in order to obtain final concentrations of 0 μM, 10 μM, 50 μM, 100 μM, 150 μM, 200 μM, 300 μM, 500 μM, 750 μM or 1000 μM glucose. The absorbance of each solution at 650 nm was recorded after 8 mins (**Figure 3.16**).

2.2.4 Investigation of glucose sensor performance of polymer 2

Pre-gel blends of polymer **2** were prepared as described in **Section 2.2.1**. Before casting into moulds, a 1 ml aliquot of the polymer **2** pre gel blend was pipetted on to a weigh boat and photographed 5 mins and 10 mins after addition of a 10 mM glucose solution (100 μL) (**Figure 3.17**).

A MN composed of polymer **2** prepared using the method detailed in **Section 2.2.2** was submerged in a 3 mL solution containing 425 U/L GOx/HRP and 42 μM TMB in sodium acetate buffer. After 2 h the MN had imbibed the solution and any surface solution removed with filter paper. A 100 μL aliquot of 10 mM glucose solution was

pipetted on to the surface of the swollen MN and imaged after 4 and 8 mins (**Figure 3.17**).

2.2.5 Synthesis of PMVE/MA and TPME backplates

PVME/MA (2g) was dissolved in distilled water and heated to 90°C for 1h. Upon cooling, tri(propyleneglycol) monomethyl ether TPME (1g) was added and the pH adjusted to 5.4 with 3 M NaOH. The final weight of the solution was then made up to 10 g with distilled water. GOx/HRP and TMB solutions were added to the gel to obtain final concentrations of 425 U/L and 42 µM respectively. To remove air bubbles the pre-gel blend was centrifuged at 1000 x g for 15 mins and then poured into square silicon moulds with 10 mm x 10 mm dimensions. The gel was allowed to set overnight in a fume hood at 25 °C. For attachment to hydrogel MNs, a small quantity of distilled water (1 µL) was added to the centre of the backplate before placing on to the back of the MN and dried at 25 °C in a fume hood.

2.2.6 In vitro extraction of glucose from simulated ISF

MNs were fabricated from polymer **2** as detailed in **Section 2.2.2** and interfaced with sensor embedded TPME backplates as described in **Section 2.2.5**. The MN projections were penetrated through a single layer of Parafilm using thumb pressure and placed on the surface of glucose solutions (0 – 10 mM) (PBS) to start the extraction procedure. Photographs of the backplates were taken over 1 h (**Figure 3.21**).

2.2.7 Fabrication of sensor embedded paper backplates

Whatman No 1 paper was used to create square backplates measuring 10 mm x 10 mm. Each backplate was submerged in 3.5 mL of a 50:50 distilled water : ethanol solution containing GOx/HRP and TMB for 5 min. In order to optimise the quantities of GOx/HRP and TMB, four formulations (A-D) contained different amount of enzyme but the same quantity of TMB were prepared. The quantities for Formulation A-D are listed in **Table 3.1.** The backplates were then removed and allowed to dry at 25 °C for 2 h.

2.3 Single Hollow Microneedle Device for the Extraction and Colorimetric Detection of Glucose

2.3.1 3D printing of solid MNs and MN master moulds using Form 1+ printer

CAD schematics of MNs for 3D printing were initially created using SketchUp (Trimble) in order to produce STL (stereolithography) files that are native to 3D printing software and were suitable for the Form 1+ printer. In order to repair any issues with the CAD schematics before printing, the files were analysed using NetFabb basic (Autodesk) and default repairs were carried out if necessary.

The Form 1+ printer resolution was set to 0.025 mm. After STL files were loaded into the Formlabs printer software, default supports were added to the models and modified if necessary to avoid creating points of contact between the key areas of the model and the support (e.g. MN tips or inner areas of moulds). After printing, models were removed from supports using cutting pliers and washed twice in isopropanol and dried in an oven at 50 °C for 1 h.

2.3.2 Production of negative silicone moulds for hollow MN

A 30G needle was inserted into the 3D printed mould until the tip came into contact with the attached lid. The lid was removed and the needle was fixed in place with cyanoacrylate glue. Room temperature vulcanising (RTV) silicone (Viscolo 13, TOMPS UK) was used to create a negative mould of the master mould with the attached needle (**Figure 2.1**). The silicon was prepared according to the manufacturer's instructions. Equal amounts by volume of part A and B were thoroughly mixed in a 50 ml polypropylene tube using a stirring rod. The bubbles introduced from the mixing were removed by placing the open tube in an upright position in a vacuum oven at RT. A vacuum was applied to the oven for 30 mins until no visible bubbles remained. The silicone was then taken up into a 5 ml syringe which was subsequently attached to the needle hub in the 3D printed mould. The silicone was pushed through the needle until a small quantity of the liquid exuded from the tip. The syringe was then removed and the mould was placed on an even surface. The remaining silicone from the 50 ml centrifuge tube was then poured into the mould until it was completely filled, avoiding the introduction of air bubbles. The silicone was left to crosslink for 16 h at 25°C. After fully solidifying, the silicone negative mould was

peeled away from the 3D printed master mould, ensuring the thin line of silicone that protruded into the barrel of the needle remained attached to the base of the negative mould. The mould was washed with distilled water and then methanol before being allowed to dry at 40 °C for 60 mins.
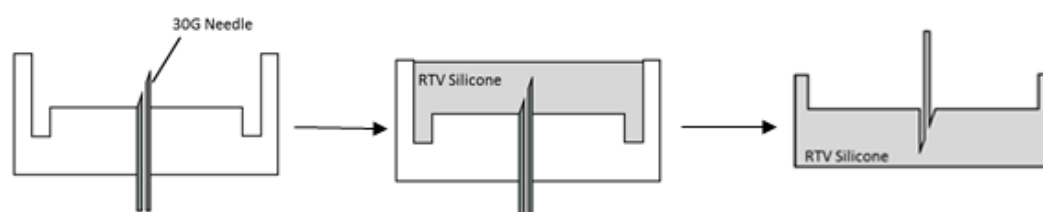
Figure 2.1 Fabrication of silicone negative mould for production of hollow polymer MN

2.3.3 Single hollow polymer MN

A stock solution containing glycidyl methacrylate (GMA) (10 ml), trimethylolpropane trimethacrylate (TRIM) (5.23 ml), triethylene glycol dimethacrylate (TEGDMA) (15.7 ml) and Irgacure 184 (0.1 g) was prepared. If not used immediately, the solution was wrapped in aluminium foil to avoid inadvertent polymerisation from ambient light and refrigerated at 5 °C overnight. An aliquot of 150 µL of the solution was added to each of the negative silicone moulds while the length of silicone that replicated the inner bore of the needle was held upright at 90°C using a small scaffold structure. To ensure the moulds were completely filled, they were placed in a vacuum oven at RT and a vacuum was applied for 60 mins to force the liquid into the tip of the moulds. The monomer mix was then polymerised using a 365nm emitting UV lamp (6W, 50Hz, 0.12 A) for 30 mins until the polymer mix had fully solidified. The hollow MNs were then removed from each mould and washed with methanol before drying in an oven at 40 °C for 60 mins.

2.3.4 Kinetics of Methylene Blue extraction using the hollow MN device.

An aqueous solution (30 mL) of methylene blue (MB) at a concentration of 1.0 mM was added to a plastic 90 mm petri dish. A hollow polymer MN was pierced through a single layer of Parafilm to simulate skin penetration. Segments of Whatman No. 1 filter paper were cut into 5 mm^2 squares and attached to the back each MN device. The MNs were then placed on the surface of the MB solution ad photographs of the

paper square backplate were taken at 1 s intervals for 5 s in order to capture the extraction of the coloured solution (**Figure 4.8**).

2.3.5 Mechanical testing of the hollow MN device

The magnitude of the force required to fracture the single MN in the hollow polymer MNs was measured using an axial load test station with a 50 N load cell. The MNs were fixed to a horizontal metal block using double sided adhesive tape. To enable sufficient adhesion to the tape and to avoid any lateral movement during axial compression, the backplate of each MN was first roughened using sandpaper before application of the adhesive tape. A metal rod with a diameter of 4 mm was driven downwards on to the MN tip at a rate of 0.01 mm/s until fracture of the MN occurred. This was monitored using an optical microscope to visually confirm that the rod was lowered directly on to the MN tip and that breakage occurred.

2.3.6 Measurement of $Chrom_B$ in MB soaked paper backplates

Stock solutions of MB (0-1 mM) in distilled water were prepared. Blank paper backplates were submerged in each solution, removed and allowed to dry at room temperature. Photographs of each backplate were recorded and the $Chrom_B$ values calculated. This was achieved by obtaining the red (R), green (G) and blue (B) values from the photograph of the backplate using ImageJ with the RGB measure plugin. The $Chrom_B$ was calculated by dividing the B value by the sum of the R, G and B values. All measurements were background corrected by subtracting the $Chrom_B$ value of a white paper square submerged in distilled water and dried. In the case of sensor embedded glucose responsive backplates, the $Chrom_B$ values were calculated from digital photographs of each backplate after an aliquot of glucose solution in PBS was added or the MN device had extracted glucose solution into the backplate.

2.4 Glucose detection using a hollow metal microneedle interfaced with an optical glucose sensor: the use of antioxidants to modulate signal response.

2.4.1 Fabrication of custom needle holder and metal MN

A custom made needle holder was fabricated from polypropylene plastic (**Figure 5.3**). The upper plate (diameter 30 mm) was cut to a thickness of 2 mm and four holes were drilled through the plate in a cross pattern using 200 µm diameter steel drill bit. A circular hole (diameter 30 mm) was made in the base plate in order to hold the upper plate in place when placed together. A screw was used to ensure a tight connection between the upper plate and base plate.

BD Micro-Fine ™ Ultra 32G needles were removed from their outer packaging, placed in 100 mL of acetone and stirred for 4 hours in order to dissolve the adhesive holding the metal needles to their plastic housing. The needles could then be removed from the housing using tweezers. A needle was placed in each of the four holes on the upper plate of the needle holder, with the shorter bevelled end pointing downwards (**Figure 5.4**). The upper plate was then screwed on to the baseplate. A pair of cutting pliers was used to cut the metal needles to approximately 4 mm in length before the remaining length of needle was removed using abrasive sand paper. P600 grade paper was used to remove the majority of the excess material before P1000 grade paper was used to remove the final 0.5 mm to avoid unwanted burrs or imperfections along the edges of the needle that could form blockages. The holder was then disassembled and the needles were removed from the upper plate using tweezers. 100 µm diameter steel wire was threaded through each of the cut needles to remove material that had plugged the lumen and to ensure they remained open. They were then rinsed with acetone and dried at RT for 10 mins to yield 2 mm long 32G needles.

2.4.2 Fabrication of the metal MN and photopolymer baseplate

A master mould was 3D printed using the Form 1+ printer in clear resin (**Figure 2.2a**). RTV silicone was prepared as detailed in **Section 2.3.2,** poured into the master mould and allowed to cure for 16 h at 25°C. It was then removed from the master, washed with ethanol and dried to yield the negative silicone mould for the photopolymer baseplate. 100 µm diameter wire was threaded through a 32G BD needle which was pierced through the centre of the negative mould so that the wire was perpendicular

to the surface of the mould. The full size needle was then removed, leaving the wire in place. A 2 mm long needle was then threaded down the wire with the needle point facing upwards until the lower end reached the silicone mould (**Figure 2.2b**). 200 µL of TRIM containing 0.1% w/w of Irgacure 184 as a photoinitiator was pipetted into the mould and polymerised by placing under a 365nm emitting UV lamp (6W, 50Hz, 0.12 A) for 60 mins. The MN and baseplate was then removed from the mould, washed with methanol and dried at 60°C for 10 mins.

(a)
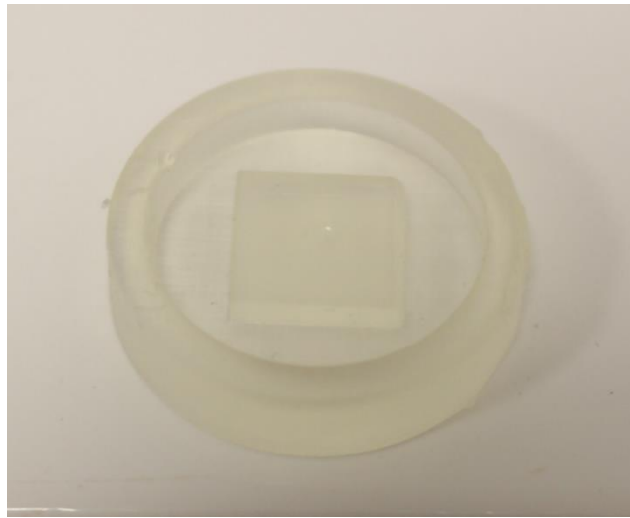
(b)
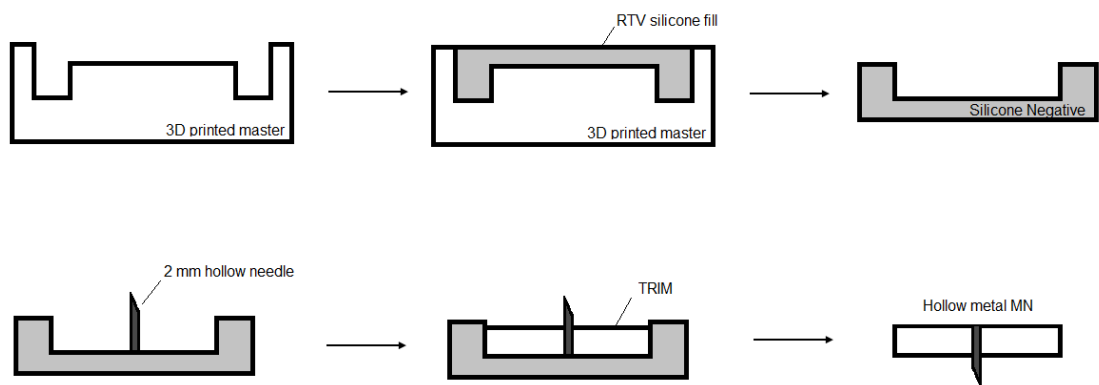
Figure 2.22: (a) Master mould produced using Clear resin (proprietary) using Form 1+ 3D printer. (b) Schematic using master mould to create negative silicone mould. This was then used to hold 2 mm needle in place for the formation of the surrounding baseplate to produce the metal MN.

2.4.3 Fabrication of PDMS suction housing and assembly of the metal hollow MN device

A master mould was printed using the Form 1+ printer in clear resin, washed in isopropanol and then dried. PDMS (Sylgard 182 Silicone Elastomer, Dow Corning) was prepared according to the manufacturer's instructions. This involved mixing the base and catalyst in a 10:1 ratio (w/w) in a 50 mL polypropylene tube and mixing thoroughly with a disposable glass stirrer. The tube was then placed in a vacuum oven and air bubbles removed by applying a vacuum force for approximately 60 mins. The PDMS was then poured into the master mould to minimise entrapped air pockets. The filled moulds were then placed in an oven overnight to cure at 100 °C. Subsequently, the PDMS housings were removed from the moulds and washed with methanol and dried. In order to create the transparent PDMS housing as shown in **Figure 5.13**, the centre surface of the 3D printed master mould was covered with a glass microscope slide. In order to ensure sufficient adhesion to the mould, the underside of the glass slide was roughened with sand paper before the application of cyanoacrylate glue. The glue was allowed to completely dry before addition of the PDMS liquid and the housing was fabricated as previously described above.

To assemble the MN devices, the PDMS housings were affixed to photopolymer baseplates containing the metal MN as described in **Section 2.4.2** using cyanoacrylate glue. Sensor backplates or blank paper squares were placed on the back of the baseplates before attachment of the PDMS housing.

2.4.4 Photophysical investigation of the glucose sensor coupled with ascorbic acid
A 50:50 ethanol and distilled water solution of 625 U/L GOx, 125 U/L HRP and 3.33 mM TMB was prepared. Sufficient quantities of ascorbic acid (AA) was added to aliquots of the sensor solution to give a final concentration of either 0 µM, 20 µM or 40 µM AA. 5 µL of aqueous glucose solution (7.5 mM or 10 mM) was added to each sensor solution and the absorbance at 650 nm was determined using UV-Vis spectroscopy at 10 s intervals for 5 mins.

2.4.5 Glucose sensor embedded paper backplates modified with AA

10 mm^2 paper squares were submerged in an ethanol / distilled water solution (50:50 v/v) containing 6250 U/L GOx, 1250 U/L HRP and 3.33 mM TMB for 5 mins before removal and drying at 25 °C for 1 h. The paper backplates were then dipped in aqueous solutions of AA (0 – 10 mM) before a further drying step at 25 °C for 1 hr. To each backplate was then added 1 µL of either 7.5 mM or 10 mM of a glucose solution in PBS. Digital photographs of the backplates were then taken after 60 s (**Figure 5.16**). A further experiment was subsequently undertaken where sensor embedded backplates containing 5mM AA were photographed every 60 s for 5 mins after the addition of 1 µL of 0.0 mM – 20 mM aqueous solutions of glucose (**Figure 5.17**).

2.4.5 In vitro extraction of glucose solutions using the assembled metal hollow MN with AA modified glucose sensor backplate

Metal hollow MN devices with 5 mM AA sensor backplates were assembled as detailed in **Section 2.4.3.** Two glass slides were fixed to the surface of a 90 mm petri plate to act as a scaffold for the MN device. The petri plates contained 30 mL of glucose solution in PBS ranging from 0 – 20 mM . A gap of approximately 2 mm was left open between the slides to allow access to the glucose solution in the plate (**Figure 5.10**). The MN device was pierced through a single layer of Parafilm and placed on top of the two glass slides with the extruding MN touching the glucose solution. The flexible PDMS housing was pressed and released using finger pressure in order to extract the glucose solution into the device. The devices were photographed at 30 s intervals for 120 s to observe the colour change on the sensor embedded backplates.

3.0 Polymeric Hydrogel Microneedles for the Extraction and Optical Detection of Glucose

3.1   Introduction

As discussed in **Chapter 1**, frequent glucose monitoring is a key requirement for the effective management of diabetes. The exchange of glucose and other biological analytes between the plasma present in the capillaries near the surface of the skin with the extracellular fluid compartment and ISF allows an opportunity to access these analytes without the need for blood sampling. As glucose levels found in the ISF correlate well with those found in the plasma, with a mean absolute difference of approximately 10%[136,137], the measurement of glucose within the ISF provides an indirect measurement of the glucose present within the blood capillaries and can be used in the monitoring of hyperglycaemia in diabetes.

3.1.1 ISF monitoring using microneedles

As discussed in **Section 1.11** there have been a wide range of MN based methods investigated to remove ISF from the skin in order to gain access to the analytes within. One of the most promising approaches are MNs prepared from swellable hydrogels composed of PMVE/MAH and PMVE/MA crosslinked with PEG[138]. These MNs can penetrate the *stratum corneum* in the dry xerogel state and absorb ISF that can be subsequently be removed and analysed. The MNs have demonstrated the ability to be removed from the skin intact after application therefore leaving no polymer residue behind. This is an important consideration in ensuring the biocompatibility of the system. A further advantage of PMVE/MA based MNs is the decreased chance of needle stick injuries as after removal from the skin the MN projections are unable to re-penetrate skin due to the absorption of the fluid.

3.1.2 Poly(methylvinylether/maleic acid) MNs

In an effort to increase the swelling capabilities of the hydrogel, sodium carbonate has been added to the formulation as a modifying agent[139]. The sodium carbonate acts by neutralising a proportion of free carboxylic acids present on the maleic acid

subunits of the backbone, thus providing less opportunities for the esterification reaction of the PEG to form crosslinks with the backbone. This decreased crosslinking density results in an increase in the swelling capability of the hydrogel. A balance must be maintained however, as when the crosslinking density is decreased sufficiently by the addition of a large amount of sodium carbonate, the hydrogel will lose its swelling capability and become soluble.

3.1.3 Extraction and determination of glucose concentration

Current approaches to determining the analyte concentration contained within PMVE/MA MNs involve post processing steps. The ISF is removed from the MN either by centrifugation[128] or by adding the MN to water and allowing the analyte to diffuse out of the swollen MN and into the surrounding solution[10] . The concentration of the analyte can then be determined using various methods such as HPLC, electrochemical glucometers or enzymatic assays[129]. These "off board" analytical steps have the disadvantage of requiring external equipment, trained users and complex steps that preclude these from being used in a POC device in their native form. An integrated device that permits the MN to perform in situ analysis bypasses these drawbacks and would allow these MNs to become point of care devices that patients could use without training to determine clinically relevant measurements related to disease.

3.1.4 Colorimetric Determination of Glucose Concentration

Visual determination of a colour change is one possible way of enabling a result to be determined without the need for external equipment. Such colorimetric tests for glucose have been widely used commercially, paired with a calibrated colour chart for the determination of glucose in urine[140] (e.g. Clinistix®). These tests rely on the glucose oxidase catalysed metabolism of glucose to produce gluconic acid and hydrogen peroxide. The hydrogen peroxide is then used to oxidise a dye to produce a colour change. 3,5,3',5'-tetramethylbenzidine (TMB) is one such dye and can be used to detect the resultant hydrogen peroxide by forming the one electron oxidised blue colour charge transfer complex when catalysed by a peroxidase enzyme[141]. This blue coloured compound can then be further oxidised to the two electron oxidised

yellow diimine derivative (**Figure 3.1**). Subsequently, the amount of glucose present in the sample can be determined by correlating with the intensity of either the blue or yellow colour change.
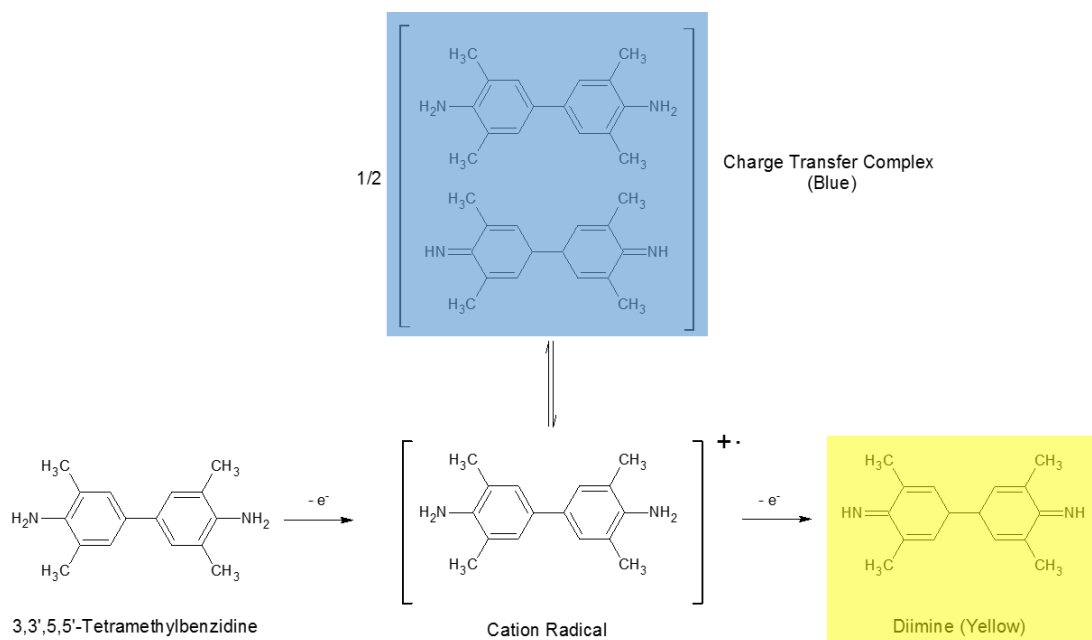
Figure 3.1 Scheme of the oxidation of TMB by hydrogen peroxide producing blue charge transfer complex and yellow diimine.

After a single electron oxidation TMB is converted to a radical cation which forms an equilibrium with the blue coloured charge transfer complex. After a further oxidation, the charge transfer complex is converted to the yellow diimine form.

3.2 Aim and Specific Objectives

The main aim of the work undertaken in this chapter was to develop a hydrogel based MN device capable of penetrating skin and swelling with ISF containing glucose. A colorimetric sensor will be integrated with the MN to allow the visual determination of glucose concentration. The specific objectives were:

i.   Investigate the swelling capabilities of hydrogels prepared from poly(methylvinylether/maleic acid) and crosslinked using poly(ethylene) glycol at various crosslinking densities.

ii.   Manufacture highly swellable hydrogel MN arrays from the polymers prepared in (i) above.

iii.   Develop an optical detection system (hereafter referred to as sensor) for physiologically relevant concentrations of glucose.

iv.   Develop a suitable matrix for the sensor enabling it to be interfaced with the hydrogel MN to produce an integrated device.

v.   Investigate the ability of the integrated MN-sensor to determine glucose concentrations in solutions simulating ISF.

3.3 Results and Discussion

3.3.1 Swelling studies of PMVE/MA hydrogels crosslinked with PEG

To investigate the effect of altering crosslinking density with sodium carbonate, three PMVE/MA hydrogels were prepared. Each formulation contained PMVE/MA (20% w/w), PEG (7.5% w/w) (MW 10,000 Da) and sodium carbonate at either 0%, 3% or 5% w/w (polymers **1 2** and **3** respectively) with the remaining mass balance comprising distilled water.
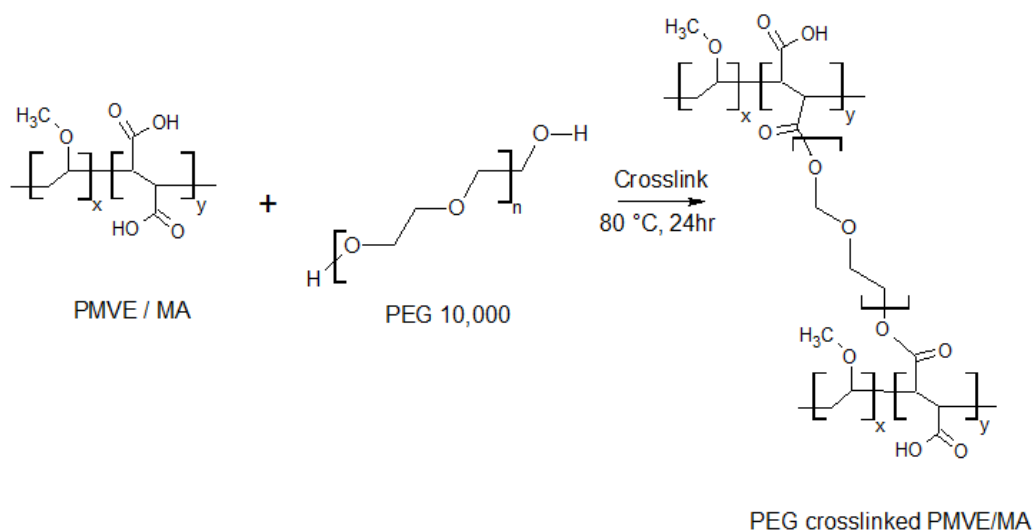
Figure 3.2 Scheme of crosslinking reaction between PMVE/MA and PEG

Following dissolution, the separate solutions were centrifuged at 1000 x g to remove air bubbles and cast in thin films using a 13 mm x 13 mm moulds. These films were left to dry at ambient temperature for 48 hours then placed in an oven at 80°C for 24 hours. This allowed the polymer backbone to become crosslinked through ester bond formation between the carboxylic acid residues of the maleic acid subunits and the terminal hydroxyl groups on PEG as shown in **Figure 3.2**. After crosslinking, the squares of each film were submerged in phosphate buffered saline (PBS) and

periodically removed, dried with filter paper and weighed to monitor the swelling characteristics. The percentage swelling was calculated using **Equation 3.1**:

$$\% \text{ Swelling} = \frac{m_t - m_0}{m_0} \text{ x } 100$$

Where m_t is the mass at each time interval and m_0 is the starting mass of each film. The results, shown in **Figure 3.3,** illustrate that the formulation without sodium carbonate reached a percentage swelling at equilibrium of 2676% w/w ± 488%. The inclusion of 3% sodium carbonate significantly increased this to 7343% w/w ± 1071% at equilibrium ($p < 0.01$ at 5h). The formulation containing 5% sodium carbonate did not swell with PBS but rather dissolved after a few minutes.
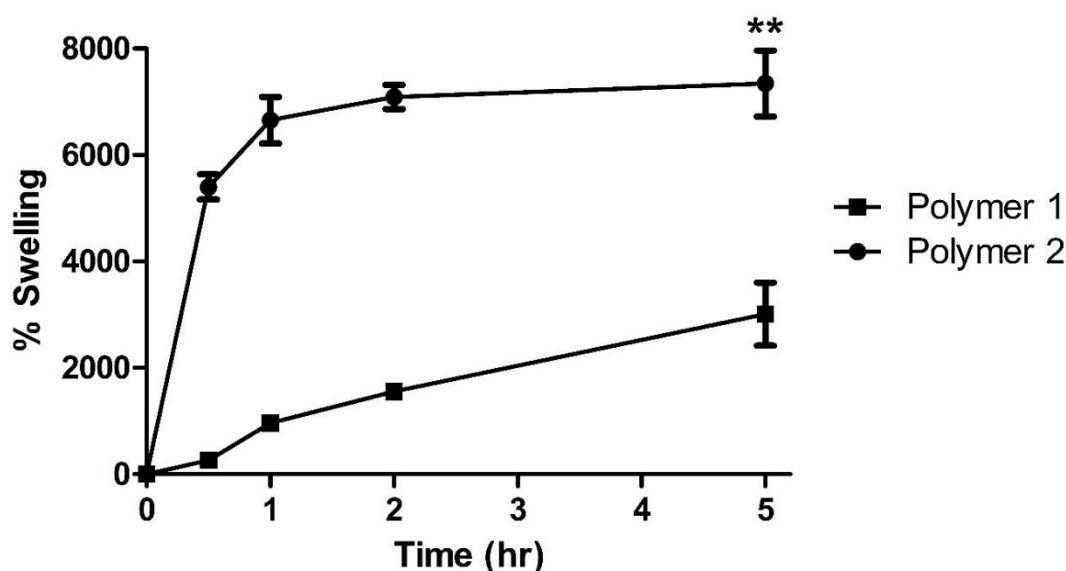
Figure 3.3 Plot showing swelling of 1cm x 1cm films of PMVE/MA based hydrogels. 5% sodium carbonate formulation dissolved. Error bars represent standard deviation where n = 3. ** $p < 0.01$ for polymer 2 v polymer 1 at 5 h.

The differences in the swelling characteristics of the three formulations can be explained by changes in crosslinking densities. Polymer **1** would be expected to have the highest cross-link density and so imbided the least fluid at equilibrium. The inclusion of 3% sodium carbonate in polymer **2** would result in a proportion of the free carboxylic acid groups of the maleic acid residues forming the sodium salt, reducing the number available to form cross links resulting in a less stiff, less dense

gel. As a result, the gel was able to swell with more fluid. In polymer **3**, given the increased amount of Na_2CO_3 there were too few free acid residues remaining to form adequate crosslinking for swelling, instead rapidly dissolving in the aqueous medium.

Based on these results, the formulation of polymer **2** was chosen for future studies, as it exhibited the highest rate of swelling and maximum swelling at equilibrium. The next step was to examine the feasibility of manufacturing MNs using this formulation.

*3.3.2 Manufacture of MNs prepared using polymer **2**.*

Templates purchased from Micropoint® Technologies were used to create MN arrays from the chosen hydrogel formulation. The templates were designed to produce 10 x 10 MN arrays with projections 350 μm in length. The MNs were manufactured by casting the blend of PMVE/MA, PEG and sodium carbonate into the templates followed by centrifugation at 800 x g for 10 mins to force the solution into the needle tips. The polymer in the templates was allowed to dry at ambient temperature for 48 hours and then placed in an oven at 80°C for 24 hours. The MN arrays were removed from the templates after cooling to room temperature (**Figure 3.4**).
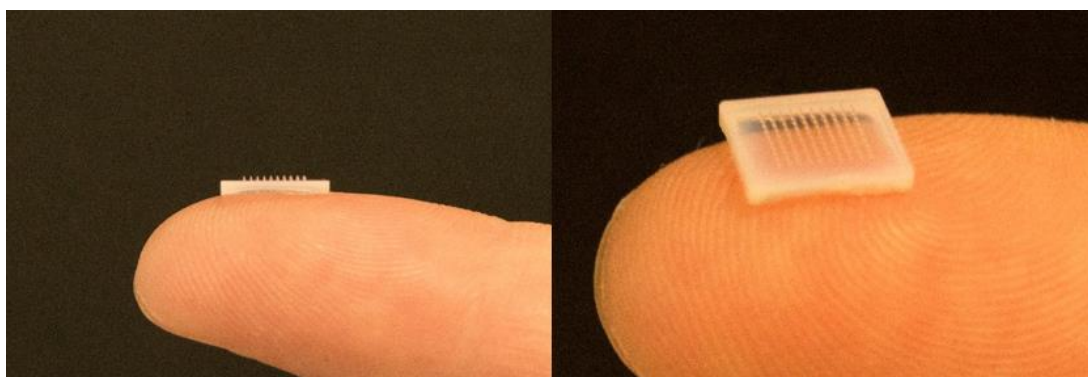
Figure 3.4 Digital photographs of 10 x 10 array of hydrogel MNs prepared from polymer 2 on fingertip. Left shows profile view and right shows view from above.

The MNs consisted of a 10 x 10 array of square based pyramidal MN projections. Each projection had a height of 348 μm ± 10.2 μm and base width 160 μm when measured by light microscopy (**Figure 3.5**). The base to base interspacing was measured as 445 μm and tip to tip distance as 590 μm.
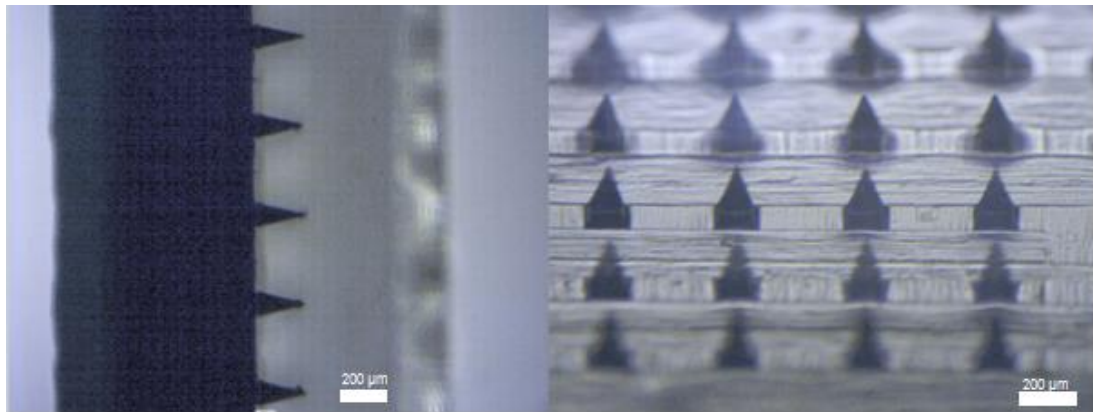
Figure 3.5 Optical microscope image of PMVE/MA hydrogel MN array. Profile view (left) and top down view (right). Scale bar is 200 µm

The MNs displayed well-formed MN projections, however, the opposite face of the baseplate had an uneven surface with sidewalls of hydrogel as a result of the moulding process. To produce MNs with an even baseplate and no sidewalls a "double filling" method was developed (**Figure 3.6**).
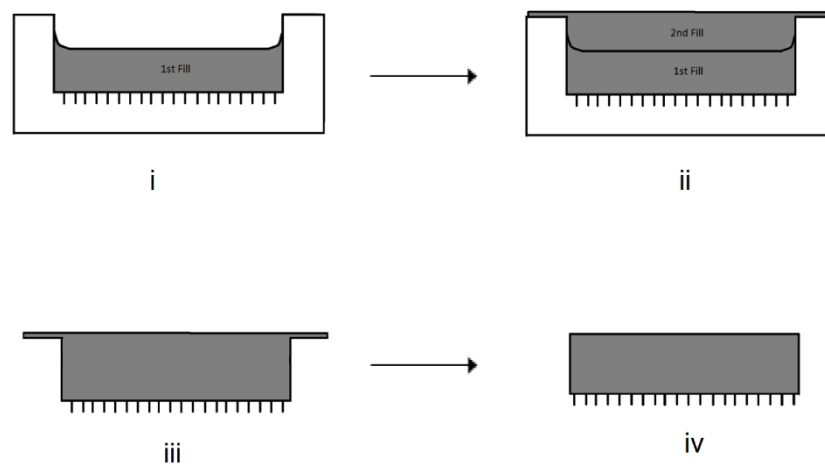
Figure 3.6 Schematic representation of MN "double fill" manufacture (i) Pre-gel blend added to mould, centrifuged and allowed to dry (ii) Second fill of pre-gel blend added to mould until slightly overflowing and allowed to dry (iii) MN crosslinked in oven then removed from mould (iv) Excess material trimmed from backplate

This involved adding 60mg of polymer **2** solution to each mould and centrifuging. This was left to dry before a second layer of pre-gel solution was added until the solution had completely filled and just flowed over the lip of each mould. After a second

drying step, the MNs were placed in the oven at 80°C for 24 hours as before and then removed from the moulds. The MNs were then trimmed to remove any material that had been overflowed onto the lip of each mould. This resulted in MNs with a more even baseplate which was an important consideration when attaching the backplate containing the sensor. The uniformity of mass for ten MNs using each method was determined (**Figure 3.7**). The average final mass of the single filled MNs was 18.3 mg ± 0.68 mg whereas the double filled MNs was 60.6 mg ± 4.83 mg. The MNs made with the double filled method consisted of more polymer as was expected and had a greater variation in weight however this was deemed as an acceptable consequence due to the advantage of the even surface to which backplates could be attached in subsequent development.
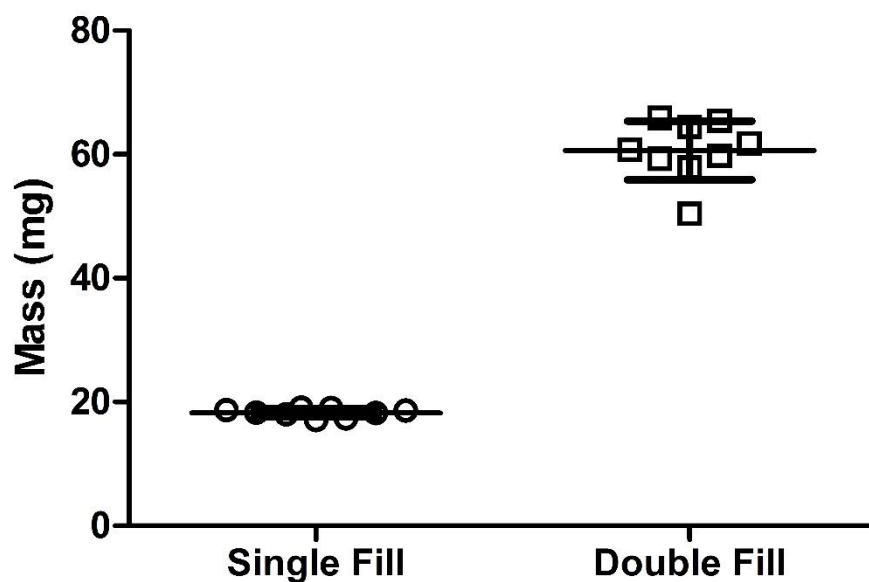
Figure 3.7 Scatter plot of final dried mass of MNs produced from single fill and double fill methods. Error bars represent standard deviations where n=10.

The ability of these MN array to penetrate the skin was investigated by using Parafilm M® as a surrogate membrane. Parafilm has previously been used as a model membrane for MN skin insertion studies[142,143] and closely resembles neonatal porcine skin with regards to penetration depth. MN arrays were inserted into five layers of Parafilm using firm thumb pressure and held in place for 30 s. The top layer of Parafilm was then removed with the attached MN remaining pierced through. The

Parafilm pierced MN was then examined using light microscopy to confirm that the MN tips had had successfully penetrated the film and remained intact (**Figure 3.8).**

Figure 3.8 Optical microscope image of 350 μm MN tips pierced through a single layer of parafilm. Scale bar is 250 μm

The mean length of each projection that was visible after penetration was 103 μm ± 12.2 μm which was approximately 30% of the total projection length. Having confirmed the ability of the highly swellable MNs to penetrate through the model Parafilm membrane, the next step was to develop the glucose sensor that could be interfaced with the MN.

3.3.3 Development of the glucose sensor.

Colorimetric glucose sensors commonly rely on the enzymatic oxidation of glucose to produce gluconolactone and hydrogen peroxide (H_2O_2) (**Figure 3.9**).
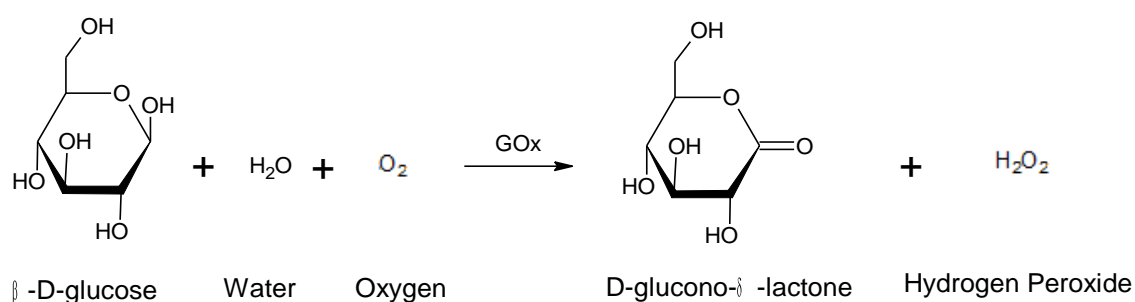
Figure 3.9 Reaction scheme of the oxidation of glucose by Glucose Oxidase to produce Hydrogen Peroxide

The peroxide, catalysed by a peroxidase enzyme, is then used to convert a colourless dye to a coloured form as described in **Section 3.1.3**. In this way the concentration of glucose can be determined from the intensity of the coloured species.

To determine the kinetics of this colour change reaction, an aliquot of glucose was added to a solution of glucose oxidase, horseradish peroxidase and TMB in sodium acetate buffer (pH 5.4) at room temperature. The absorbance spectrum of the solution was measured over the course of the reaction and plotted in **Figure 3.10.**
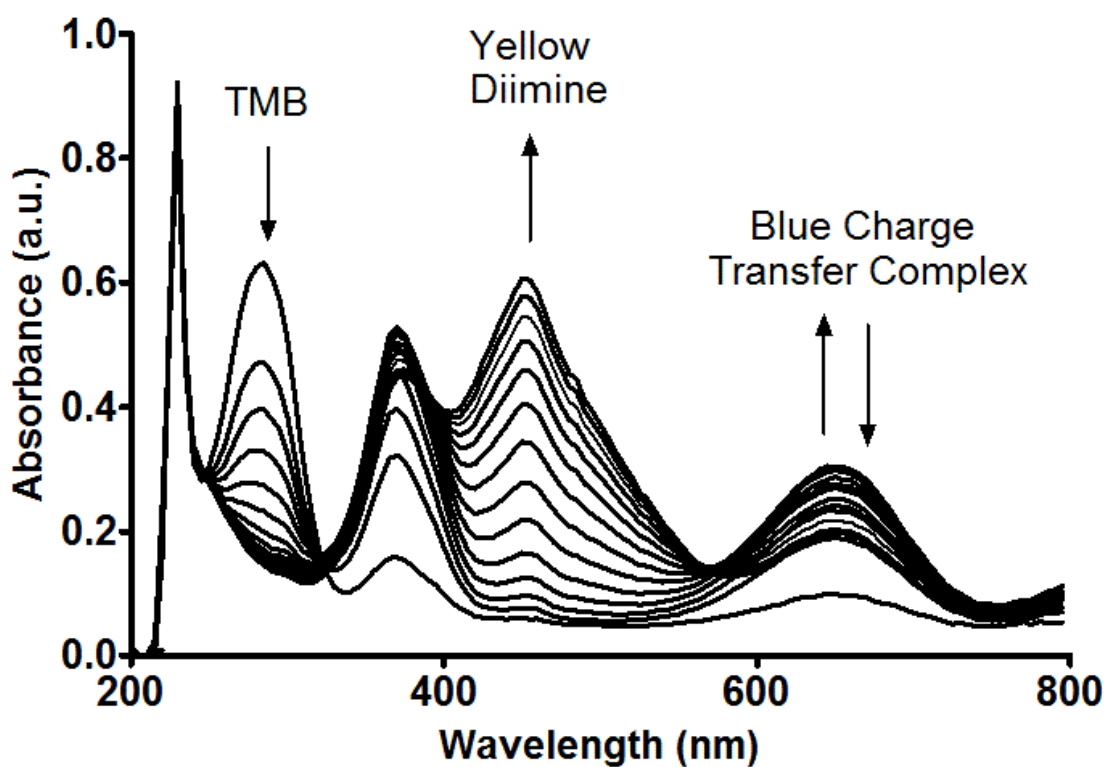
Figure 3.10 Absorbance spectra obtained following oxidation of TMB (42 μM) by hydrogen peroxide produced from oxidation of glucose by GOx/HRP (425 U/L). Measurements taken at 60 s intervals.

Initially, the absorbance at 270 nm corresponding to the colourless TMB was high, which decreased as the reaction progressed. The colourless TMB was converted to the blue coloured charge transfer complex (λ_{MAX} 650 nm) which rapidly increased intensity until it plateaued after 8 mins. This absorbance at 650 nm then began to decrease as more H_2O_2 was produced that further oxidised the blue complex to the

yellow coloured diimine. As a consequence, the decrease in absorbance intensity at 650 nm was accompanied by the appearance of a new absorbance band centred at 370 nm which continued to grow until the reaction was stopped at 15 min.

Given that the goal was to use this sensing system as a method to determine variations in glucose concertation, it was of interest to identify the time taken for the absorbance readings to reach their maximum, as a practical device would require the colour change time to be kept at a minimum. As the blue coloured complex was the dominant species in the solution, the absorbance at 650 nm was plotted separately as a function of time in **Figure 3.11**. As can be observed, using this particular ratio of enzymes to TMB, the formation of the blue charge transfer complex reached its peak after 8 min.
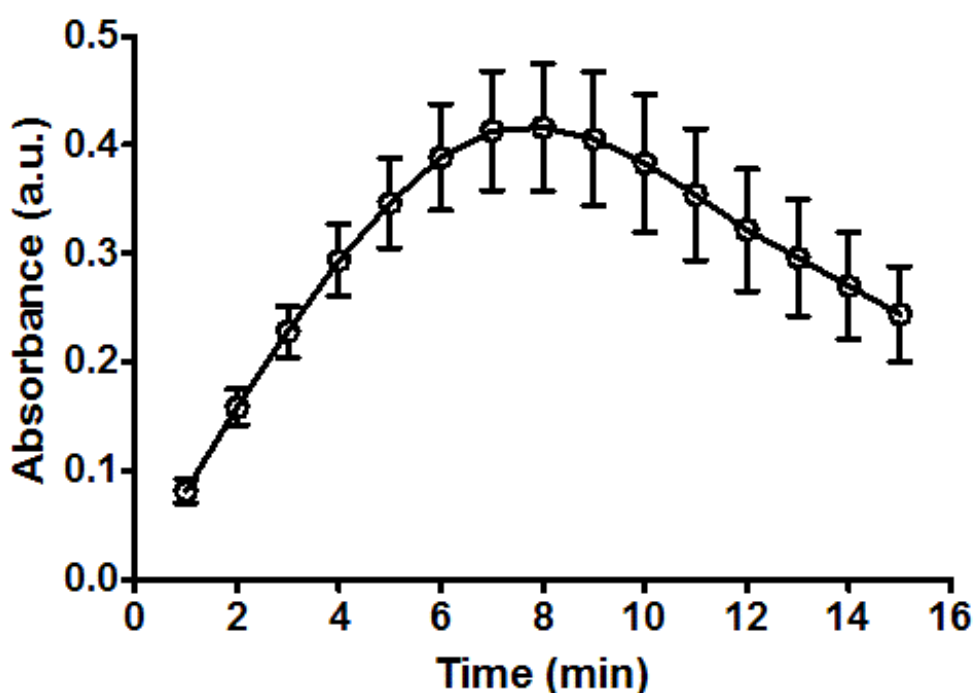
Figure 3.11 Absorbance values of solution containing GOx/HRP (425 U/L) and TMB (42 µM) in sodium acetate buffer (pH = 5.4) at 650 nm showing formation of charge transfer complex over 15 mins. Error bars represent standard deviation where n=3

To determine if the rate of blue charge transfer complex formation could be reduced, the concentration / ratio of enzymes and TMB were modified, with the absorbance at 650 nm measured over the course of 15 min. **Figure 3.12** shows the results when

the TMB concentration was kept constant but the concentration of the enzymes were doubled to 850 U/L. The results reveal that the peak charge transfer complex concentration is reached in a shorter period of time (3 mins) while the maximum absorbance intensity remained unchanged. In contrast, if the TMB concentration was doubled to 84 µM and the enzyme concentration kept constant, the time to reach peak absorbance at 650 nm was extended because the rate of oxidation was not increased. If both the enzyme and TMB concentrations were increased to 850 U/L and 84 µM respectively the peak absorbance was still reached in 8 mins, but the intensity of absorbance at 650 nm was increased to 0.86 indicating more charge transfer complex was formed.
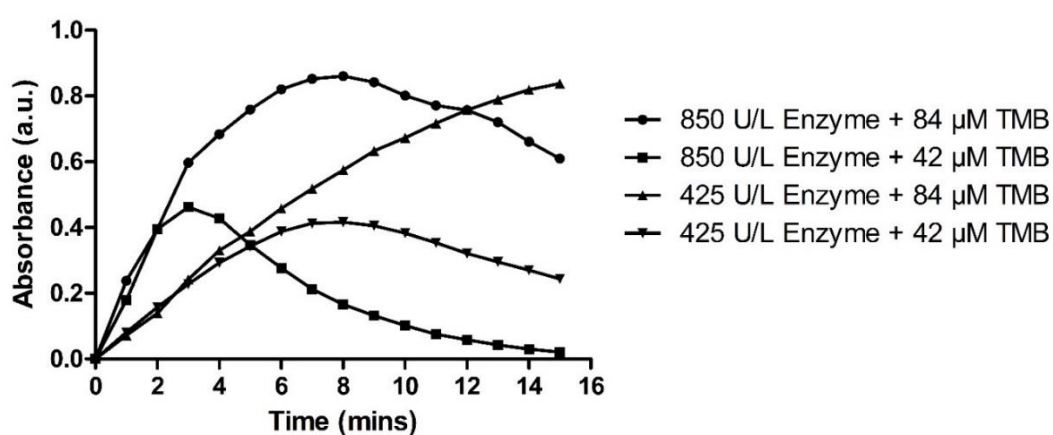
Figure 3.12 Absorbance at 650 nm showing formation of charge transfer complex over 15 mins using different ratios of GOx/HRP and TMB

When increasing concentrations of glucose (0 – 1000 µM) were added to GOx/HRP (425 U/L) and TMB (42 µm), the plot of absorbance at 650 nm showed a linear relationship (R^2 = 0.99) when measured at 8 mins between 0 – 200 µM (**Figure 3.15**), however this linearity broke down at higher concentrations (200 – 1000 µM) as shown in **Figure 3.13**.
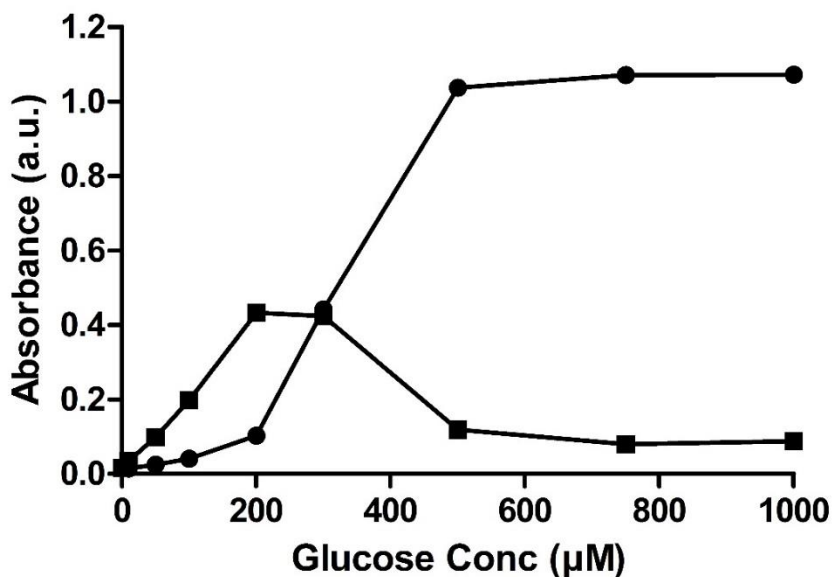
Figure 3.13 Absorbance values of solutions containing GOx/HRP (425 U/L), TMB (42 µM) and increasing concentrations of glucose (0 – 1000 µM) in sodium acetate buffer (pH = 5.4) Absorbance at 650 nm shows formation of charge transfer complex. Absorbance at 460 nm shows formation of diimine.

This loss of linearity can be explained by the formation of the second oxidation product, the yellow diimine. The distinctive colour change from blue to yellow has an intermediate green colour which is simply an approximately equal mixture of both structures (**Figure 3.14**).
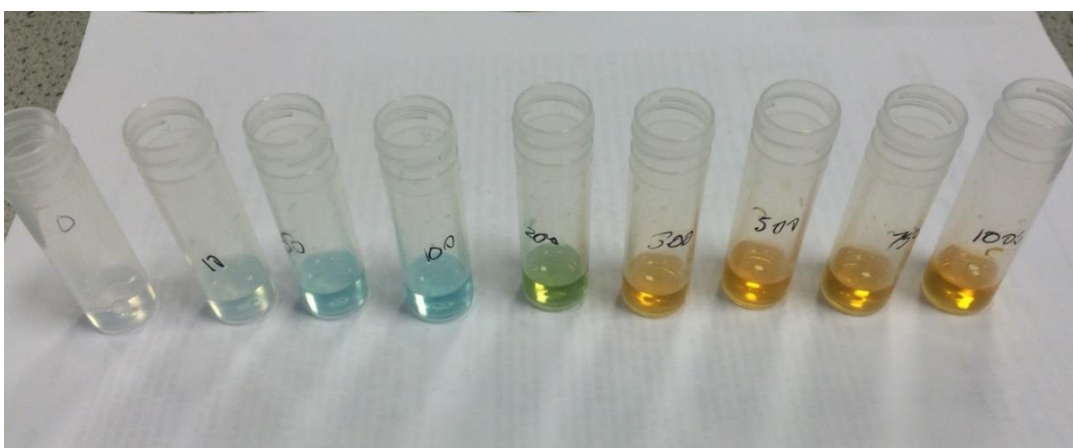
Figure 3.14 Photograph of solutions of GOx/HRP (425 U/L) and TMB (42 µM) spiked with increasing concentrations of glucose (0 - 1000 µm) in sodium acetate buffer (pH=5.4). Photograph taken after 8 mins

To effectively use the blue colour present to determine the concentration of glucose visually, the intensity of colour must be directly proportional to the glucose concentration. This means that the sensor system using this ratio of GOx/HRP to TMB could be used to determine glucose concentrations between $0 - 200$ µM, as the relationship between the absorbance and the glucose concentration had acceptable linearity over this range. (**Figure 3.15**).
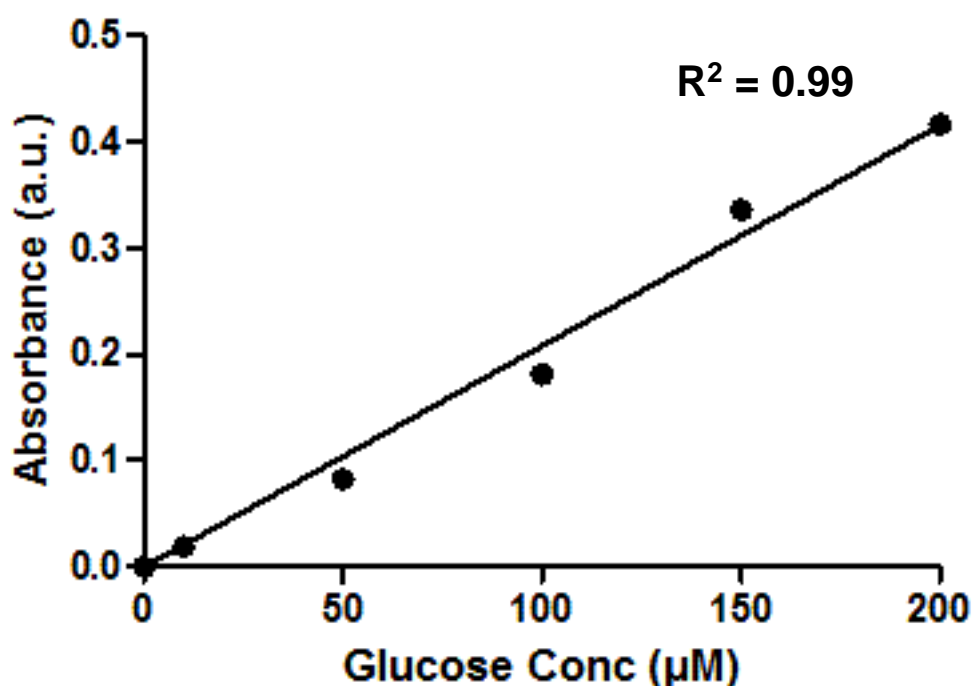
Figure 3.15 Plot of linear range of absorbance at 650nm at 8 mins after addition of increasing concentrations of glucose to GOx/HRP (425 U/L) and TMB (42 µM) in sodium acetate buffer (pH = 5.4)

To extend the linearity range and thus the range of glucose that could be detected visually, the formation of the yellow coloured diimine must be avoided when measuring higher concentrations of glucose within the given time frame. As the diimine is formed through the second oxidation of the blue charge transfer complex, reducing the rate of oxidation can reduce its likelihood to form. One way to decrease the rate of oxidation was to decrease the concentration of the GOx/HRP but keep the concentration of TMB constant. Adopting this approach, **Figure 3.16** shows that the

linear region can be extended across the entire 0 – 1000 µM range by decreasing the concentrations of GOx/HRP from 425 U/L to 106 U/L.
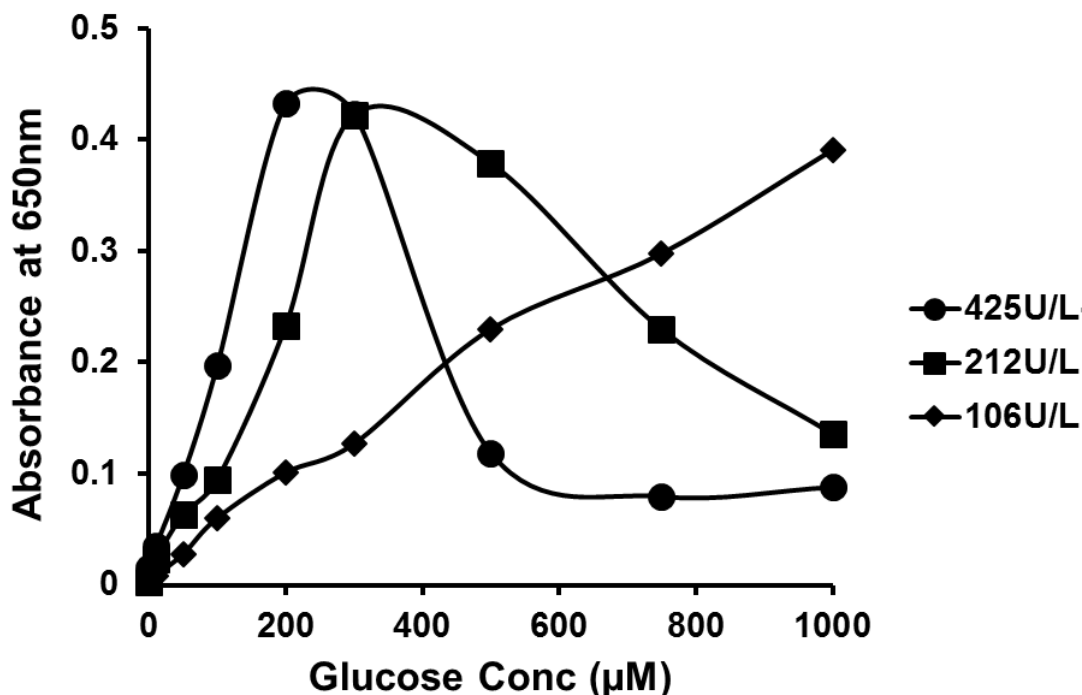
Figure 3.16 Absorbance of solutions containing 425 U/L, 212 U/L and 106 U/L of GOx/HRP and TMB (42 µM) 8 mins after addition of increasing concentrations of glucose in sodium acetate buffer (pH=5.4)

This decreased the formation of the diimine within the 8 mins despite the higher concentrations of glucose. From these experiments it was concluded that the ratio of the enzymes GOx/HRP to the concentration of TMB could be varied to control range of glucose concentration that could be determined by monitoring the formation of the blue coloured charge transfer complex. By finding the correct ratio of GOx/HRP to TMB the intensity of the blue colour formed at a given time point could be used to determine glucose concentration within the physiological range (0 - 10 mM). However, the kinetics of this reaction would vary depending on the substrate in which it occurred. As it was carried out in an aqueous buffer at pH 5.4 it was deemed not essential to find the correct ratio of GOx/HRP to TMB to show a linear colour change within the physiological glucose concentration at this point as this would change when the reaction was carried out in a different substrate such as

a hydrogel or solid matrix, which would be necessary to interface with the hydrogel MN.

3.3.4 Interfacing sensor with hydrogel MN

The matrix chosen to house the sensor system was required to have excellent water transfer abilities, be compatible with pH sensitive and thermolabile enzymes and have the ability to be integrated with the hydrogel MNs. The PMVE/MA hydrogel was initially considered as a candidate to create a hydrogel backplate that could be attached to the opposite face of the baseplate from the MN projections as it had been demonstrated to be highly swellable. While the enzymatic glucose sensor did remain active when added to the pre-gel blend of PMVE/MA and PEG, as demonstrated by the addition of 10 mM glucose solution (**Figure 3.17**), the act of heating the polymer after drying to induce chemical crosslinking rendered the enzymes inactive.

(a)   (b)   (c)
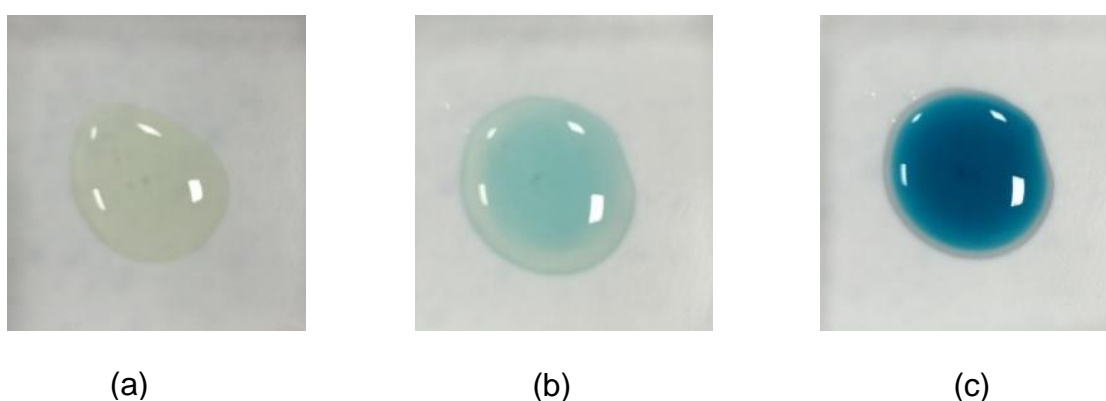
Figure 3.17 Digital photographs of pre-gel blends containing GOx/HRP and TMB (a) before addition of glucose (b) 4 mins after addition of 10mM glucose (c) 8 mins after addition of 10 mM glucose

The addition of the enzymatic sensor to the hydrogel after crosslinking was possible by submerging a crosslinked xerogel in a solution containing the sensor and allowing the hydrogel to imbibe the fluid. After it had become fully swollen, surface water was removed with filter paper and a 10mM glucose solution was pipetted on to the gel. A colour change was observed with the yellow diimine being visible (**Figure 3.18**).

(a)   (b)   (c)
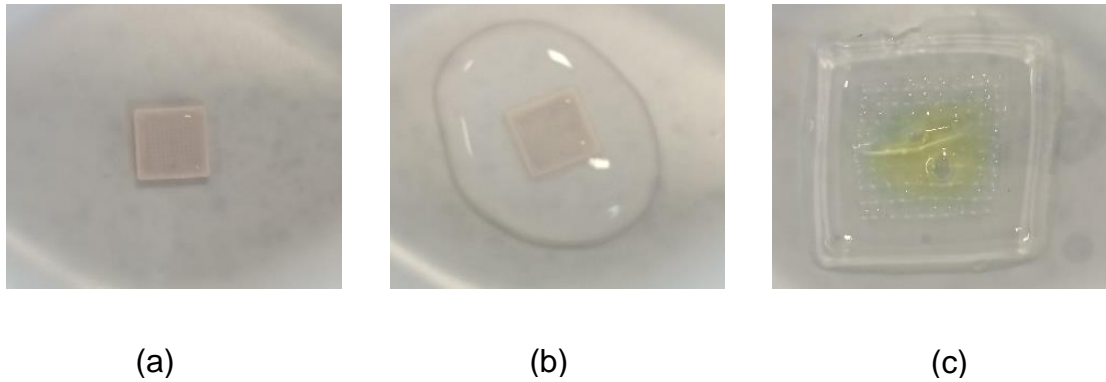
Figure 3.18 Digital photographs of addition of GOx/HRP and TMB to crosslinked hydrogels to produce colour change after glucose. (a) Crosslinked PMVE/MA based hydrogel in dried state (b) swelling hydrogel in aqueous solution containing GOx/HRP and TMB (c) swollen hydrogel 5 mins after addition of 10 mM glucose

In order to prepare a backplate from the sensor swollen xerogel, it was allowed to dry at ambient temperature under a constant air flow to aid evaporation for 4 hours. The resultant film was then cut to size and attached to the back on a hydrogel MN with a small amount of distilled water to aid adhesion (1 µL). The MN-sensor backplate assembly was then pierced through a layer of Parafilm and placed on top of a 10 mM glucose solution (**Figure 3.19**). This *in vitro* experimental set up was used as a simple method to determine if the MN tips could swell with sufficient solution to transfer the glucose into the backplate and interact with the sensor to produce a colour change.
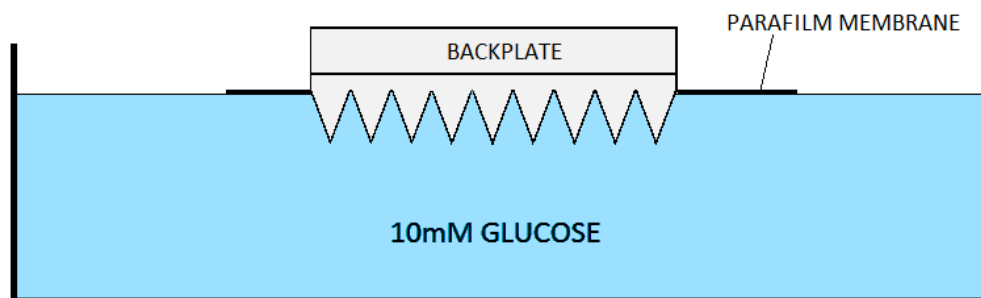
Figure 3.19 Schematic diagram of *in vitro* experimental set up to investigate the ability of PMVE/MA MN with hydrogel backplate containing glucose sensor to extract solution from reservoir containing 10 mM glucose

Figure 3.20 shows the results of this study with a blue/green colour change observed in the backplate after 60 min, which indicated that the enzymes remained active following incorporation within the dried polymer film. In F**igure 3.20**, the backplate was covering only a portion of the MN baseplate and the colour was only observed in that region.

(a)   (b)
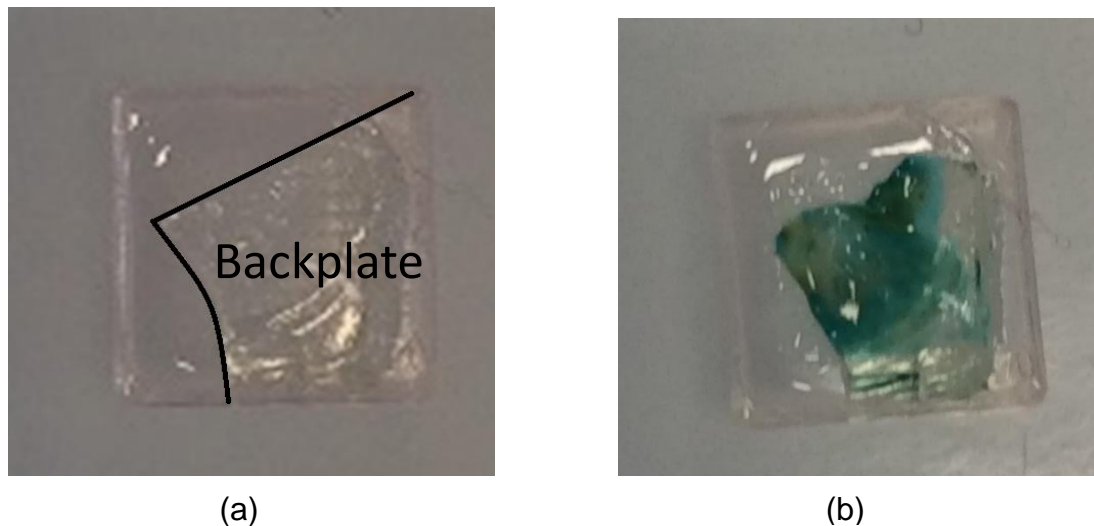
Figure 3.20 Digital photograph of PMVE/MA MN with hydrogel backplate containing GOx/HRP and TMB pierced through Parafilm and placed on top of aqueous solution containing 10mM glucose (a) line showing partial coverage of baseplate with hydrogel backplate (b) after swelling with aqueous solution containing 10 mM glucose and production of blue/green colour change

While using this method to form a backplate did show some encouraging results, there was a number of issues in using PMVE/MA crosslinked with PEG. The need to swell the polymer with the sensor and then allow it to dry meant it was difficult to control the shape and texture of the resultant film. A simpler method would involve the incorporation of the glucose sensor into the polymer before casting it into a mould and drying to allow the production of films with predetermined dimensions. This would require a polymer film that could be created without the need for elevated temperatures and with a pH of between 4 and 7. One such polymer film consists of PMVE/MA and TPME. This film was produced by adding TPME to a solution of PMVE/MA and adjusting the pH to 5.4 using NaOH. To this solution was added GOx/HRP and TMB which was then cast into the MN moulds to match the exact dimensions of the hydrogel MNs. Importantly, the moulds were not centrifuged after addition of the solution in order to produce polymer film squares that did not have MN projections. These backplates were allowed to dry under constant air flow

and attached to the MN baseplate as before. When tested *in vitro* as in **Figure 3.19,** a green colour was observed once more, but it still required approximately 50 mins (**Figure 3.21**).

The addition of TPME to the PMVE/MA has been used previously as a plasticiser to increase the flexibility of the film rather than a crosslinker[144]. Indeed, the structure of TPME (**Figure 3.22**) shows the presence of only one free hydroxyl (-OH) group.

(a)   (b)
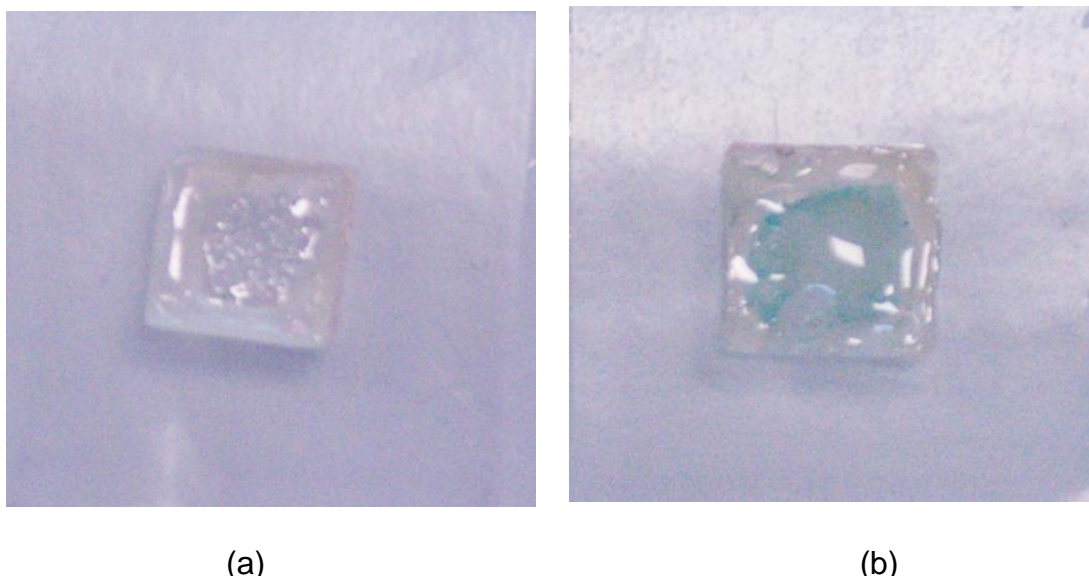
Figure 3.21 Digital photograph of PMVE/MA MN with PMVE/MA and TPME based backplate covering entire baseplate area (a) before swelling (b) after swelling for 50 mins
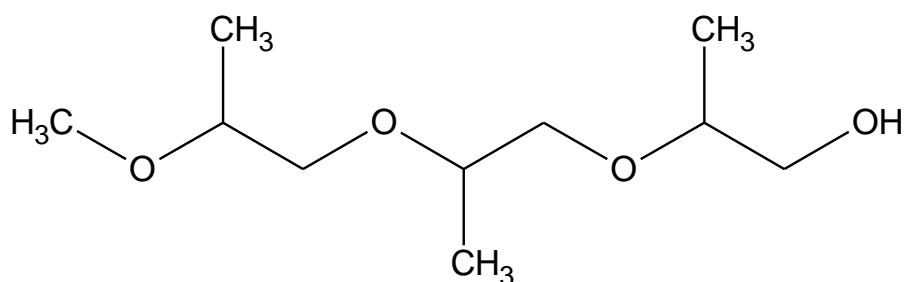
Figure 3.22 Structure of TPME used as a plasticiser in the PMVE/MA film

As a result, no covalent crosslinks could be formed between the separate PMVE/MA backbones, unlike with PEG. This resulted in a flexible film which remained water soluble and thus absorbs less fluid before dissolving.

3.3.5 Optimisation of hydrogel MN with backplate in vitro

While the integration of the sensor and MN successfully generated a colour change in response to glucose after 50 mins, for a point of care device it is preferable for the results to be available extremely rapidly, for example after 60 seconds. To achieve this goal, the following two limitations of the device were identified:

(i)   The rate at which the backplate absorbed the solution and produced a colour change.

(ii)   The rate at which the MN imbibed the solution.

Both of these limitations were investigated in turn for further optimisation.

3.3.5.1 Improving the rate at which the backplate absorbed the solution and produced a colour change.

It was observed that the hydrogel polymer backplates did provide a substantial delay in the time between the MN swelling and the colour change occurring, therefore other platforms to house the glucose sensor rather than hydrogel based backplates were investigated. Paper was identified as an ideal candidate due to its low cost, excellent water transporting capabilities and widespread use in colour based sensors[145]. The initial white colour of the paper provided an excellent contrast for colour intensity to be determined by the naked eye and aqueous solutions are quickly drawn into dried paper networks through capillary action between the interconnected strands of paper fibres[146].

To create sensor embedded paper backplates, paper squares (Whatman No. 1 filter paper) measuring 1cm^2 were submerged in solutions of GOx/HRP and TMB (50:50 distilled water: ethanol) for 5 mins. The backplates were then removed and allowed to air dry at room temperature for 60 mins. An experiment was conducted to determine the ideal concentrations of GOx/HRP and TMB to be used. The goal was to achieve a rapid colour change that was easily visible to the naked eye within 30 s to shorten the time to response. Four formulations were investigated as seen in **Table 3.1**. To observe the response of each backplate, an aliquot (5 µL) of a 10 mM glucose solution was added and photographs of each backplate at defined time

points were taken. The experiment was repeated and both sets of photographs at 0s, 30s and 60 s from are shown in **Figure 3.23**.

Table 3.1 Four formulations used to produce glucose responsive paper backplates

Formulation	GOx (U/L)	HRP (U/L)	TMB (mM)
A	8.5	1.7	3.33
B	85	17	3.33
C	850	170	3.33
D	8500	1700	3.33
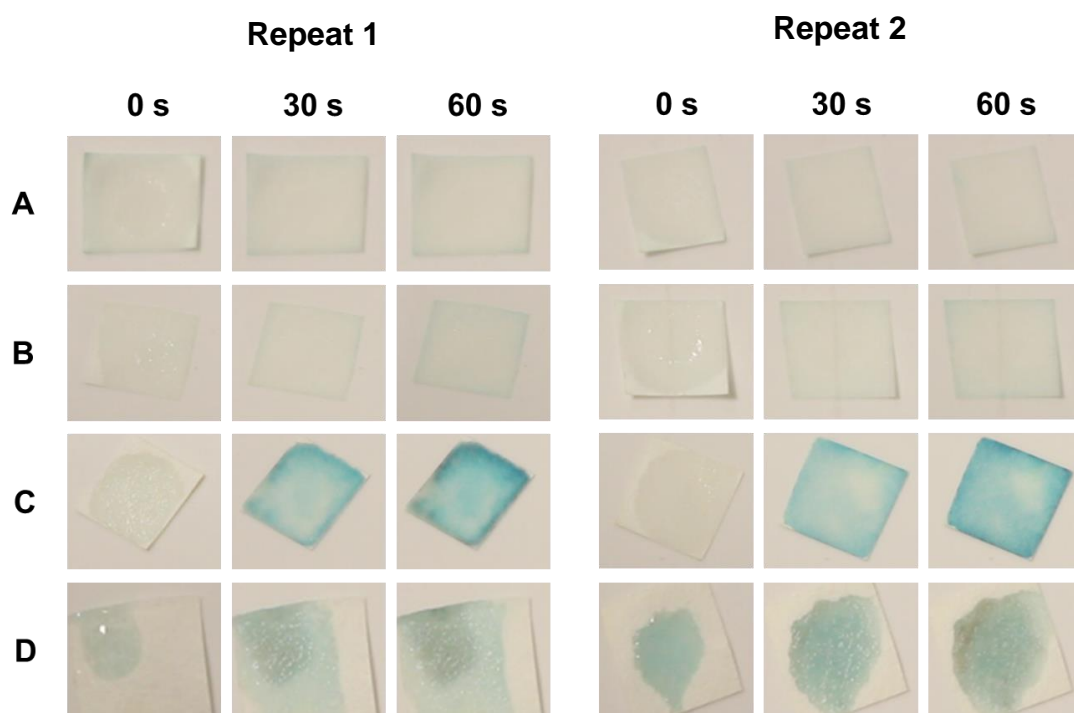
Figure 3.23 Digital photographs of colour change in paper backplates produced using formulations A – D over time following addition of a 5 μL aliquot of 10 mM glucose. Results shown from two repeats (left and right).

Both formulations A and B generated little to no visible colour change within 60 s. An easily visible colour change was visible with formulation C after 30 s and this increased in intensity at 60 s. Formulation D caused a rapid colour change, however, the colour was less uniform and less easily visible. As each formulation had the same concentration of TMB the differences observed must have been due to the enzyme

concentration. Formulations A and B had a low concentration of GOx and HRP and, therefore, relatively little TMB was oxidised within 60 s. It was observed that at later time points, e.g. 8 mins (**Figure 3.24**) a colour change did occur with both formulations, with B providing a more intense change.
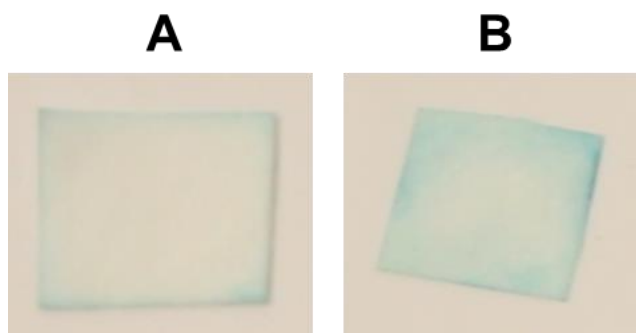
Figure 3.24 Digital photographs of paper backplates made from formulation A and B 8 mins after addition of glucose showing colour change

Formulation C showed the most promising results as a visible colour change was produced at 30 s that was reasonably uniform and covered the entire backplate. The non-uniformity of the colour change in D may be explained by the extremely high concentration of GOx and HRP forming a suspension in the solution used to make the backplates, resulting in uneven deposition of the enzymes across the backplate. C was chosen as the lead formulation to pair with the 350 µm hydrogel MN to retest *in vitro* and determine any improvement in performance.

Paper backplates prepared using formulation C were attached to the back of hydrogel MNs and the time taken for a colour change to occur using the previous *in vitro* method was measured. A decrease from the previous time (50 mins) using the hydrogel backplate was observed with the initial wetting of the backplate appearing after a mean time of 28.5 mins ± 3.9 mins from placing the MNs in contact with the 10 mM glucose solution through Parafilm. The fluid was observed to contact the paper backplate from a single point and quickly became dispersed throughout the entire backplate due to capillary action inherent to the material (**Figure 3.25**). The blue colour change began to occur as the TMB was oxidised within 60 s from the initial wetting. From these results, paper was identified as a suitable platform to house the glucose sensor for subsequent studies as it produced a colour change

within a much shorter period of time compared to previous hydrogel backplates and due to the facile nature of producing a large quantity of backplates with relatively low cost.

Figure 3.25 Digital photographs of paper backplates attached to 350 µm MN pierced through parafilm and placed on 10 mM glucose solutions (a) initial wetting of backplate (b) 20 s after wetting (c) 40s after wetting (d) 60s after wetting

3.3.5.2 Improving the rate at which the MN imbibed the solution.

Following the identification of a MN sensor backplate with rapid colour change kinetics, attention was turned to improving the extraction capabilities of the hydrogel MN. Some initial optimisation was achieved by using sodium carbonate as a crosslinking density modifier, thus increasing the rate of swelling. However, additional steps were required to shorten the time to response further. Considering the dimensions of the MN, the length of the MN projections were thought to be a significant factor in the rate at which fluid would be imbibed into the MN baseplate and subsequently the backplate. Previously, it was be determined that an average of 103 µm of each MN projection penetrated through the parafilm membrane and, therefore, only this portion would be in contact with the aqueous solution. By increasing the length of the MN projections, a greater amount of the swellable hydrogel would be exposed to the solution and the rate of uptake may be increased. When applied to an *in vivo* system i.e. human skin, the MN projections would penetrate further into the viable epidermis and upper layers of the dermis and so contact more ISF.

To this end, moulds to produce MN arrays of increased length were purchased. The mould specifications listed a length of 800 μm. These MNs were produced in the same manner as the shorter MNs using polymer **2** (**Figure 3.26**).

(a)   (b)
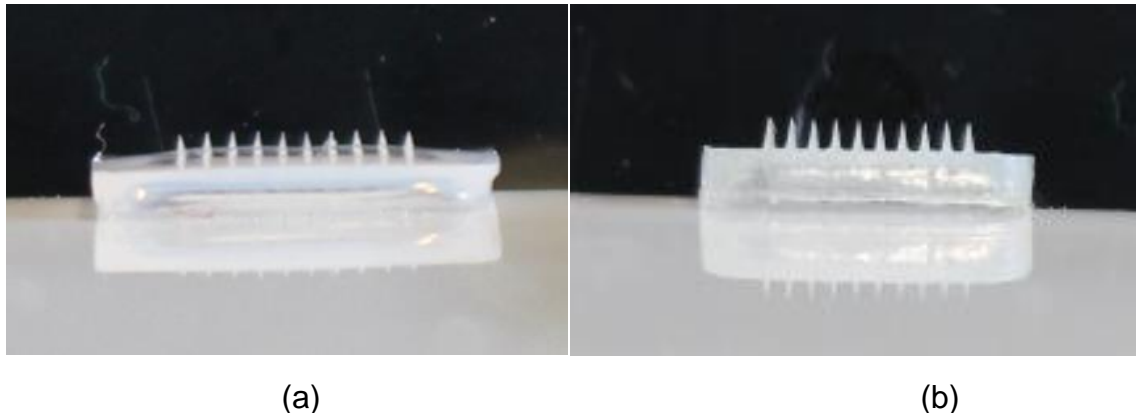
Figure 3.26 Photographs of Polymer **2** PMVE/MA hydrogel MNs (a) 350 μm MN length   (b) 800 μm MN length

Light microscopy was used to confirm good replication from the moulds with a mean needle length of 803 μm ± 15.6 μm and mean base width of 335 μm. (**Figure 3.27**). Base to base interspacing of 288 μm and tip to tip distance of 588 μm.
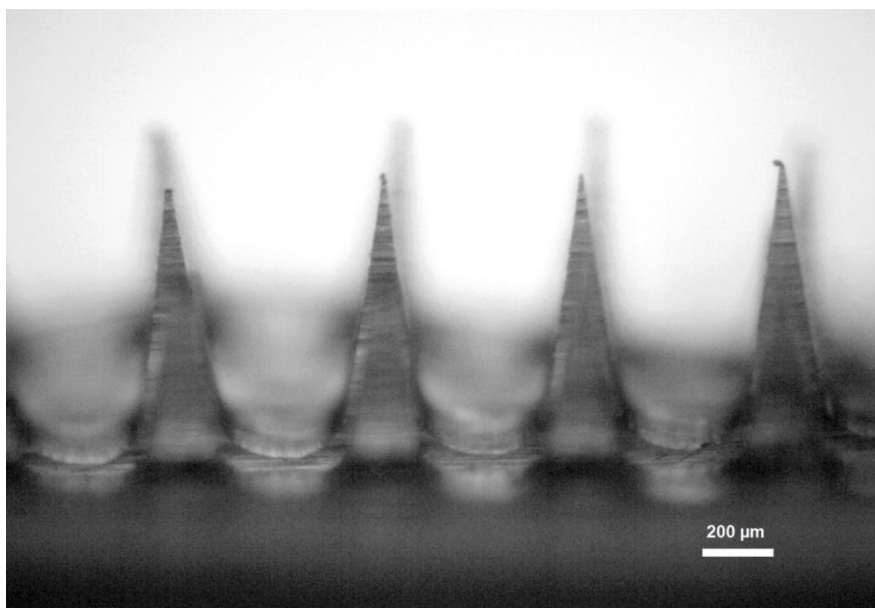
Figure 3.27 Light microscope image of PMVE/MA hydrogel MN with 800 μm length MNs. Scale bar is 200 μm

The MN arrays were also pierced through Parafilm and photographed as before (**Figure 3.28**). It was confirmed that the projections did penetrate while remaining intact. When comparing the length of each projection exposed after piercing through

a single layer of Parafilm, a significant increase was observed for the longer MN with a mean of 235 µm ± 37.6 µm compared to the shorter MNs that had a mean length of 103 µm ± 12.2 µm.
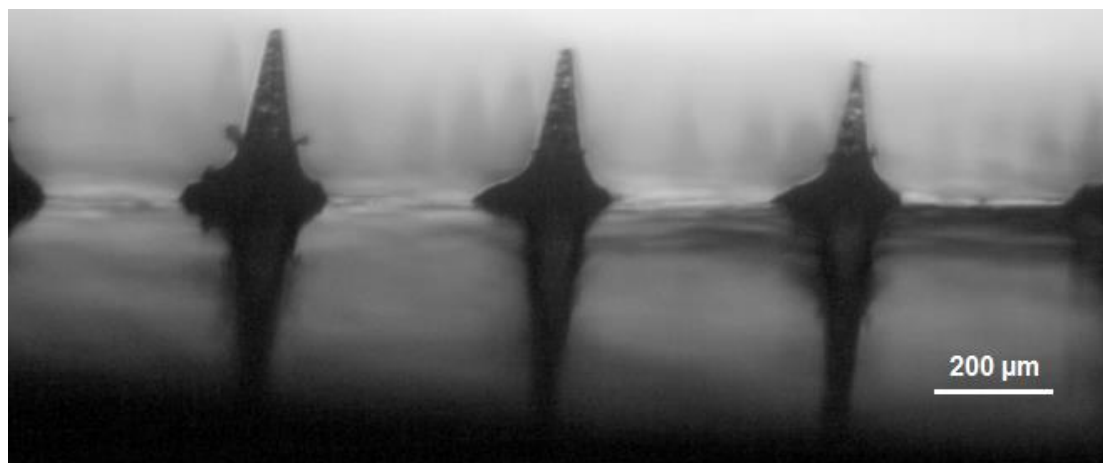
Figure 3.28 Light microscope image of 800 µm MN tips penetrating through a single layer of parafilm. Scale bar is 200 µm

To evaluate if increasing the length of the MN projection increased the rate of glucose extraction, glucose sensor embedded paper backplates were attached to the MN baseplate as before, pierced through a single layer of parafilm and placed on the surface of a 10 mM glucose solution. Initial wetting of the paper backplate occurred after 21.2 mins ± 3.6 mins following addition of the MN and the colour change occurred within the next 60 s as observed in the shorter MNs (**Figure 3.29**).
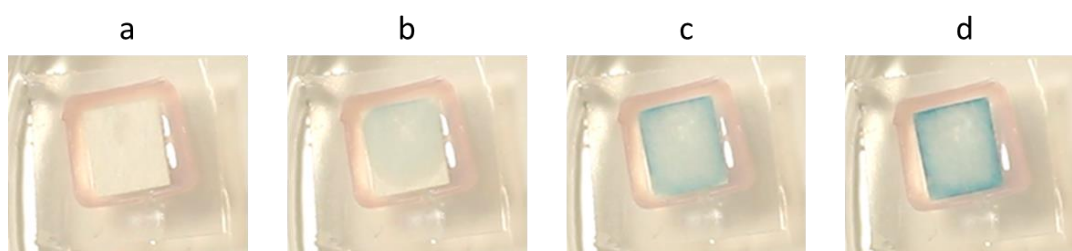
Figure 3.29 Digital photographs of paper backplates attached to 350 µm MN pierced through parafilm and placed on 10 mM glucose solutions (a) initial wetting of backplate (b) 20 s after wetting (c) 40s after wetting (d) 60s after wetting

105

These results highlight that increasing the length of the MN projections from 350 μm to 800 μm reduces the time taken for the MN to extract the aqueous solution by 7 mins from 28.5 mins ± 3.9 mins to 21.2 mins ± 3.6 mins. **Figure 3.30** illustrates how the changes in the MN and backplate described in this chapter decreases the time taken to produce a colour change in the sensor backplate.
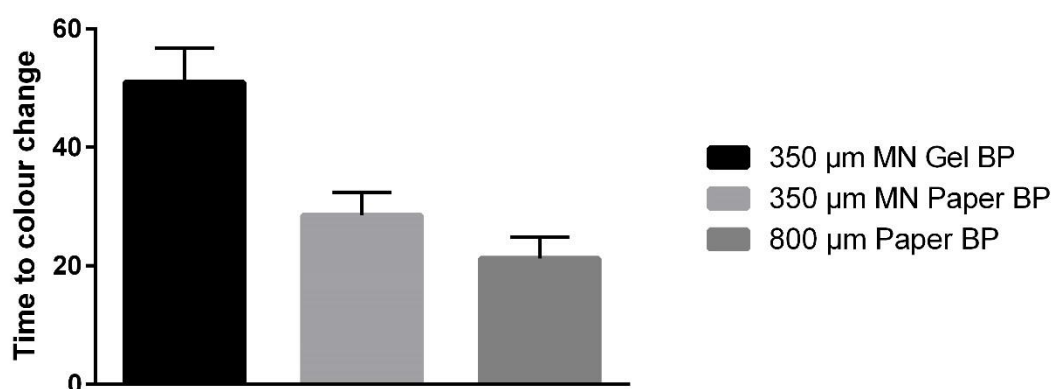
Figure 3.30: Time for colour change to occur in glucose extraction in 350 μm length MNs arrays with TPME backplate, paper backplate and 800 μm length MNs with paper backplate.

There have been a number of MNs with PMVE/MA used as the main copolymer with crosslinking polymers other than PEG. For example, hyaluronic acid (HA), a glycosaminoglycan, has been covalently crosslinked with PMVE/MA to form hydrogel MNs[147]. The polymer films demonstrated sustained release of methylene blue (MB) used as a model compound over 50 h. The polymer films also exhibited the ability to rapidly swell with aqueous solutions similar to the PMVE/MA and PEG hydrogels discussed in this chapter. In fact, the rate of swelling was greater in the HA containing polymer films as they reached their maximum equilibrium in 15 mins however the overall swelling capacity was substantially lower (1400% w/w) than the PEG containing polymer in this work.

Pectin has also been used as a crosslinker in PMVE/MA based hydrogel MNs[148]. While the crosslinking mechanism was reportedly due to esterification between the free acid residues of the PMVE/MA and free hydroxyl groups present on the pectin macromolecules, the swelling rates of the polymer films were substantially slower then PEG crosslinked films. The swelling studies were conducted over 7 days with the maximum swelling percentage observed to be 4951% w/w. While this is comparable

to the swelling percentage at equilibrium of the PEG crosslinked films, it is substantially slower in swelling rate.

3.4 Conclusion

In this chapter, highly swellable MN arrays composed of PMVE/MA, PEG and sodium carbonate were produced using a micromoulding technique. MN arrays with both 350 µm and 800 µm projections in 10 x 10 arrays were successfully produced and were sufficiently robust to remain intact following penetration through a Parafilm membrane.

An optical detection system for glucose was developed composed of GOx/HRP and TMB. The sensor utilised the production of hydrogen peroxide from the oxidation of glucose to produce a visible colour change. The oxidation of the TMB by the hydrogen peroxide was catalysed by HRP to form a blue coloured charge transfer complex. Upon further oxidation, the yellow coloured diimine species was observed. The sensor was interfaced with the MN, initially using a hydrogel backplate platform. These MNs were tested *in vitro* and successfully indicated the presence of glucose in simulated ISF within 50 mins, via a blue colour change that was visible to the naked eye.

Multiple optimisation steps were undertaken in order to improve the overall time required for observation of the colour change following addition of the MN to a glucose solution. By optimising the ratio of sensor components (i.e. enzymes and dye etc.) and utilisation of a paper based substrate to house the sensor as a MN backplate, the overall response time was almost halved from 50 min to 28.5 mins ± 3.9 mins. By increasing the length the MN projections from 350 µm to 800 µm, the time was further decreased to 21.2 mins ± 3.6 mins.

While substantial improvement in the response time was achieved by these optimisation steps, for practical use as a POC device the response time must be extremely rapid. The major limitation observed was the time necessary for the PMVE/MA hydrogel MN to extract the aqueous solution and bring it into contact with the backplate.

In the following chapter, the use of a hollow MN was investigated to determine if the extraction kinetics could be improved when compared to the hydrogel MNs.

4.0 Single Hollow Microneedle Device for the Extraction and Colorimetric Detection of Glucose

4.1 Introduction

As identified in Chapter 3, one of the major challenges of designing POC MN device for glucose is the time taken for the hydrogel MN to imbibe fluid and transport it to the detection system. For a POC device, the measurement must be obtained within a reasonable time frame so the result accurately reflects the current analyte levels in the body. Glucose concentrations in the plasma and, therefore, the ISF can rapidly increase or decrease according to the insulin-glucagon cycle while the measurement from the MN is being obtained. Therefore, it is imperative that the measurement is obtained as quickly as possible after the test commences to ensure an intervention can be made if necessary. In this chapter, hollow MNs as an alternative to PMVE/MA hydrogel based MNs were investigated to determine their ability to rapidly transport simulated ISF to the detection system.

Hollow MNs can made from monocrystalline silicon using MEMS technology. In one example, hollow silicon MNs that have successfully demonstrated the withdrawal of ISF from the skin in 15 – 20 mins using capillary action have been prepared[125]. These were manufactured by initially spinning a pattern of photoresist (SU-8) onto a silicon wafer leaving an array of circular areas of the silicon exposed. Then, using Deep Reactive Ion Etching (DRIE), channels that would become the lumen of the hollow MNs were etched into the wafer in the exposed silicon crystal. The MN projections were cut into columns by a micro-controlled diamond saw blade before sharpening of the columns into MN projections using an isotropic etching technique with a mixture of hydrofluoric, nitric and acetic acid. This produced 2D arrays of hollow MNs composed of silicon that were inserted into the skin of human subjects. The arrays were capable of extracting ISF, which was confirmed through optical microscopy and analysis of glucose in the fluid extracted.

Another method to prepare hollow MNs is through the use of metal electrodeposition[149,150]. Solid SU-8 MNs were prepared using photolithography with a dark exposure mask in the pattern of the 2D array of needles and UV light. The MNs were then fully coated with a conductive layer of poly (methyl methacrylate) and carbon black. In order to create open hollow MNs the arrays were exposed to O_2/CF_4 plasma which eroded the conductive polymer away from the MN tips and exposed the SU-8 beneath. The arrays were then electroplated with nickel for structural strength and then gold for biocompatibility. This was achieved by submerging the conductive MN arrays in an electroplating bath and applying a voltage between the arrays and a metal electrode, which were composed of either nickel or gold. After the electroplating steps, the metal layers were separated from the other layers to create the hollow metal MN arrays.

Both of these methods were successful in producing hollow MNs but require the use of highly specialised and costly materials and equipment. Silicone micromoulding may provide a more convenient and less costly method to create hollow MNs. However, the challenge of creating a master template from which to create the silicone mould must be addressed. In this chapter, the use of a hypodermic needle as a template in combination with 3D printing technology is investigated in order to develop a single hollow MN device.

Additionally, a method to quantify the colorimetric response of the detection system was investigated in this chapter and involved recording digital photographs of the backplate followed by subsequent analysis using image processing software, ImageJ. This method compliments the use of naked eye detection as used in **Chapter 3**.

4.2 Aim and Specific Objectives

The aim of the work undertaken in this chapter was to prepare a hollow MN from polymerised glycidyl methacrylate (GMA) crosslinked with triethyleneglycol dimethacrylate (TEGDMA) and trimethylolpropane trimethacrylate (TRIM), hereafter referred to as **1**. Subsequently, the MN was integrated with a paper-based colorimetric based GOx/HP and TMB glucose sensor and the kinetics of simulated ISF

withdrawal using this device was investigated. The ability of the device to accurately discriminate between various different glucose concentrations was also determined.

The specific objectives were:

i. Manufacture a hollow MN device composed of **1** that could transport simulated ISF containing glucose to the backplate

ii. Determination of the kinetics of fluid withdrawal using the MN.

iii. Mechanical analysis of the robustness of the MN structure.

iv. Development of a method to quantify of the intensity of the blue colour change of the paper based sensor through digital image analysis using chromaticity.

v. Optimisation of the sensor to produce a linear response to glucose in simulated ISF extracted by the hollow MN

4.3 Results and Discussion

4.3.1 Manufacture of a hollow MN device for the extraction of simulated ISF

In order to produce a hollow MN, a Formlabs 1+ 3D printer was utilised to create the array. Initially, solid MN arrays were printed to investigate the ability of the printer to produce structures under one millimetre in length. Using computer aided drawing (CAD) software (SketchUp and Autodesk Nettfab) schematics of several solid MN arrays of various sizes were drawn and printed (**Figure 4.1**).
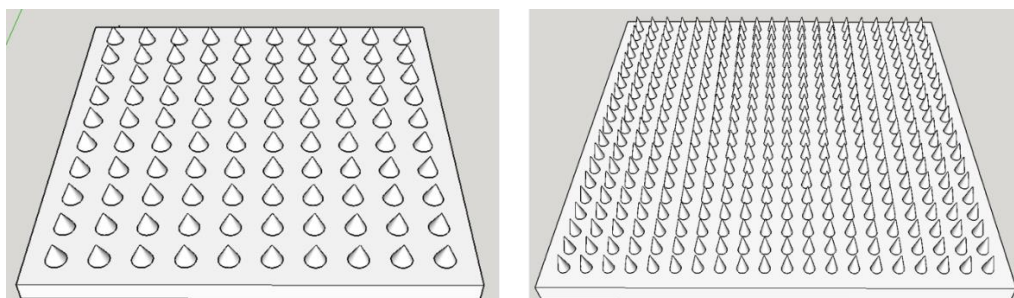
Array 1   Array 2

Figure 4.1 CAD images of solid MN arrays (Array 1) 1mm height, 1 mm base width, 1 mm interspacing and (Array 2) 1 mm height, 0.5mm base width, 0.5 mm interspacing

The printed arrays were examined using light microscopy to determine the dimensions of the projections and to evaluate the sharpness of MN tips (**Figure 4.2**). The projections of Array 1 had a mean height of 772.7 µm ± 90.9 µm and the projections on Array 2 had a mean height of 605.3 µm ± 42.9µm (n = 10). Both of the printed arrays showed a substantial difference in height from the original CAD schematics. Additionally, the tips of the projections were observed to be rounded or flattened.
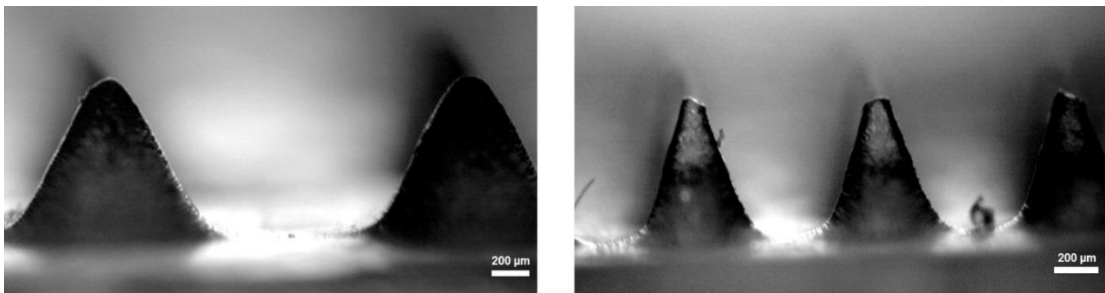
Figure 4.2 Optical microscope image of solid MN arrays projections produced using Formlabs 1+ 3D printer. Scale bars are 200 µm

Direct printing of a hollow MN would require extremely high resolution to produce the sharp tip and the hollow lumen of the MN successfully. Therefore, following examination of this data from printing solid MNs it was concluded that it would not be feasible to produce hollow MNs using the FormLabs 1+ 3D printer due to its insufficient resolution.

To overcome this challenge, instead of directly printing a hollow MN, a hypodermic needle was used as a moulding template. To produce a MN under 1000 µm in length, only the tip of the hypodermic needle was used as the template. To enable the replication of a set length of the needle, a housing for the needle was manufactured using the 3D printer as shown in **Figure 4.3**.
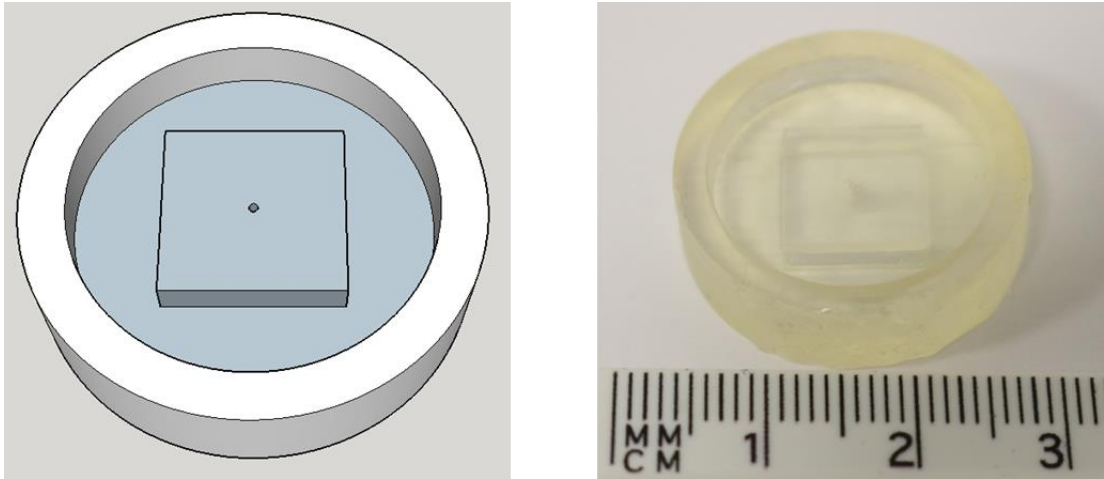
Figure 4.3 (Left) CAD schematic of housing to fix hypodermic needle. (Right) Housing to fix hypodermic needle printed using clear resin from Formlabs 1+ 3D printer

As the needle was inserted into the housing, the length of the exposed tip was controlled with a removable lid. The dimensions of the lid were designed in such a way that the length of the needle exposed after insertion was 400 µm (**Figure 4.4**).
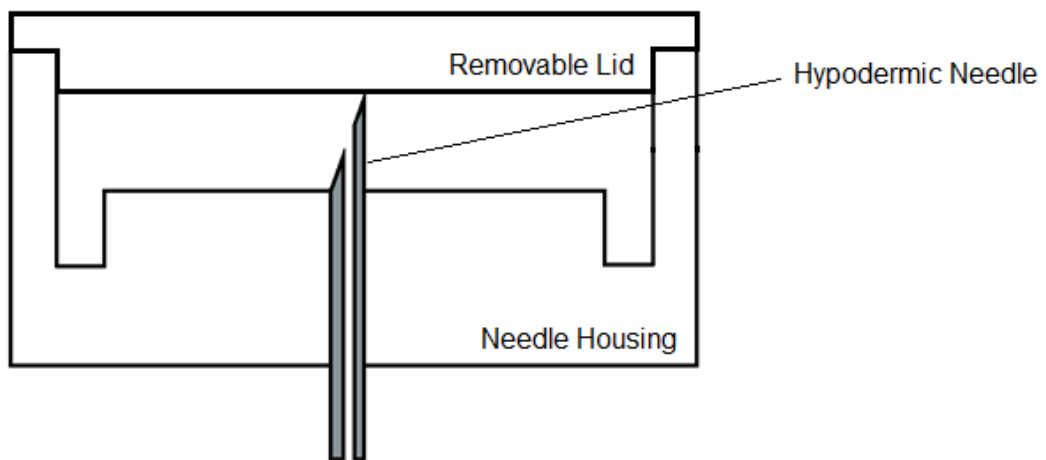
Figure 4.4 Schematic of housing with hypodermic needle inserted with attached lid. The length of the needle exposed is controlled by the gap between the housing and the lid (400 µm).

The templates were prepared as described in **Section 2.3.1.** The choice of polymers used to make the MNs was adapted from Lui et al.[151] and consisted of polymerised GMA crosslinked with TEGDMA and TRIM (**1**). Lui et al. investigated the use of these methacrylate based polymers in conjunction with a PEG porogen in order to make a porous MN that had interconnected pores capable of fluid extraction using capillary

action. However, in this work, the porogen was excluded in order to form a solid robust structure that was not porous, opting instead for a single hollow lumen through the MN projection.

Each MN was produced from the silicone templates as described in **Section 2.3.2**. Briefly, each mould was filled with 150 µL of **1** and a catalytic quantity of Irgacure 184 as a photoinitator before irradiation with UV light to enable polymerisation (**Figure 4.5**).

Figure 4.5 Schematic of hollow MN production. Silicone mould is filled with 150 µL of photopolymer mix before irradiation with UV light. Hollow polymer MN is then removed from mould.

To confirm each MN had remained hollow, a wire was threaded through the opening at the tip off each MN and through the baseplate. The MN projection was imaged using an optical stereomicroscope. This microscopy technique produced a stereoscopic view of the sample due to its binocular arrangement of lenses. It enabled the MN tip to be visualised without the need for more costly and less convenient electron microscopy. As seen in **Figure 4.6,** the MN produced had a sharp bevelled tip 400 µm in height, with the opening of the hollow bore clearly visible.

(a)   (b)
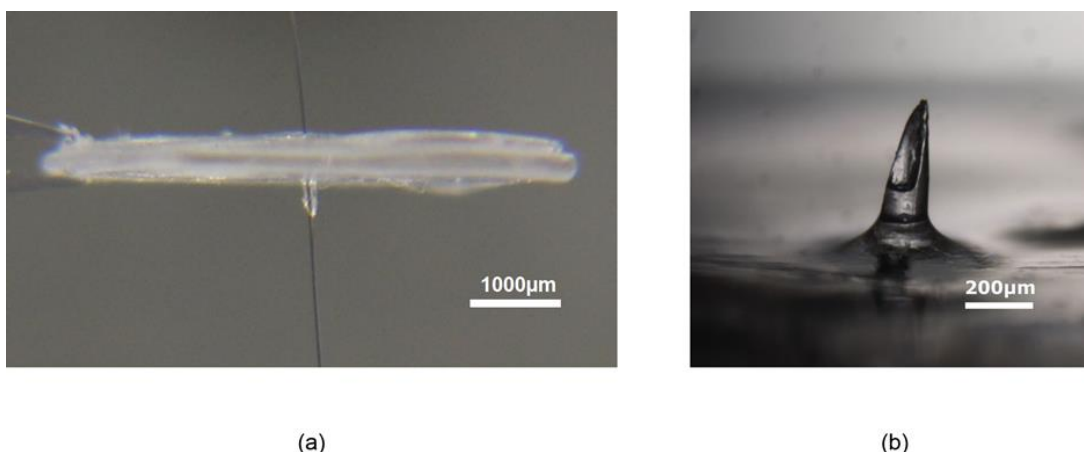
Figure 4.6 Photographs of polymerised hollow microneedle devices. (a) Polymer microneedle with metal wire through hollow bore. (b) Micrograph image of hollow microneedle tip.

4.3.2 Kinetics of fluid removal using the hollow MN device.

To confirm the capability of the hollow MN to withdraw fluid rapidly, a blank paper backplate was fixed to the upper side of the MN baseplate. The needle end of the device was then pierced through a Parafilm membrane and the assembly placed onto a solution containing MB dye (1 mM). The rate of MB uptake was followed visually over the course of 5 s. As observed in **Figure 4.7**, the first appearance of the dye occurred within 2 s and the backplate was completely saturated within 5 s.
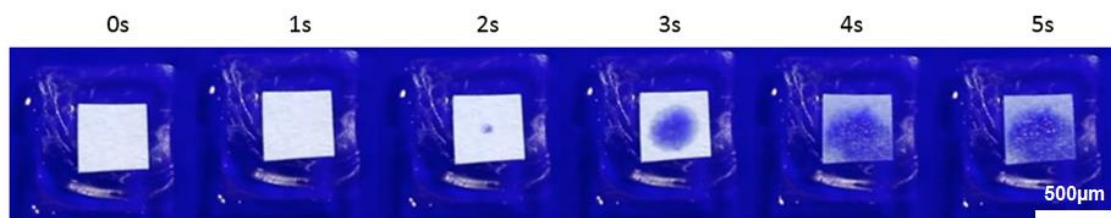
Figure 4.7 Digital photograph of single hollow MN device extracting MB solution (1 mM) into a blank paper backplate via capillary action over 5 s.

Notably, it was also observed that the blue solution moved up through the hollow bore and into the centre of the paper backplate from where it then migrated toward the outer edges. This confirmed that the fluid was only transported though the hollow bore of the needle and not through the baseplate itself. Such a timescale is compatible with use in a POC device.

4.3.3 Mechanical testing of the hollow MN device

To reliably penetrate the skin, the MN must be adequately robust to withstand the force necessary to penetrate without fracture. The mean axial force required to fracture the MN was measured to be 0.27 N ± 0.04 N (n = 4) by driving a steel rod onto the MN tip using an axial load test station (**Figure 4.8**). Previous reports have shown forces ranging between 0.028 N – 0.030 N per MN to be sufficient to penetrate the skin[152]. These values are approximately one order of magnitude lower than the mean fracture force of the hollow MN device. Therefore, the hollow MN should be sufficiently robust to withstand insertion into human skin.
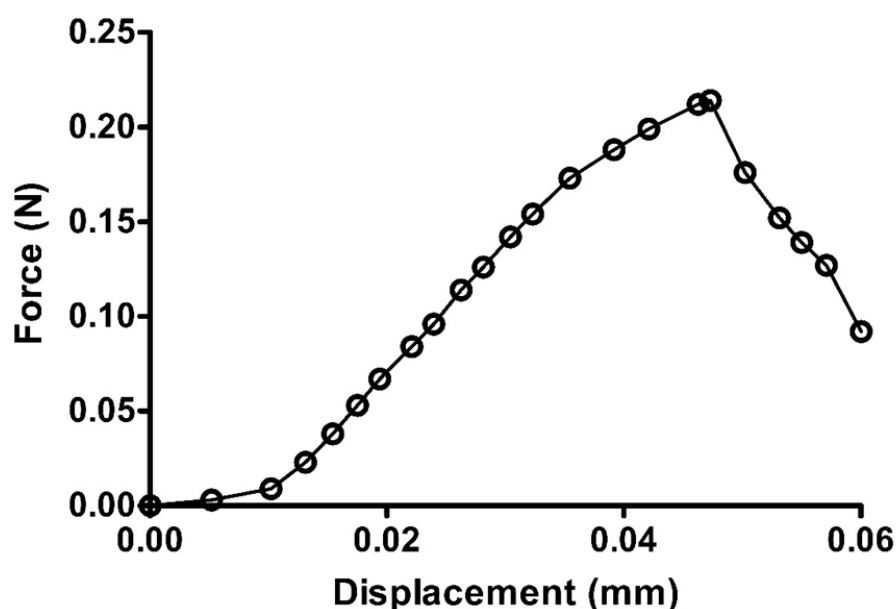
Figure 4.8 Representative graph of force against displacement of axial load fracture test of hollow MN. Mean force to fracture = 0.27 N ± 0.04 N (n = 4)

4.3.4 Development of a method to quantify of the intensity of the blue colour change of the paper based sensor

In order to more accurately develop the colorimetric sensor for glucose, a method to quantify the intensity of the colour change generated by the sensor was necessary. In **Chapter 3**, UV/Vis spectroscopy was used to quantify the concentration of the blue charge transfer complex in solution at 650 nm. However, this analytical method is more difficult when the sensor is incorporated into a solid matrix such as paper and requires the use of solid-sate probes in combination with a UV-Vis spectrometer. A

more convenient method to monitor the colour change in a paper matrix was to record photographs with a high resolution digital camera. Subsequently, the colour data could be extracted from the digital image using image processing software. Colours in digital images and screens can be represented using the trichromatic RGB model. The model is so named due to the three primary channels from which all other colours are derived: red, green and blue. The intensity of each of the channels range from 0 – 255 with 0 being the lowest to 255 being the highest intensity. **Table 4.1** shows how varying the intensity of each channel can change the final colour displayed. As the RGB model is additive, white is produced when all three channel are at maximum intensity (255, 255, 255) and black is produced when all channels are set to lowest intensity (0, 0, 0).

Table 4.1 Actual colour represented by Intensity of each colour channel ranging from 0 – 255 in trichromatic RGB model

R	G	B	Colour
255	0	0	
0	255	0	
0	0	255	
255	255	255	
0	0	0	

To quantify the intensity of a colour, the corresponding channel value can be monitored, however, the single value alone may not be directly proportional to the intensity observed. This is due to the luminance of the object in the image. To illustrate this concept, two photographs of a blue coloured paper were recorded, one in bright conditions and one in darker conditions (i.e. one image has high luminance and one has low luminance). Using image processing software, the value of the blue channel in the bright image (170) was determined to be greater than in the darker image (150), despite the colour of the object remaining unchanged (**Figure 4.9**).

| Darker Conditions | Brighter Conditions |
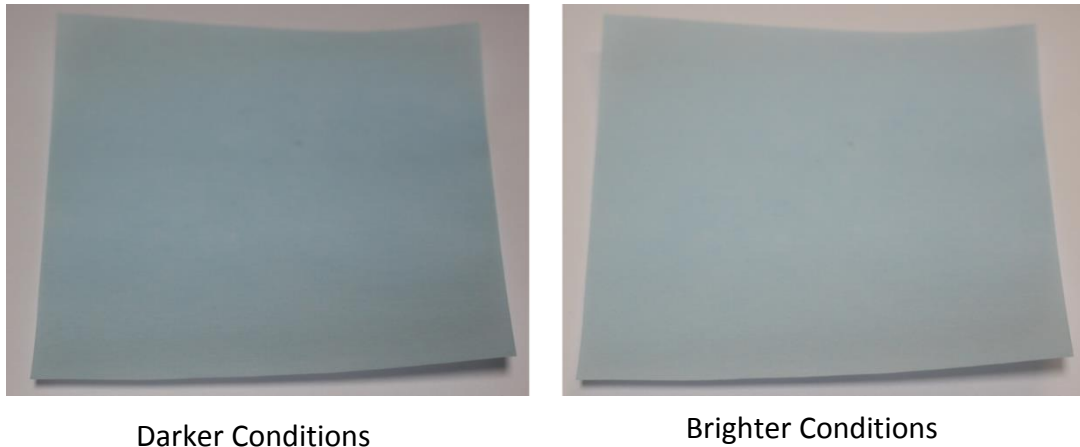
Figure 4.9 Digital photographs of blue coloured paper in dark conditions and light conditions

Therefore, it is unsuitable to use only a single colour channel intensity as a measure of colour intensity without taking into account the luminance. One approach to overcome this is to measure the chromaticity of the colour which can be calculated as described in Equation **4.1:**

$$Chrom_B = \frac{B}{R + G + B}$$
Equation **4.1**

Where $Chrom_B$ is the blue chromaticity, and R, G and B are the Red, Green and Blue channel values respectively.

The sum of the R, G and B channels represents the total luminance of the image which can be used to obtain the intensity of a colour independent of the total luminance. Taking the images from **Figure 4.10** and comparing the $Chrom_B$ value and the blue channel value it was found that the $Chrom_B$ was a more accurate method of determining the intensity of the blue colour in both images as the $Chrom_B$ values are much less affected by the luminance of the object (**Table 4.2**).

Table 4.2 Comparison of methods to obtain blue colour intensity from two images of the same object in different light conditions. Error represents % Standard Deviation and n = 4

Measurement Method	Dark Lighting	Bright Lighting
Blue Channel Value	150.6 ± 2.10%	170.4 ± 0.71%
$Chrom_B$	0.356 ± 0.25%	0.345 ± 0.15%

To validate the use of chromaticity in quantifying the blue colour intensity of paper backplates, an experiment was carried out in which paper squares (1 cm²) were submerged in increasing concentrations of MB dye (0 – 1 mM) and allowed to air dry. Digital photographs of each square were taken and the $Chrom_B$ values were calculated using ImageJ software. To control for any background interference, the $Chrom_B$ values of paper squares that had been submerged in distilled water were subtracted from the readings. **Figure 4.10** shows the linear relationship obtained between the $Chrom_B$ and the MB concentrations ($R^2 = 0.95$). From this experiment it was concluded that the $Chrom_B$ could be used to quantify the intensity of the blue colour of a paper based sensor in response to glucose.
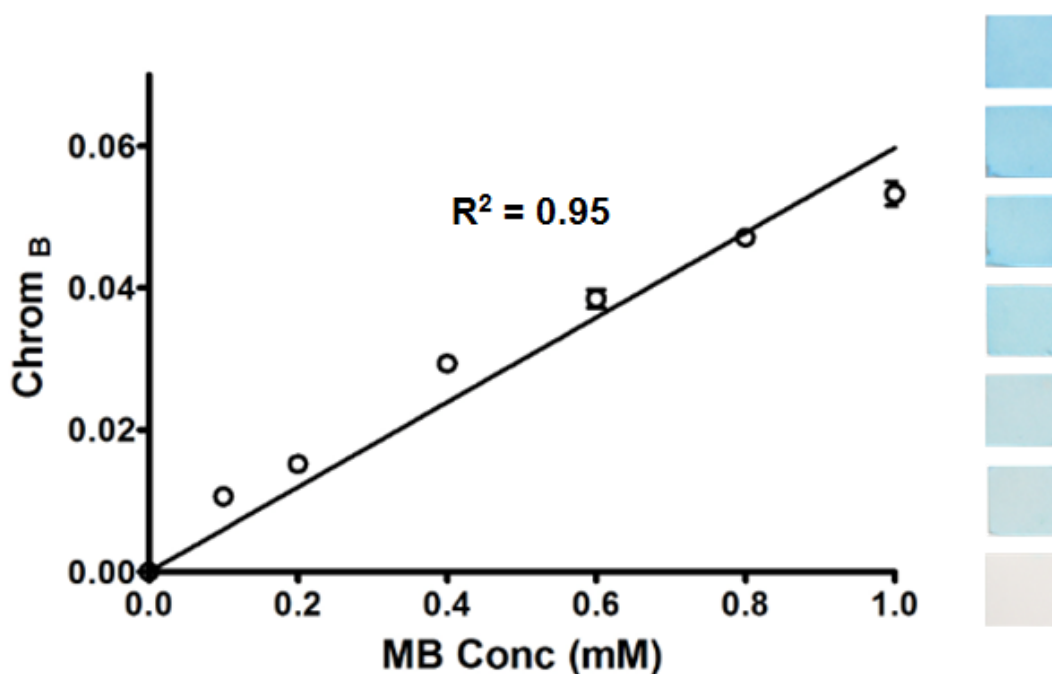
Figure 4.10 Linear relationship between $Chrom_B$ and MB concentration of paper squares after dye absorption and drying. Photographs of paper squares are shown to right of graph. Error bars represent standard deviation where n = 3

4.3.5 Optimising the sensing system to produce a linear response to glucose in simulated ISF.

In Chapter 3, the paper based glucose sensor was optimised to provide a rapid colour change in response to 10 mM glucose. In this section, the goal was to further optimise the sensor by establishing a linear colorimetric response to glucose concentrations between 0 – 10 mM in simulated ISF. Using the previous ratio of enzymes to TMB

(850 U/L GOx, 170 U/L HRP, 3.33mM TMB), paper backplates were prepared and the colorimetric response to glucose concentrations within a 0 – 10 mM range were tested (**Figure 4.11**). The Chrom$_B$ values of the backplates was used quantify the intensity of the colour change after 15 s.
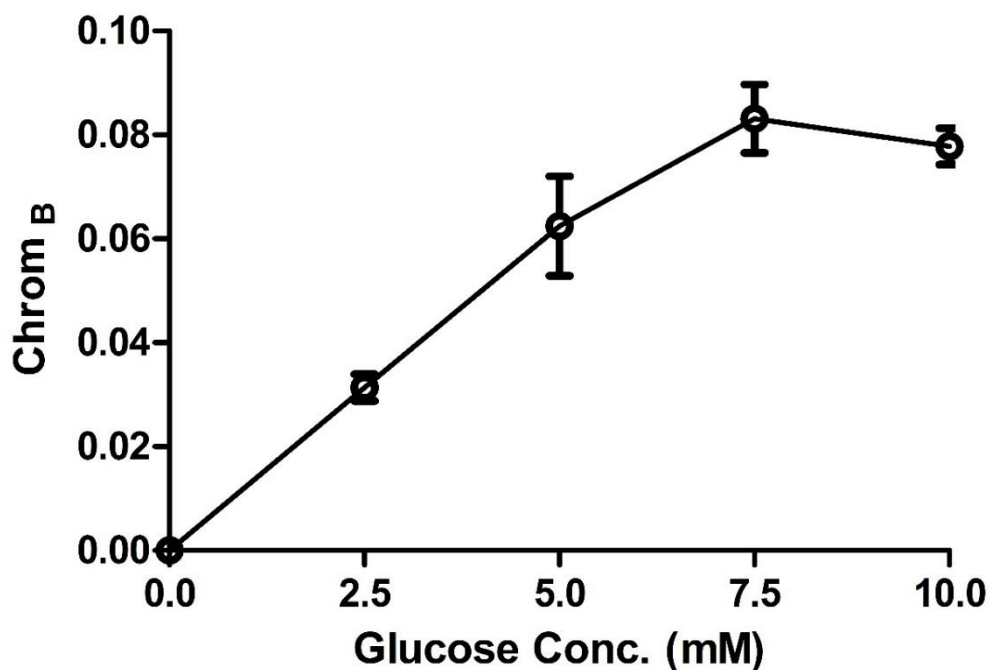
Figure 4.11 Plot of Chrom$_B$ of glucose sensor embedded paper backplate 15s after direct addition of glucose solutions of increasing concentration. Error represents standard deviation where n = 3.

The results from this experiment indicated that while there was a linear relationship between the glucose concentration and Chrom$_B$ between 0 mM – 7.5 mM, at the higher concentrations of glucose (from 7.5 mM – 10 mM), a non-linear relationship existed due to the further oxidation of the blue charge transfer complex to form the yellow coloured diimine, as demonstrated previously in the UV/Vis studies in **Section 3.3.3**. Therefore, in order to extend the linear response across a greater range of glucose concentrations, the concentration of the enzymes were decreased while the concentration of TMB was kept constant. Backplates were once again prepared but the concentration of GOx and HRP were decreased to 625 U/L and 125 U/L respectively. Several different concentrations of glucose (0 mM, 2.5 mM, 5.0 mM, 7.5 mM and 10 mM) were added to the backplates and digital photographs of each

recorded at 1 s intervals for a total of 15 s and the $Chrom_B$ values were calculated (**Figure 4.12**).
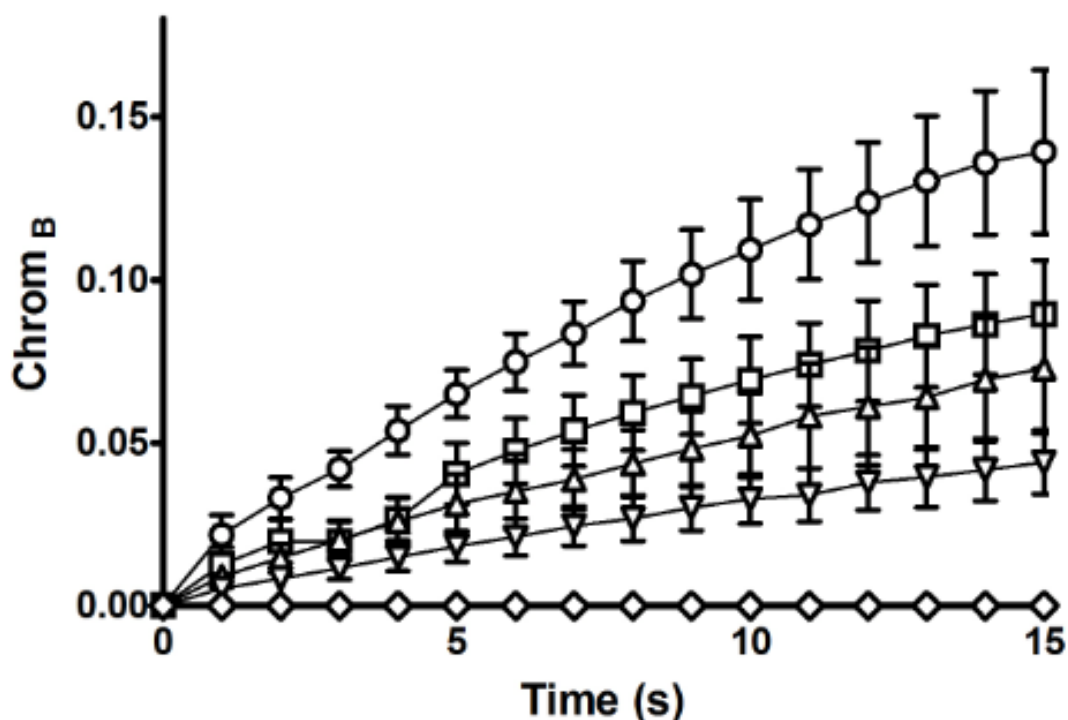
Figure 4.12 Plot of $Chrom_B$ against time for glucose responsive backplates following addition of increasing glucose concentrations. 10mM (Circle) 7.5mM (Square) 5mM (Triangle) 2.5mM (Inverted triangle) 0mM (Diamond). n = 3. Error bars are standard deviation.

The backplates rapidly began to change colour from white to blue as evidenced by the increase in the $Chrom_B$ values, with the greater concentrations of glucose causing more intense colour change over the course of the 15 s, while the control backplate with the addition of blank PBS remained colourless. When the $Chrom_B$ values at 15 s were plotted separately (**Figure 4.13**), a linear response was observed over the entire 0 - 10 mM range. ($R^2 = 0.95$). From the results of this experiment, backplates prepared using this concentration of enzyme and TMB were chosen to be paired with the hollow MN device to test the response to glucose after extraction using a similar *in vitro* experimental set up as in **Section 3.3.4**.
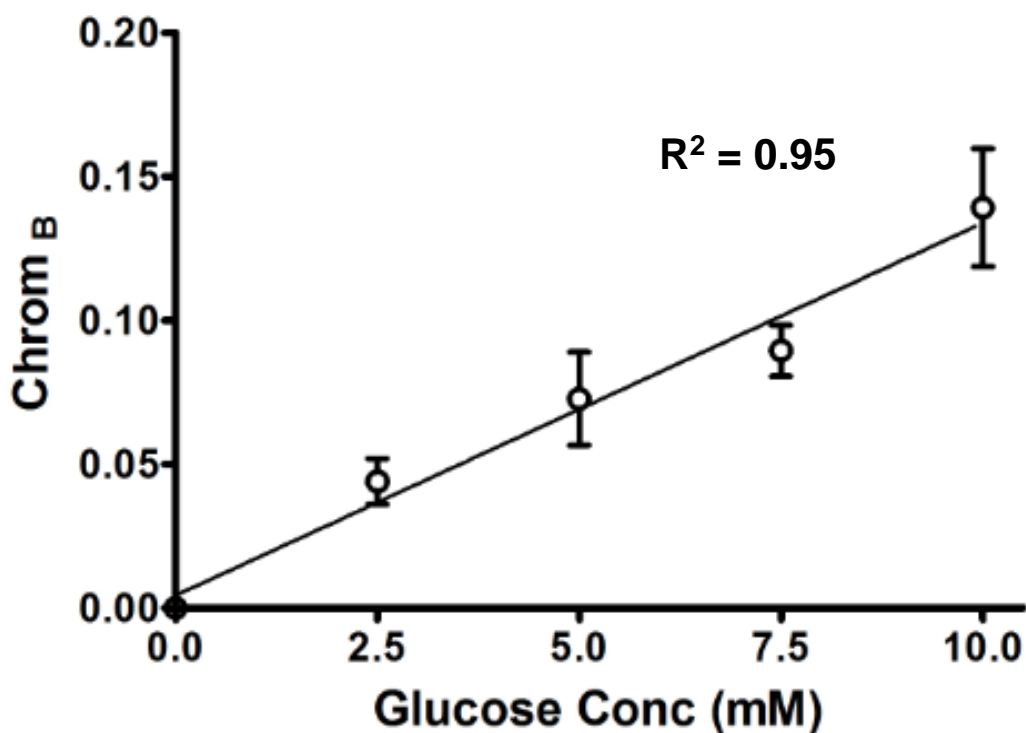
Figure 4.13 Linear relationship between Chrom$_B$ and glucose concentration after direction addition of 5 µL of glucose between 0 – 10 mM in PBS.

4.3.6 In vitro extraction of simulated ISF using MN device integrated with sensor backplate.

Having demonstrated the ability of the hollow MN to transport fluid rapidly to a paper back plate, and having developed a suitable sensing system with a linear colour change over the 0 - 10 mM range, the next step was to incorporate both together and test the ability of the resulting device to measure glucose concentrations in simulated ISF. Briefly, a paper backplate embedded with the sensor was fixed to the upper side of the baseplate. The MN-backplate assembly was then pierced through a single layer of Parafilm and placed on top of PBS solutions spiked with varying concentrations of glucose between 0 – 10 mM as a surrogate for ISF (**Figure 4.14**). Photographs of each backplate were taken after 15 s and 30 s and the intensity of the colour change was analysed as before using Chrom$_B$ measurements (**Figure 4.15**).
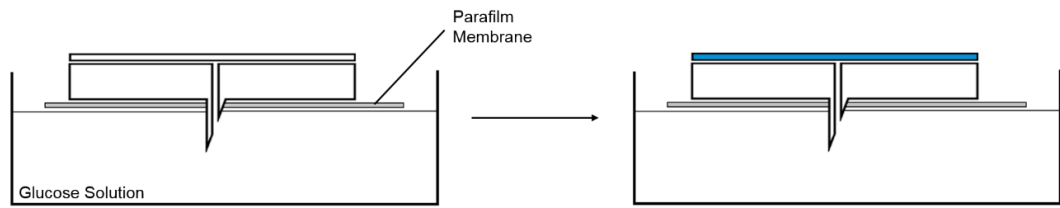
Figure 4.14 Schematic of the experimental set up of a glucose sensor embedded backplate attached to the single hollow MN device. The device was pierced through Parafilm to simulate the skin and place on top of PBS spiked with physiologically relevant concentrations of glucose (0 – 10 mM) as a surrogate for ISF
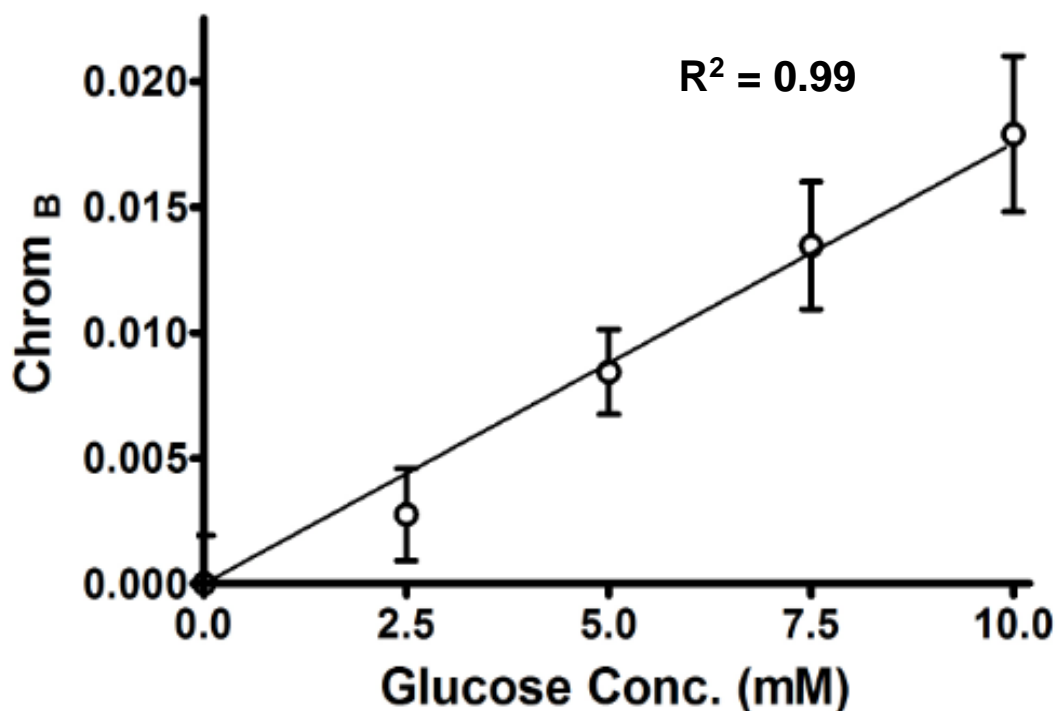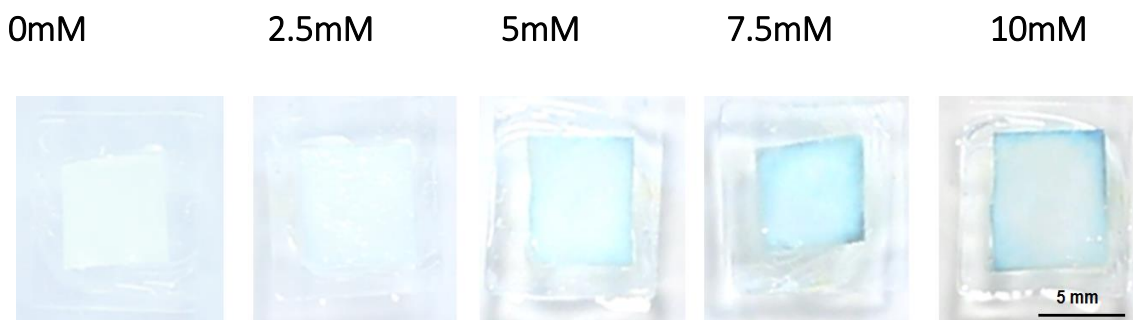
Figure 4.15 Digital photographs of sensor embedded backplates after 30 s showing blue colour change in increasing concentrations of glucose spiked PBS (above). Linear plot of Chrom$_B$ against glucose concentration. Error bars represent standard deviation where n= 3

As was the case for the MB study, the MN-backplate assembly again rapidly withdrew the glucose solution as evidenced by a dampening of the paper backplate. In addition, the intensity of the blue colour generated 30 s following immersion was dependent on the concentration of glucose with excellent linearity (R^2 = 0.99) observed over the 0 – 10 mM range. The relationship between the glucose concentration and the Chrom$_B$ showed superior linearity after 30 s than at 15 s. This change may be due to the change in the volume of the glucose solution that is absorbed into the backplate in the *in vitro* setup where it is controlled by the capillary action through the lumen of the MN compared to the experiment in **Section 4.3.4**

wherein a 5 µL aliquot of each glucose solution was added directly to the backplates. Representative images of the hollow MN-backplate assembly at each concentration demonstrated it was also possible to discriminate between the low and high glucose concentrations tested. Indeed, the difference in colour intensity produced from normal glycaemia (4 - 7 mM) and hyperglycaemia (>7 mM) was visually apparent.

Direct 3D printing of MNs has been previously attempted[153,154], however, one of the main limitations is the resolution of the printer, as observed in the work in this chapter. To overcome this issue, some groups have developed post printing processing steps such as chemical etching[155] in order to reduce the tip size of each MN projection. While this method has demonstrated the ability produce polylactide MN arrays capable of penetrating porcine skin, it did result in non-uniform MNs with uneven surface morphology in comparison to MN produced by conventional MEMS technology. The method deployed in this chapter of using a hypodermic needle as a master template has resulted in the production of a sharp tipped, bevelled edge MN with a more uniform surface than those fabricated with chemical etching following direct 3D printing.

Other efforts involving electrochemical detection of glucose within the ISF using enzyme coupled electrode systems have been previously published. Silicon dioxide MN arrays fabricated using photolithographic methods coupled to an enzyme linked biosensor has shown rapid uptake of ISF (1 µL/s) through capillary action *in vitro* and subsequent highly sensitive detection of glucose concentration across a range of 0 mM – 35.0 mM[156].

Similarly, swellable poly (ethylene glycol diacrylate) MNs fabricated using photolithography have been doped with enzymes to create wearable electrodes to allow the detection of glucose and lactic acid concentrations[157]. However both systems have yet to be successfully demonstrated using *in vivo* models.

4.4 Conclusion

In conclusion, the results obtained in this chapter illustrate a novel method to manufacture a single hollow MN integrated with a colorimetric detection method for glucose. The hollow MN was formed by creating a master template with a

hypodermic needle coupled with a 3D printed housing that allowed replication of the needle tip and the hollow bore. The negative silicone mould was then used to create a solid photopolymer based MN device with a sharp bevelled tip to aid skin penetration, which demonstrated extremely rapid fluid uptake through capillary action within 5 seconds. The single MN projection withstood a mean axial load of be 0.27 N ± 0.04 N before fracture, which is greater than the 0.028 N – 0.030 N per MN measured in other reports that is required for skin penetration.

A method to quantify the intensity of the blue colour change in the sensor backplate was developed by calculating the $Chrom_B$ values from digital images of the backplate after the addition of glucose. By altering the concentration of the components of the sensor system, a linear colour change after 30 s was achieved when the integrated MN device was used to extract physiologically relevant concentrations of glucose in simulated ISF *in vitro*. The colorimetric paper based backplate provided a rapid and facile method to detect glucose after 30 s that enabled discrimination between normal glycaemia (4 - 7 mM) and hyperglycaemia (>7 mM) with the naked eye.

This integrated device obviates the need for removal and further processing of the simulated ISF from the MN to obtain a glucose concentration and thus represents an important step towards the goal of an easy to use, minimally invasive, POC device as an alternative to fingertip blood sampling in diabetes. The calculation of the $Chrom_B$ was demonstrated to be an excellent method to quantify the intensity of the glucose dependent colour change. In the development of a colorimetric test strip for salivary glucose, Soni et. al[158] demonstrated that an office scanner can be used to quantify the intensity of the colour change. Placing the test strip in the office scanner would control the lighting conditions of the strip during the data procurement, however, as demonstrated in **Section 3.2.2**, calculation of $Chrom_B$ does control for changes in ambient light. Measurement of $Chrom_B$ value using digital photography removes the need for the paper sensor to be separates from the MN and placed in the scanner to be measured and, therefore, it is more convenient and compatible to a wider range of experimental set-ups and devices. One could easily envisage the digital camera used in this chapter being replaced with a mobile phone with on-board imaging software making it even more user friendly.

The next step in the development of this approach would be to produce 2D arrays of hollow MNs. Fabrication of a 2D MN array would increase the mechanical properties of the device and, therefore, decrease the risk of MN breakage while also increasing the number of channels for ISF to be extracted through capillary action. Finally, while the polymer mix selected to manufacture the MN device was previously used to produce MNs[151] and demonstrates excellent wettability properties, thus acts to extract fluid extremely rapidly through capillary action, the biocompatibility of the polymer mix would need to be investigated.

5.0 Glucose detection using a hollow metal microneedle interfaced with an optical glucose sensor: the use of antioxidants to modulate signal response.

5.1 Introduction

5.1.1 Hollow Metal MNs

Biocompatibility is one of the key requirements of a transdermal device as they are designed to be in contact with both the skin surface and the upper layers of the epidermis. With the widespread use of silicon in MN manufacture using microelectromechanical systems (MEMS) technology, the biocompatibility of the silicon used has generated much interest. There is a risk of MN fracture upon insertion resulting in residual silicon remaining in the skin after use due to its brittle nature[159]. The presence of granulomas have been observed in response to the presence of silicon in the skin which is a sign of immune response and inflammation[160]. With the large range of immune cells present in the epidermis, the resultant release of cytokines and pro-inflammatory markers upon insertion of foreign bodies can elicit an immune response thus decreasing the biocompatibility of the material[161].

Metals such as stainless steel and titanium are commonly used in medical devices due to their mechanical properties and biocompatibility. Titanium has been used in prosthetics and implants[162] whereas hypodermic needles are commonly manufactured from stainless steel. The use of stainless steel to make MNs has the advantage of both the mechanical robustness of the metal thus decreasing the risk of MN fracture upon insertion into the skin and the well-established biocompatibility of the material. Unlike hydrogel MNs which become unable to penetrate skin after a single use, metal MNs do carry the risk of accidental needle stick injury and as such may increase the risk of transmitting infection between users. However, due to the decreased length of the needle this risk may be quite low compared to full sized hypodermic needles as the shorter MNs are not capable of reaching the blood

capillary system in the skin and so are unlikely to directly carry blood borne pathogens from one person to another. Additionally, the risk of infection from microbes on the skin has been shown to be lower through the use of MNs compared to conventional hypodermic needles[163,164].

5.1.2 Modulation of the colorimetric glucose sensor for the detection of hyperglycaemia.

In the previous chapter, a glucose responsive backplate was developed that produced a linear colour change to glucose concentration within 0 – 10 mM. While the intensity of colour change enabled differentiation between low physiological glucose concentrations (< 5mM) and high physiological concentrations (> 7.5 mM) using the naked eye, some ambiguity remains in distinguishing between different grades of colour intensity. A simpler approach would be an "Off-On" detection system that only produces a colour change when a certain level of glucose is exceeded. Thus the sensor would remain colourless in normal glucose concentrations and give a colour change when the concentrations of glucose indicate hyperglycaemia (> 7.5 mM).

From the work undertaken in **Chapter 3** (see **Section 3.3.3**), it was observed that reducing the concentration of the GOx/HRP enzyme mix while maintaining the TMB concentration in the sensing system, reduced the rate of TMB oxidation when glucose was added. While further reductions of GOx/HRP could potentially result in the desired "Off-On" response to hyperglycaemia, the reduced enzyme concentration would reduce significantly the kinetics of the colour change reaction for it to be of practical use. Therefore, to achieve an "Off-On" colour change in response to hyperglycaemia within in a practically useful time, an alternative approach was necessary.

Interference with GOx based colorimetric tests for glucose has been reported with strongly reducing substances including ascorbic acid (AA), beta-lactam antibiotics, levodopa, and salicylates giving false negative results[165]. AA has shown inhibitory effects in colorimetric assays for uric acid, cholesterol and glucose involving hydrogen peroxide mediated changes in colour intensity[166]. This is due to the high affinity of

AA for peroxidase enzymes causing depletion of the H_2O_2 produced as shown in **Scheme 5.1**.
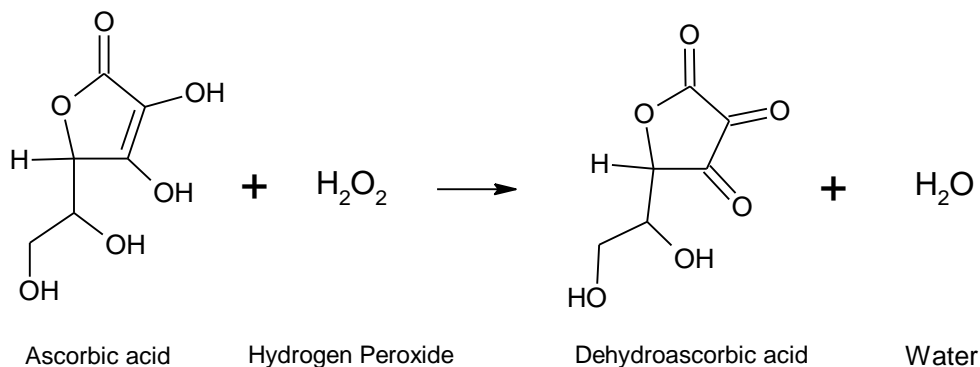
Scheme 5.1: Peroxidase catalysed oxidation of ascorbic acid to dehydroascorbic acid by hydrogen peroxide

Clinistix reagent strips are a commonly used paper based colorimetric test for urine glucose that is based on the oxidation of o-tolidine in a GOx/HRP enzyme system. AA has been shown to cause a delay in the formation of the coloured compound that was proportional to the concentration of the AA (**Table 5.1**). Additionally, at increasing concentrations of glucose the resultant lag phase was decreased[167].

Table 5.1: Inhibition of colour change in Clinistix glucose test strips in the presence of AA [167]

	Time lag (s) at glucose concentration of :		
Ascorbate (mg/L)	2.5 g/L	5 g/L	7.5 g/L
100	2	-	-
250	4	3	3
500	7	5	4
1000	22	9	7

Similarly, using a 4-aminophenazone based dye which combines with phenol to form a quinoneimine in the presence of H_2O_2 (**Figure 5.1**), a delay in colour formation is observed when AA was added to the dye system[155].
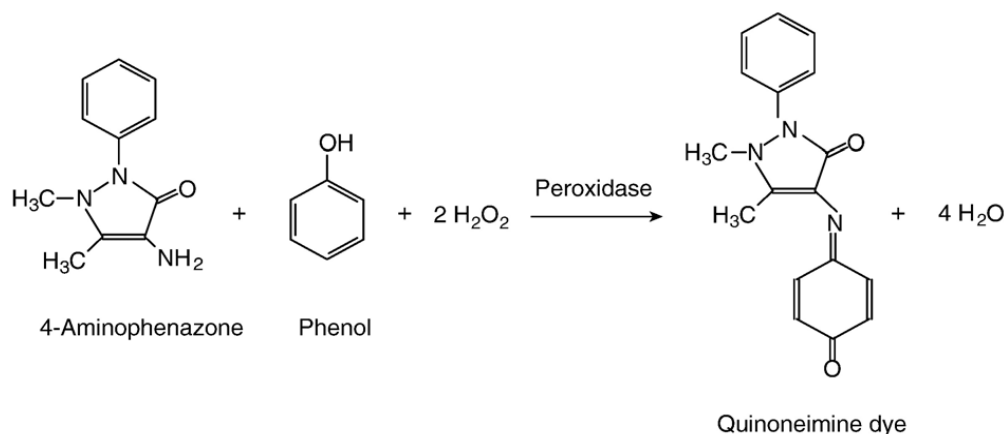
Figure 5.1 Trinder reaction, a H_2O_2 dependent formation of coloured quinoneimine dye used to determine glucose concentration[1]

As both the ascorbic acid and dye compete for the available peroxide, oxidation of the dye and concomitant colour change is inhibited or delayed. Thus, when monitoring the development of the coloured chromophore, a time delay form the start of the reaction is observed in which no visible coloured compound is generated. This delay or lag phase has been found to be proportional to the concentration of the ascorbic acid concentration and inversely proportional to the concentration of glucose[1].

This lag phase may be exploited in order create a sensor to produce a colour change within a predetermined time period only if the concentration of glucose was high enough, thus indicating hyperglycaemia. In lower glucose concentrations, the lag phase would be increased and, therefore, no colour change would occur within the predetermined time period.

5.1.3 Vacuum assisted suction through MNs

MNs coupled with vacuum force have been used previously to extract ISF from the skin. However, they have largely involved piercing the *stratum corneum* with solid MN arrays followed by the application of a separate vacuum device to draw fluid through the micropores created after the MN array was removed[168]. In this chapter, a flexible housing for the hollow MN device was designed in order to aid the extraction of fluid. The integrated housing generated a small negative pressure created by the press and release of the housing to draw fluid through the MN and into the sensor backplate.

5.2 Aim and Specific Objectives

The main aim of the work undertaken in this chapter was to manufacture a hollow MN device with the MN projection composed of stainless steel coupled with a paper based sensor that underwent a colour change only in high concentrations of glucose that indicated hyperglycaemia. The specific objectives were:

i.   Manufacture of a hollow metal MN device that can extract fluid rapidly and transport it into an attached backplate.

ii.   Development of a colorimetric sensor based on GOx/HRP, TMB and ascorbic acid to indicate hyperglycaemic concentrations.

iii.   Investigate the benefit of incorporating vacuum assisted suction within the MN housing to facilitate rapid solution withdrawal.

iv.   Integration of the paper based sensor backplate with the hollow MN device and subsequent *in vitro* testing to investigate its ability to rapidly indicate hyperglycaemic concentrations in simulated ISF.

5.3 Results and Discussion

5.3.1 Manufacture of Hollow Metal MN device

BD Micro-fine Ultra 32G needles were used to create the metal hollow MN device. The commercially available needles possessed a bevelled edge on each end. However, each side was not identical as demonstrated by the optical microscope image below (**Figure 5.2**). The end designed to pierce the skin to a depth of 4 mm possessed a bevel 1100 μm ± 12 μm in length. Therefore, it was not possible to use the full length of this end in the MN as the final projection would extend longer than 1000 μm. The opposite end of the 32G needles had a bevelled end 417 μm ± 5 μm in
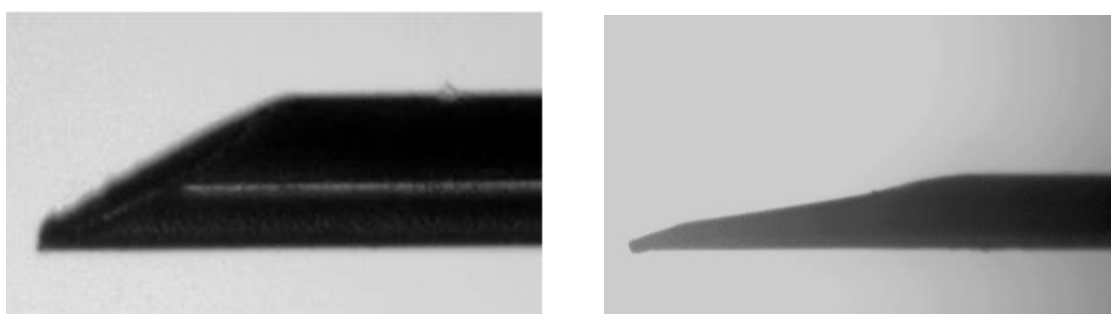
Figure 5.2 Light microscope image showing both ends of a BD Micro-fine Ultra 32G needle. Scale bar is 200 μm in both images

length. This enabled inclusion of the total length of this bevelled end and an additional portion of the needle shank to yield a final MN projection within the 1000 μm limit.

Initially, attempts were made to cut the needles to the desired length (i.e. 2 mm) using pliers but this resulted in the end of the needles being closed due to the compression from the pliers. To circumvent this issue, the needles were cut to approximately 4 mm in length and then inserted in a custom made holder (**Figure 5.3**).
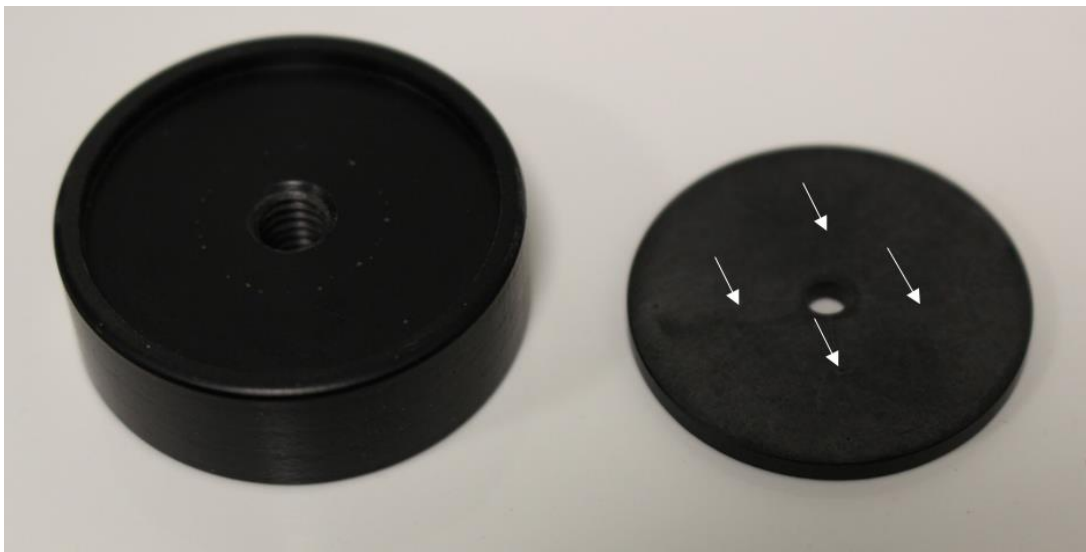
Figure 5.3 Custom holder used to reduce needles to correct length while remaining open. (Left) Baseplate into which top plate is placed. (Right) 2 mm deep upper plate with 4 circular holes (white arrows) 200 μm in diameter into which the needles are placed point downwards.

The holder consisted of a baseplate with an upper plate 2 mm in depth attached together with screws. In the upper plate, holes were drilled using a drill bit which was 100 μm in diameter. The 4 mm long needles were inserted into these holes with the needle point downwards and the excess material was filed away using abrasive wet-or-dry sand paper (**Figure 5.4**).
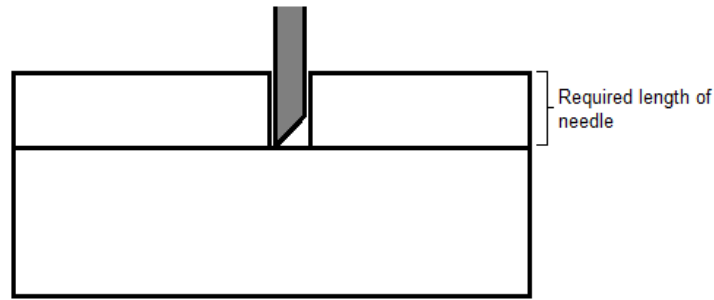
Figure 5.4 Schematic diagram of needle placed point downwards into 200 μm diameter holes in needle holder. Needle is reduced in length by circular sanding until level with the surface of upper plate which yielded 2 mm long needles

Initially grade P600 paper was used to remove the majority of the excess length of the needle then grade P1000 paper was used to remove the final ~0.5mm in order to remove small burrs in the metal walls of the needle and ensure the plastic holder was not substantially abraded. After removal from the holder the needles were washed in acetone to remove metal debris and a length of stainless steel wire (100 μm diameter) was inserted through each needle to ensure complete opening. **Figure 5.5** shows how the needle end that was closed after cutting with the diagonal cutting pliers was reopened using the sanding method.
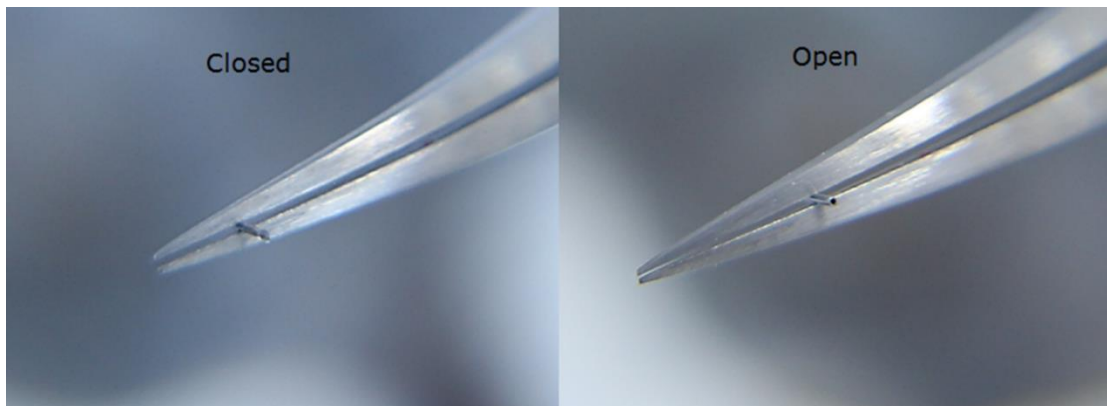
Figure 5.5 (Left) Photograph of needle cut with diagonal pliers showing how the end of the needle is crimped closed. (Right) Photograph of needle after sanding showing the reopening of the needle

A baseplate in which to house the 2 mm needle was created using a silicone moulding technique. As described in detail in **Section 2.4.2**, a master mould was designed in CAD and created using the Form 1+ 3D printer in the proprietary clear methacrylate based photopolymer. The master mould was used to make a negative mould using RTV silicone. The 2 mm hollow needle was placed in the centre of the negative mould and the MN baseplate, composed of TRIM, was polymerised around its base, leaving the needle tip exposed. An aliquot of 200 μL of TRIM was pipetted into the silicone mould before irradiation with 365 nm UV lamp for 60 mins (**Scheme 5.2**).
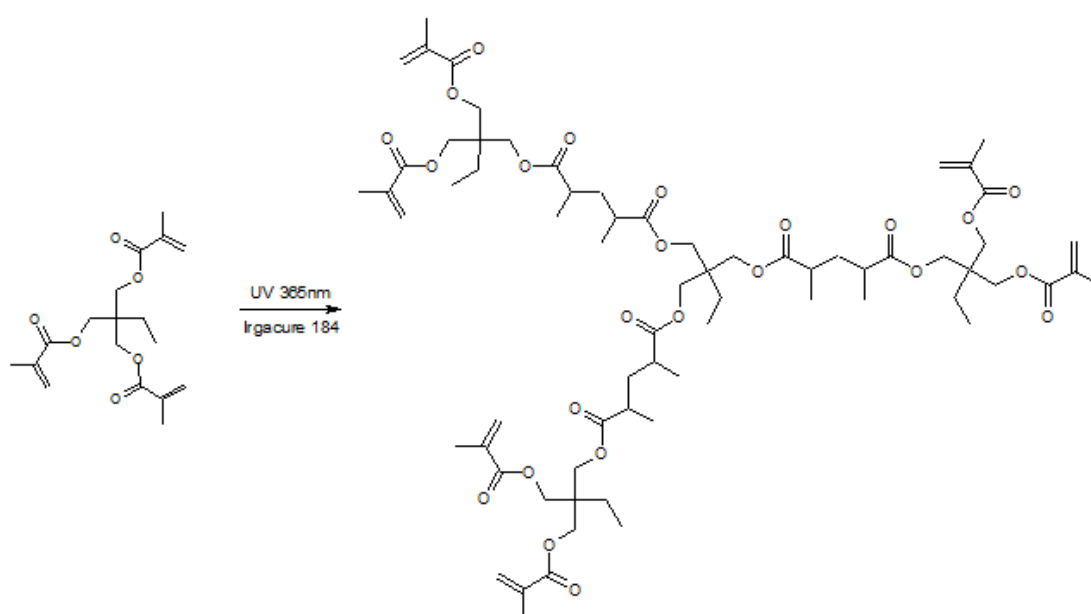
Scheme 5.2 Photo-catalysed polymerisation of TRIM by free radical generator 1-Hydroxycyclohexyl phenyl ketone (Irgacure 184) and UV irradiation (365nm)

After polymerisation, the MN with attached baseplate was removed from the mould, washed in ethanol and dried at 60 °C for 10 min. A representative photograph of the prepared MN is shown in **Figure 5.6a** and clearly reveals the crosslinked TRIM polymer baseplate with a single MN projection emerging. The bevel end of the needle was clearly hollow and emerged through the base plate to the other end. In addition, **Figure 5.6b** also clearly demonstrates the photopolymer coats the needle shank maintaining it in place and providing mechanical strength. In total, 10 MN were produced using this method with a mean MN projection of 590 μm ± 23 μm.
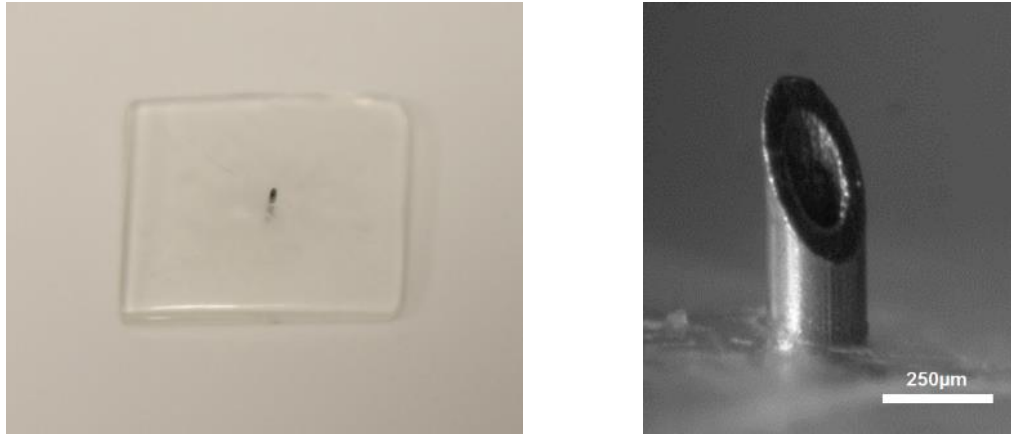
Figure 5.6 (a) Photograph of metal hollow MN in polymer baseplate. (b) stereomicroscope image of MN. Scale bar is 250 μm

5.3.2 Flexible PDMS suction housing to aid fluid extraction

In **Chapter 4**, the MN device prepared relied solely on capillary action to draw fluid through the MN opening and into the backplate. While the liquid extraction kinetics using this method was rapid, this was determined in solution and does not accurately represent tissue where the volume of ISF is not as large or readily accessible. To overcome any possible reduction in fluid withdrawal rate as a consequence of these issues, a modified housing for the MN device was also developed. The housing was prepared from PDMS in order to provide a suction force to draw fluid though the metal MN. The attachment was designed to be flexible enough to be slightly deformed when pressed with the fingertip as the MN was being applied. In this way, when the finger was released, the PDMS attachment would revert to its original shape and create a suction force through the metal MN, thus drawing fluid into the backplate. To create this attachment, a master mould was created using CAD and printed using the Form 1+ in clear resin as before (**Figure 5.7**). The mould was designed to allow the replication of an optically clear PDMS housing for the hollow MN device. The resultant square shaped housing with each side 15 mm² in length, with a depth of 6 mm and possessed a square opening for the MN device itself with each side measuring 10 mm² long.
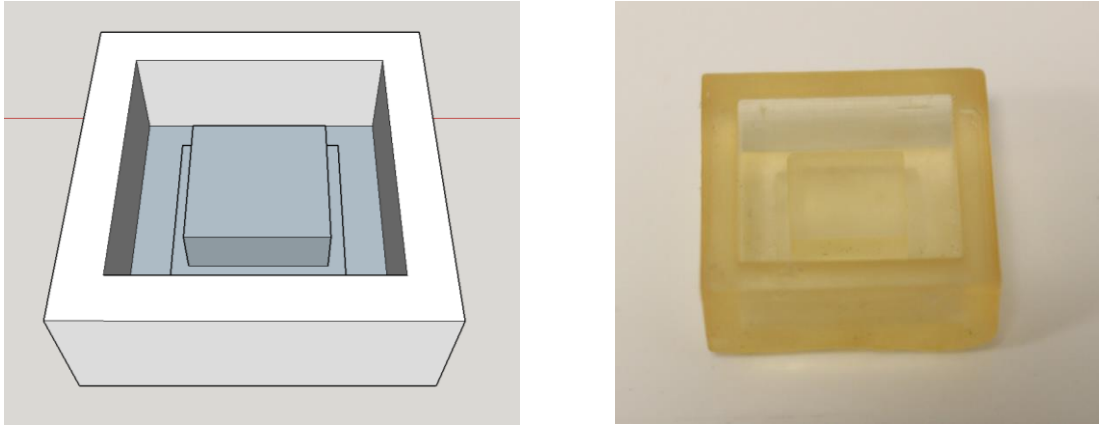
Figure 5.7 (Left) CAD image of master mould for PDMS suction device (Right) Photograph of mould for PDMS housing created using 3D printer.

In order to create a sufficient seal with the baseplate of the metal MN, the PDMS housing was designed with a segment of material that protruded from the length of the inner edge, as indicated in **Figure 5.8**. This design element was found to be an effective method to hold the square baseplate in place while it was fixed with adhesive. The assembled device with a blank paper backplate is shown in **Figure 5.8.**
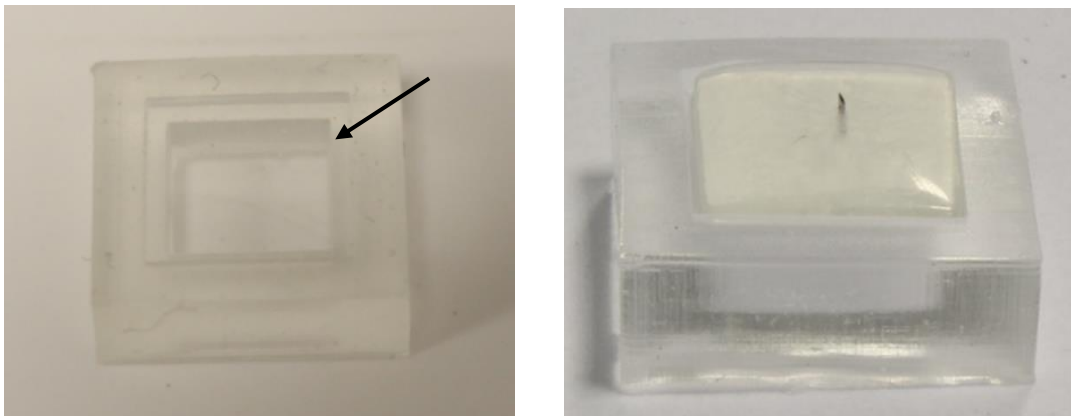
Figure 5.8 (Left) PDMS housing created from master mould. Arrow depicting inner edge used to hold polymer baseplate in place. (Right) Photograph of assembled device consisting of hollow metal MN in the polymer baseplate adhered to the PDMS attachment

Figure 5.9 shows the steps involved in the operation of the assembled MN device. The MN will be applied in order to pierce the metal hollow MN through the membrane to gain access to the glucose solution. Depression and subsequent release of the flexible PDMS housing by gentle finger pressure creates a negative pressure within the MN device that will aid fluid extraction through the hollow MN and into the sensor backplate for analysis.
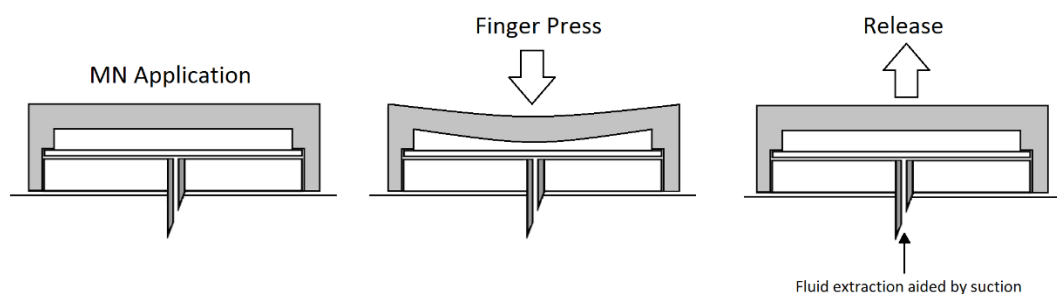
Figure 5.9 Schematic of the operation of the PDMS housing and single hollow MN device

In order to test the capability of the metal MN device with the PDMS attachment to withdraw fluid through suction, 30 mL of a 1 mM methylene blue dye was added to a petri dish. Two glass slides were placed lengthways across the top of the dish and separated by a gap of 5 mm to act as a solid support. The assembled metal MN device, shown in **Figure 5.8,** was then pierced through a layer of parafilm and placed on the petri dish in such a way so as the MN was in contact with the methylene blue dye between the glass slides (**Figure 5.10**). The flexible PDMS attachment was then depressed with thumb pressure and released. It was observed that a small volume of methylene blue dye was drawn up through the MN and into the backplate reservoir containing a blank paper square confirming the feasibility of the device.
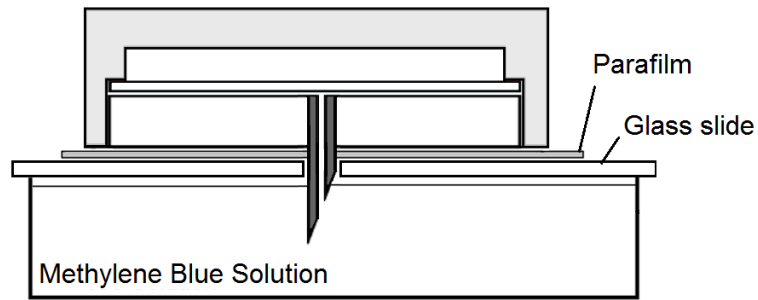
Figure 5.10 Schematic of experimental set up to investigate the capability of the MN device to draw Methylene blue solution from the container through the MN and into the paper backplate. The glass slides were in place to provide a solid support to allow the flexible PDMS attachment to be pressed and released.

As demonstrated in **Figure 5.11**, photographs taken 5 s following release of thumb pressure reveal successful extraction of a small volume of MB solution that had been absorbed rapidly by the paper backplate. This demonstrated that the suction pressure generated from the press and release of the PDMS housing was sufficient to cause the movement of the MB solution from the MN tip, through the hollow MN and into the paper backplate, contained within the assembled device.
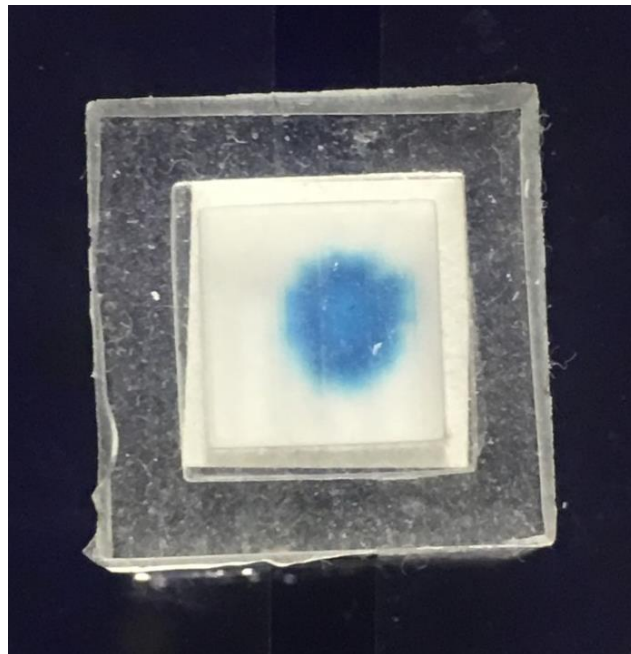
Figure 5.11: Photograph of assembled hollow MN device 5 s after press and release showing extraction of MB solution into black paper backplate

It was noted that although the blue colour could be observed through the PDMS attachment, the PDMS material was not completely optically clear. This was due to the uneven surface of the mould that is inherent to the 3D printing technology and the polymer material used to create the mould. This resulted in the PDMS having a slightly uneven inner surface which led to the light becoming diffuse as it passed through, resulting in a blurred image. To overcome this, the mould was modified slightly by placing a glass microscope coverslip to the uneven mould surface in the visualising region of the backplate. (**Figure 5.12**).
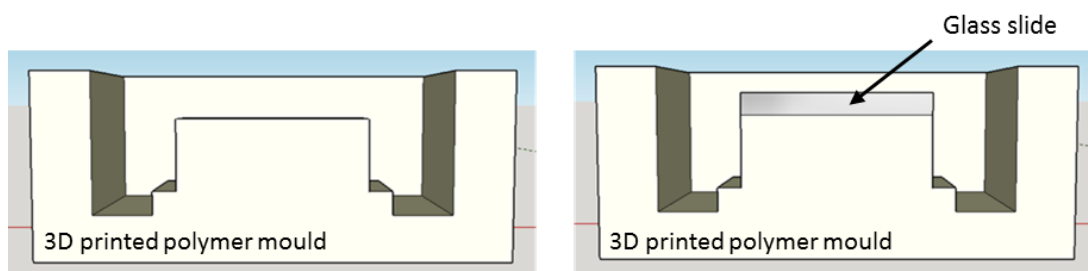
Figure 5.12 Cross sectional CAD images of mould used to create PDMS attachment. (Left) Original mould. (Right) Mould with added glass slide layer.

The glass slide provided a smooth surface for the curing of the PDMS and resulted in much more optically clear polymer window through which the colour of the paper could be observed. To demonstrate this, paper squares were spotted with a small volume ($\sim$2 µL) of methylene blue solution and photographed when placed in the non-modified PDMS housing or the modified glass slide PDMS housing. A photograph of the same paper square without the presence of a PDMS housing was taken for comparison (**Figure 5.13**).

<center>(a)   (b)   (c)</center>
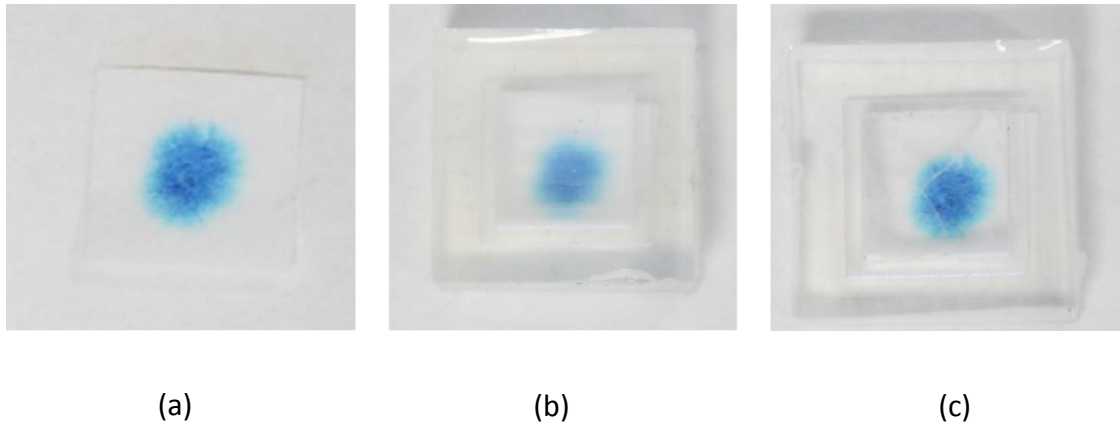
Figure 5.13 Representative photographs of the same paper backplate with methylene blue dye stain as seen through different PDMS attachments. (a) No PDMS housing. (b) Non-modified PDMS housing. (c) PDMS housing with glass slide modification.

While this modification to the mould created a more transparent PDMS housing through which to see the colour of the paper backplate than the original PDMS housing, the photographs were also analysed using ImageJ and the blue chromaticity of the methylene blue dye spots were calculated for comparison (**Figure 5.14**).
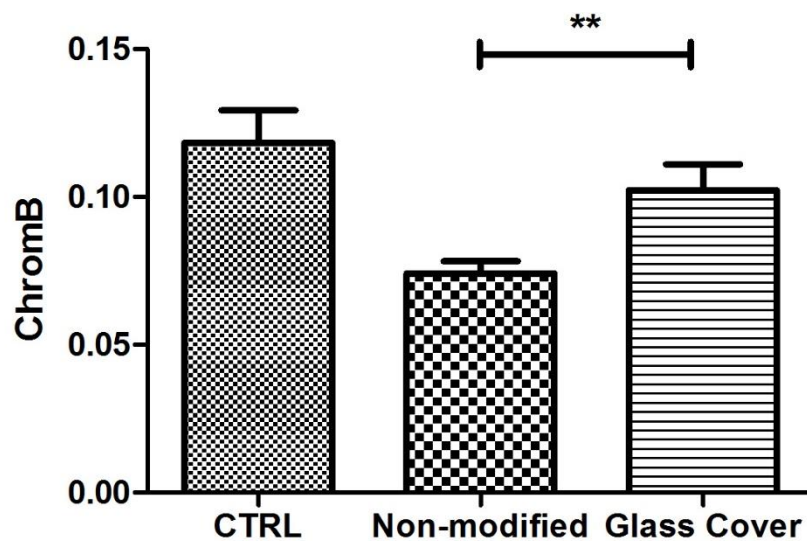
Figure 5.14 Plot of $Chrom_B$ of paper backplate with methylene blue as seen through original non-modified PDMS housing and PDMS housing created with glass cover modified mould. Control is paper backplate imaged with no PDMS housing. ** $p < 0.01$. (n = 3)

The mean $Chrom_B$ value of the paper backplate with no PDMS housing was 0.118 ± 0.011. When photographed through the modified PDMS housing the $Chrom_B$ value was 0.102 ± 0.008 which is comparable to the control and was significantly greater

than the non-modified PDMS housing (0.074 ± 0.004, p < 0.01). These representative photographs and quantification of the $Chrom_B$ values demonstrate the benefit of the modified PDMS housing compared to the original housing with a clearer observation of the colour change to the end user of the device.

5.3.3 Optimising the GOx/HRP, TMB based colorimetric sensor using ascorbic acid to modulate the glucose mediated colour change

L-Ascorbic acid (AA) is oxidised by H_2O_2 to dehydro-L-ascorbic acid through a reversible two electron mechanism with a free radical intermediate (**Scheme 5.1**). Further oxidation into diketogulonic acid and tetrahydroxydiketohexanoic acid has also been reported[169].

To investigate the effect of AA on the H_2O_2 producing glucose sensor developed in the previous chapters, photophysical studies using the glucose sensor system with AA added were undertaken. Subsequent changes in the TMB intensity at 650 nm was determined by UV/Vis spectroscopy. Solutions containing GOx, HRP and TMB were prepared using the optimised ratios for a rapid linear glucose mediated colour change (625 U/L GOx, 125 U/L HRP and 3.33 mM TMB) as determined in **Section 4.3.4**. These solutions also contained either (0 µM, 20 µM or 40 µM) AA which were the initial concentrations chosen to observe the effect on the generation of the coloured TMB compound. 5 µL aliquots of 7.5 mM and 10 mM glucose were then added to each solution and the absorbance at 650 nm measured every 10 s for 5 min. A plot of absorbance intensity at 650nm as a function of time was plotted for each of the three experiments and is shown in **Figure 5.15**. In the solution containing no AA (**Figure 5.15a**), the oxidation of the TMB proceeded immediately after the glucose was added, with the 10 mM glucose experiment showing a higher rate of oxidation than the 7.5 mM glucose experiment, consistent with the results obtained in **Section 4.3.4**. When 20 µM AA was added to the sensor system, the kinetics of the reaction changed significantly (**Figure 5.15b**), with an initial period where the TMB was not oxidised, as demonstrated by no substantial change in the absorbance from the baseline in the initial 10 s. This delay in intensity increase lasted longer (50s) for the 7.5 mM glucose experiment than for the 10 mM glucose experiment (20s), consistent

with the hypothesis that more glucose generates more peroxide that oxidises AA in preference to TMB.

The results in **Figure 5.15c** show that the effects of the AA on the kinetics of the reaction were more pronounced as the concentration was increased. The 10 mM glucose solution started to increase from the baseline at 30 s and the 7.5 mM glucose solution increased at 90 s. This demonstrated that the lag phase could be increased by including more AA within the sensor system.

The results of these experiments demonstrated that AA could be used to modify the glucose sensor to give a blue colour change only in hyperglycaemic conditions within a given time period, for example within 60 s. A time constraint had to be specified as the inclusion of AA did not stop the colour change reaction from occurring in normal glucose concentrations, however, it did introduce a substantial lag phase before a colour change occurred between a 10 mM glucose sample (hyperglycaemia) and 7.5 mM (normal glucose).

.

(a)

(b)

(c)
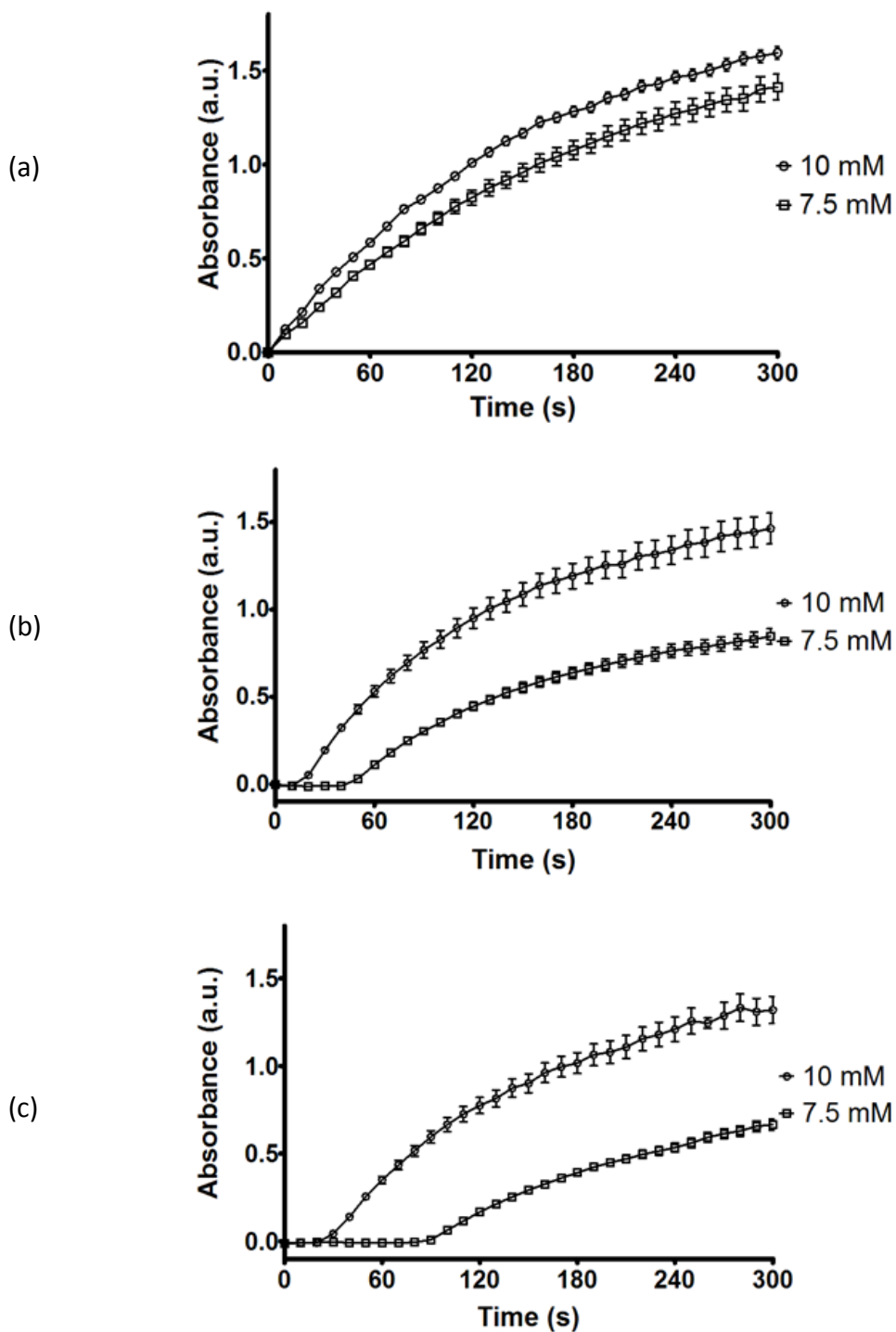
Figure 5.15 UV/Vis spectra of oxidation of TMB by GOx/HRP in solutions containing several concentrations of AA. Absorbance was measured at 650 nm at 10 s intervals. Circles represent solutions spiked with 10 mM glucose. Squares represent 7.5 mM glucose. Error bars are standard deviation (n = 3) (a) No AA (b) 20 µM AA (c) 40 µM AA

5.3.4 Glucose sensor embedded backplates with ascorbic acid to indicate hyperglycaemia

Following the solution experiments described in **Section 5.3.3** that used UV-Vis spectroscopic detection, the next step was to determine if a similar effect occurred when the AA modified sensor was incorporated into paper backplates. The concentrations of the sensor and AA optimised in the UV-Vis experiments were not directly translatable to the paper backplates due to the way the backplates were prepared. For example, as the backplates were dried following immersion in sensor solution, the addition of a small volume of glucose solution (1 µL) to the backplate modifies the concentration of both the sensor and AA. Therefore, the quantities of sensor and AA used to create the paper backplates had to be determined experimentally using the paper backplates, rather than using the concentrations determined in the UV-Vis experiments.

Sensor backplates were prepared as previously described (**Section 2.2.7**). To add the AA to the backplates, the paper squares embedded with the enzymes and TMB were allowed to dry for 60 mins at room temperature before being submerged in aqueous solutions of AA at the following concentrations – 0 mM, 2.5 mM, 5.0 mM, 7.5 mM, 10 mM, then dried at RT for 60 mins.

60 s was chosen as the measurement time to indicate hyperglycaemic conditions as this would provide results in a timely manner in a POC device. The backplates were tested using glucose concentrations of 10 mM and 7.5 mM as these were the key concentrations in hyperglycaemia (> 7.5 mM), therefore 1 µL aliquots of each glucose concentration in PBS were added to each backplate and a photograph of each was recorded after 60s (**Figure 5.16**)
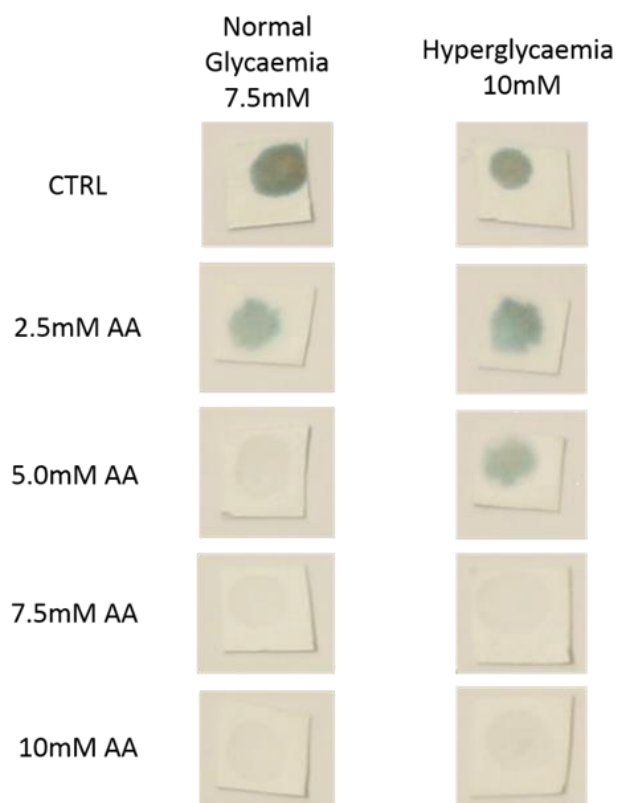
Figure 5.16 Photographs of paper backplates with embedded TMB and GOx/HRP sensor systems. A range of concentrations of AA (0 mM – 10 mM) were added to each backplate. Photographs were taken 60 s after 1 µL aliquots of either 10 mM or 7.5 mM of glucose were added to each backplate

After 60 s, the most intense colour change was observed in the control (0 mM AA) backplates for both concentrations of glucose. Similarly, both concentrations of glucose resulted in a colour change in the 2.5 mM AA backplates, although these were less intense than the control backplates. In contrast, only the hyperglycaemia concentration (10 mM) showed a colour change in the 5.0 mM AA backplate while the normal glycaemia (7.5 mM) gave no colour change. Notably, the colour change in the hyperglycaemia concentration in the 5.0 mM AA backplate was less intense than either the control or 2.5 mM AA backplates. No colour change was observed for either glucose concentration in the 7.5 mM or 10.0 mM AA backplates. These results can be explained through the inhibitory effect of the AA causing a longer lag phase before the TMB oxidation takes place. The more AA there is available to react with the hydrogen peroxide generated, the longer it takes for the TMB to become oxidised and any colour change to be realised. Based on the results shown in **Figure 5.16** above, 5mM AA containing sensor backplates produced the optimum result as no

colour was obtained within 60 sec in 7.5 mM glucose solution while a visibly apparent blue colour was observed for the 10 mM glucose solution, clearly differentiating between normal and hyperglycaemic concentrations of glucose. .

These 5.0 mM AA backplates were then tested using a wider range of glucose concentrations to mimic the clinically relevant measurements in diabetes. 4.0 mM and 7.5 mM glucose solutions were included to mark the lower and upper bounds of the normal range of glucose in the blood. 10 mM and 20 mM were used to represent hyperglycaemia. 1 μL aliquots of these glucose solutions were pipetted on to the backplates in triplicate and photographs were recorded at 60 s intervals for 5 mins. A representative image of each time point is shown in **Figure 5.17.**
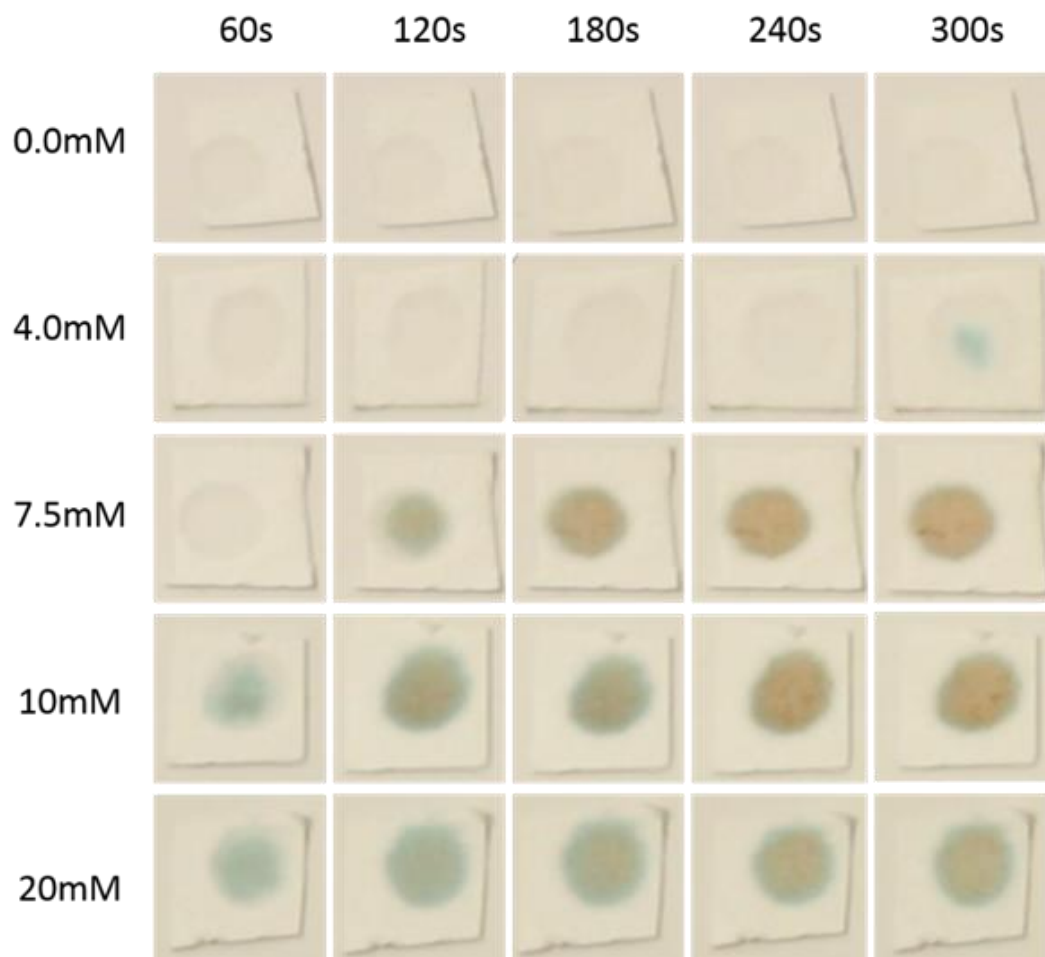
Figure 5.17 Photographs of sensor backplates containing TMB, GOx/HRP and 5 mM AA. Image taken at 60 s intervals after 1 μL aliquots of a range of concentrations of glucose were added to each backplate (0 mM – 20 mM)

For the 0 mM glucose, no colour change was generated over the course of the experiment. When 4.0 mM glucose was added no colour developed until a faint blue spot appeared after 300 s. The upper limit to normal glycaemia (7.5 mM glucose) caused no colour change at 60 s however at 120 s a coloured spot was generated that further developed throughout the remainder of the experiment. The first hyperglycaemia concentration of 10 mM glucose developed a coloured spot within 60 s that remained thereafter. Similarly, the, 20 mM glucose solution produced a coloured spot at 60 s that further developed until the end of the experiment.

As can be observed from the images in **Figure 5.17**, the colorimetric response to glucose produced both blue and yellow coloured spots depending on the progress of the reaction and as a consequence, the oxidised species generated. Therefore, quantifying blue chromaticity alone would not accurately reflect the reaction kinetics by proving a low reading for a reaction that has already progressed through the blue single oxidation product to the yellow di-oxidised product. By converting the images to grayscale, the intensity is less dependent on the type of colour but more by the intensity. Therefore, the images at each time point in **Figure 5.17** were converted to an 8-bit grayscale image using ImageJ[170] (**Figure 5.18a**). The mean gray values of the coloured areas of each backplate were then obtained and the intensity of colour was calculated using **Equation 5.1**:

$$\text{Intensity (a. u.)} = 255 - \text{Mean Gray Value} \quad \textbf{Equation 5.1}$$
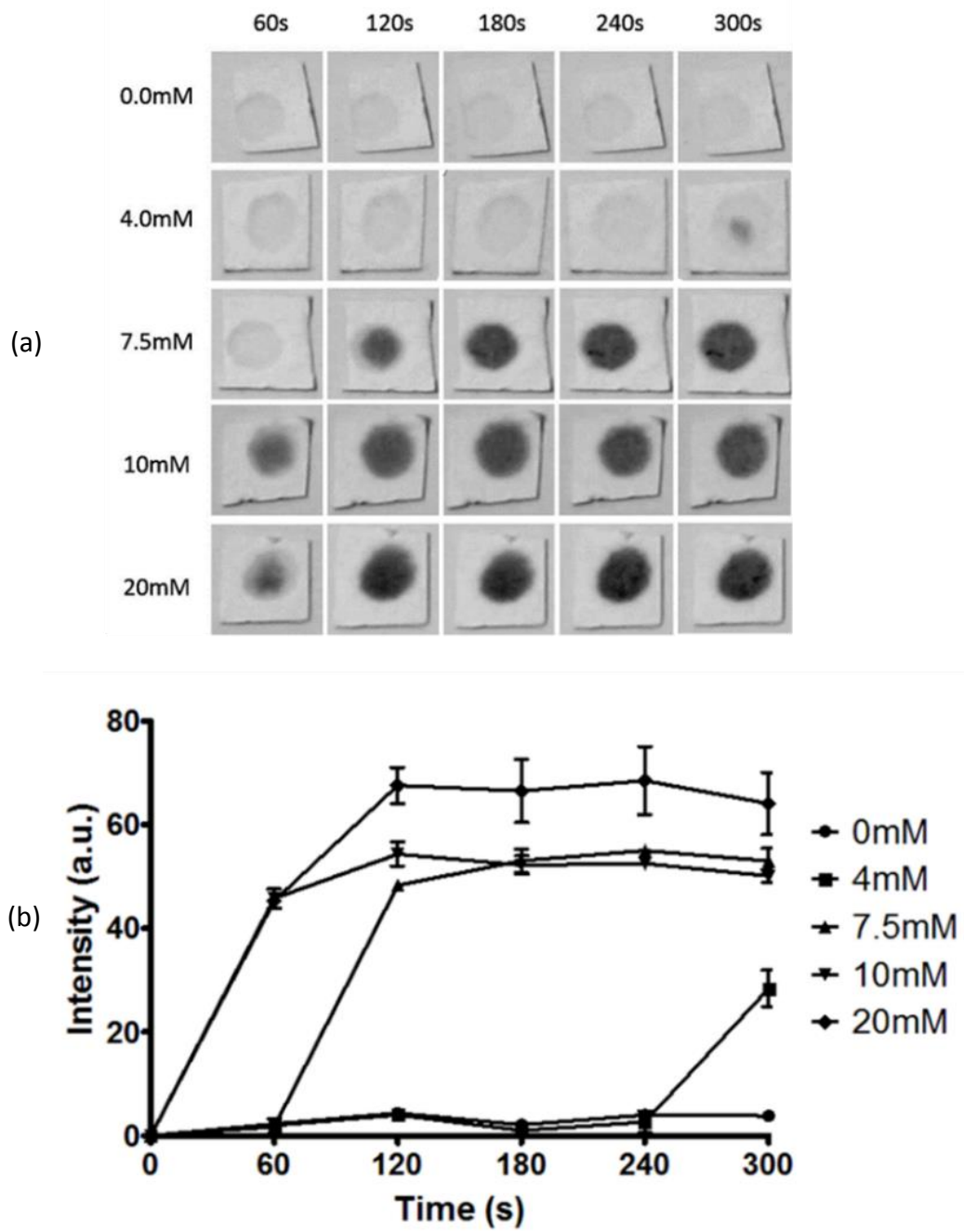
Figure 5.18 (a) Grayscale image of backplates from **Fig. 5.14** (b) Plot showing the intensity of the colour change in each backplate at 60 s intervals in response to addition of glucose solutions (0 mM – 20 mM)

As can be observed in **Figure 5.18b,** the intensities of the coloured spots correlated to what was observed by the naked eye with the 0, 4 and 7.5 mM glucose solution producing intensities that were low at 60s, while the 10 and 20 mM intensities 50-fold higher at the same time point. Again, these results suggest that using 5.0 mM AA within the backplate and identifying a time–point of 60 s following application of the MN should be appropriate to discriminate between normal and hyperglycaemic conditions.   The next step was to interface the AA containing sensor backplate with the suction-assisted MN device and determine how effective this would be at discriminating glucose concentrations following extraction of glucose from simulated ISF.

5.3.5 Incorporation of Ascorbic acid modified sensor backplate with hollow MN device for the Off-On detection of hyperglycaemia in simulated ISF.

Sensor backplates containing 5 mM AA were prepared as described in **Section 2.4.5** and fixed onto the base plate of the hollow metal MN. The MN-sensor construct was then incorporated within the flexible PDMS housing and sealed using adhesive as described in **Section 2.4.3**. The same *in vitro* model as described in **Section 5.3.2** was used to simulate penetrating the skin with thumb pressure used to provide vacuum and facilitate extraction of the glucose solutions via suction. The experiment was repeated in triplicate. Glucose concentrations (0 mM, 4 mM, 7.5mM, 10 mM and 20 mM) in PBS buffer were used as simulated ISF and in each case photographs were taken at 30 s intervals for 120 s. Representative images are shown in **Figure 5.19**.
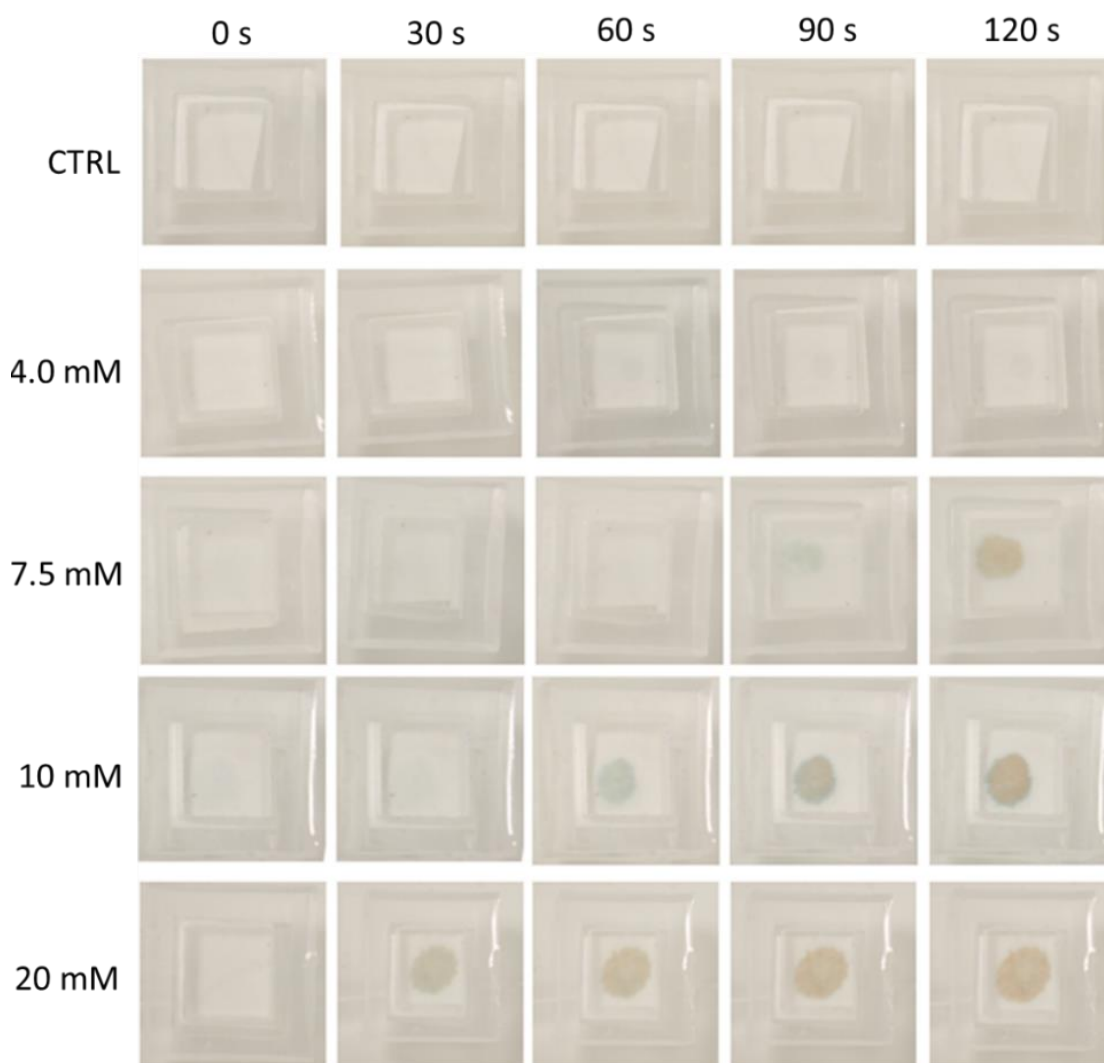
Figure 5.19 Photographs of sensor backplates in the assembled metal MN device after extracting glucose solutions (0 mM – 20 mM) at 30 s intervals

The MN device successfully extracted the glucose solutions though the metal needles and into the paper backplates as evidenced by the wetting observed on the sensor backplates. The MN that extracted the control solution (0 mM glucose) did not produce any colour on the backplate. Similarly, the 4.0 mM glucose solution did not produce a colour response within the time-scale of the experiment (120 s). The upper range of normal glycaemia (7.5 mM glucose) did not produce a colour change between 0 – 60 s, however a faint blue spot was observed at 90 s which further developed to a more visually apparent yellow colour at 120 s. The first hyperglycaemic concentration of 10 mM glucose caused no colour change at 30 s but the backplate had developed a strong colour change by 60 s, which increased in

intensity throughout the course of the experiment. The highest concentration of glucose (20 mM) caused the most rapid colour change, with a readily visible coloured spot observed at 30 s which had increased in intensity at 60 s and remained through to the end of the experiment. As before, the images were converted to 8 bit grayscale. The intensity at 60 s were measured and are shown in **Figure 5.20.**
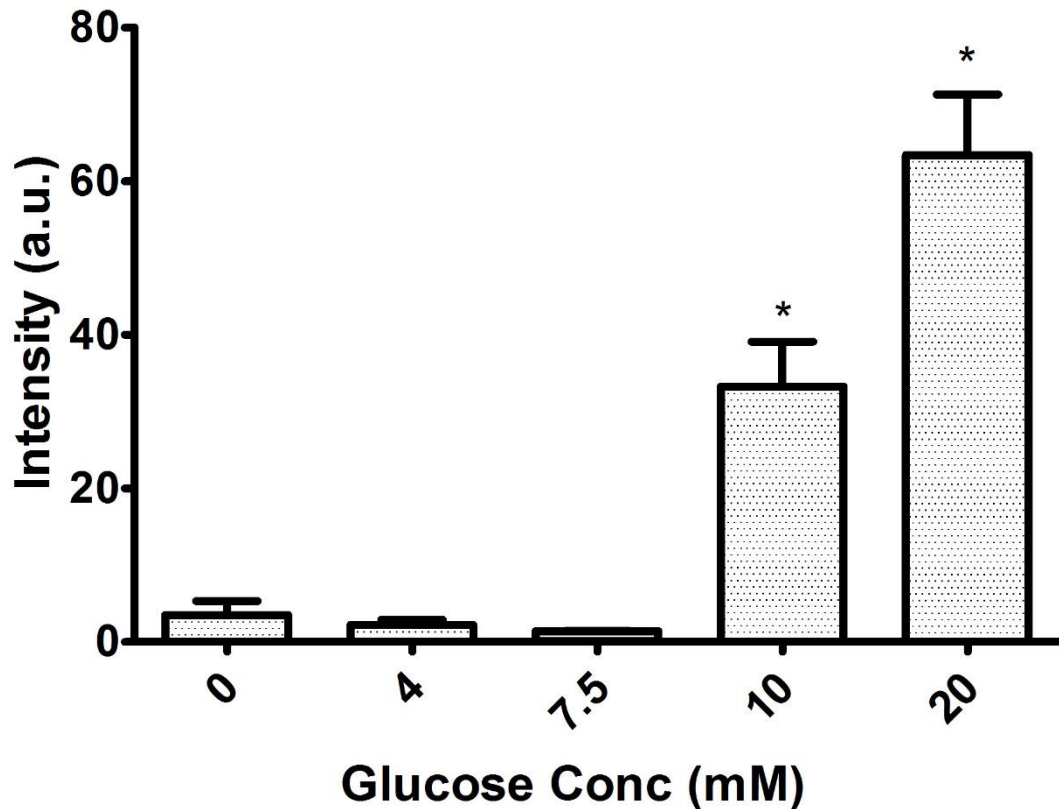
Figure 5.20 Plot showing the intensity of the colour change at 60 s in the sensor backplate in **Fig 5.19** in response to the extraction of glucose solution using assembled MN devices (0 mM – 20mM) (n=3) * denotes $p < 0.05$ for intensity generated between 10 mM and 0 mM control and 20 mM and 0 mM control

At 60 s, there was no significant difference between the grayscale values of the 0 mM, 4.0 mM and 7.5 mM glucose solutions. This demonstrated that normal glycaemic concentrations did not cause a colour change within 60 s in the assembled device. However, there was a significant increase in intensity for the 10 mM glucose solution when compared the 0 mM control ($p < 0.05$) and the increase in intensity for the 20 mM glucose when compared to the control ($p < 0.05$) at the same time point.

These results confirm that the device successfully indicates hyperglycaemic levels of glucose when the device is applied to the glucose solution for 60 s, with a colour change that is easily visible by the naked eye.

A MN device consisting of an in-plane array of hollow metal needles has demonstrated successful extraction of ISF in human volunteers[171]. The metal needles used in the fabrication of the device were also BD 32G pen needles as in this chapter, however the opposite longer bevelled end of the needles were used. This resulted in the production of MNs of 1000 μm, 1500 μm and 2000 μm height, which were substantially greater than the 600 μm MN reported in this chapter. The hollow MNs were fabricated using a CO2 laser cutter to control the MNs length and surrounding plastic housing. Glass capillary tubes were attached to the opposite end of each MN to act as a reservoir for the extracted ISF. Using a MN array consisting of five MNs in parallel, up to 16 μL of ISF was extracted from 14 human volunteers after a lag time of 30 - 120 s. The ISF collected in this study was used to determine transcriptome, proteome and exosome content and while it was acknowledged that ISF could be used to quantify glucose, no measurements have been reported using this device[172].

The crucial design aspect of this MN that allowed the successful ISF extraction was the concentric circular plastic ring of the housing around the opening of each MN. This concentric ring allowed the skin under the MN opening to remain uncompressed upon MN penetration. The authors assert that the pumping mechanism from the compression of the skin under the concentric ring of plastic to the uncompressed skin under the MN tip induced ISF to flow into the MN opening and into the reservoir. This design aspect could be incorporated in to the proposed device in this chapter if necessary to aid the extraction of ISF following *in vivo* investigations.

5.4 Conclusion

The results obtained in this Chapter demonstrate the use of a hollow metal MN device that can successfully extract simulated ISF *in vitro* and indicate the presence of hyperglycaemia within 60 s through a colour change. The detection of hyperglycaemia using a paper based sensor that is integrated into the MN device without the requirement for subsequent spectroscopic or chromatographic methods

is a novel approach. An additional novel aspect of this work was the use of AA to create a sensor that can discriminate relatively small differences in glucose levels through a visually apparent and non-ambiguous colour change using commercially available reagents without the need for complex synthetic routes and purification steps. The peroxide sensitive AA inhibited the formation of the coloured TMB product in physiologically normal concentrations of glucose (4 mM – 7.5 mM) within 60 s. However in higher concentrations, the generated peroxide overcame the action of AA and oxidised the TMB into its coloured product to give a colour change as an indication of hyperglycaemia (>7.5 mM glucose) at 60 s.

The device utilised stainless steel hollow needles due to their excellent mechanical properties and favourable biocompatibility profile, thus reducing the risk of MN fracture and skin sensitisation, often reported when using polymeric and silicon based MNs. Using 3D printing technology and silicone moulding, a PDMS attachment was coupled to the metal hollow MN that allowed the generation of a negative pressure upon the application of the MN that aided the extraction of ISF through the MN and into the paper based sensor backplate.

Chapter 6

6.0 Conclusions and Future Outlook

The work in this thesis has investigated MN based extraction and subsequent colorimetric determination of glucose within simulated ISF, in order to provide a minimally invasive method of indirectly monitoring glycaemia in the blood. Both hydrogel MNs and hollow MNs fabricated from methacrylate based polymers and stainless steel were used to provide a rapid means of extracting the simulated ISF and bringing it into contact with the glucose sensor. The enzyme based sensor was developed to generate a colour in response to glucose concentration and could be optimised to give a linear colorimetric response to quantify the concentration of glucose or provide an Off-On switch only sensitive to hyperglycaemic levels.

Crosslinked PMVE/MA MNs have previously shown the ability to extract ISF in human subjects and the work in **Chapter 3** has successfully demonstrated the integration of a sensor embedded backplate to these MNs that gives a visually apparent blue colour change in the presence of glucose. One of the main limitations of this approach in its current form was the time taken for the ISF absorb into the MN and move into the sensor backplate to interact with the sensor. It has been shown that using a paper based sensor backplate and increasing the length of the MN projections caused the response time to significantly decrease *in vitro*, however for use in a POC device future development should seek to lower the response time further.

A single hollow MN device in **Chapter 4** showed the ability to rapidly extract simulated ISF and move it into the sensor backplate within 5 s using capillary action *in vitro,* thus demonstrating a major improvement in the response time. The sensor was also optimised to provide a means of quantifying the concentration of glucose within the simulated ISF through the use of a digital camera. While larger differences in glucose concentrations, for example between hypoglycaemic conditions and hyperglycaemic conditions were visually apparent, further work could allow smaller changes to be measured using a smartphone camera and a calibration colour chart. Other development opportunities may include increasing the number of hollow MN

projections to produce a 2D array for superior mechanical robustness and to provide additional channels to extract ISF.

Finally, **Chapter 5** has detailed the production of a single metal hollow MN coupled to a flexible housing to provide ISF extraction through both capillary action and suction. The sensor was modified to give an Off On switching mechanism to identify hyperglycaemic concentrations in a visually apparent way that could find use to screen larger populations without the need from blood extraction or to alert diabetics to periods of hyperglycaemia that would then require administration of insulin or other hypoglycaemic agents. Future improvements could involve tailoring the sensor for the detection of hypoglycaemia. One potential method of achieving this would be to determine the time taken for the sensor to change colour when the glucose is in the hypoglycaemic range and use this as time point as a marker, i.e. if no colour change is visible before this time point then hypoglycaemia is present.

In summary, a MN based approach to measuring ISF analytes has enormous potential to avoid the current issues with blood sampling, such as contamination with blood borne pathogens, reduction of needle stick injuries and increasing patient compliance due to convenience and decreased pain. This work demonstrates promising methods to extract ISF rapidly and the integration of colorimetric sensors for glucose to aid in the development of POC devices.

7.0 Bibliography

1. Jatlow P, Costa JC. Chapter 4: An overview of diagnostic laboratory testing. In: Zaret BL, ed. Yale university school of medicine patient's guide to medical tests. Boston, MA.: Houghton Mifflin Company; 1997:62-72.

2. GVR. Blood testing market size, share & trends analysis report by test type (glucose, lipid, BUN, A1C, CRP, vitamin D, ALT, AST, thyroid stimulating hormone), by region, and segment forecasts, 2018 - 2024. Mar 2018;978-1-68038-897-8.

3. Paul DP, Ashworth S, Salyers L, Saldanha S, Coustasse A. Evaluation of glucose monitoring technologies for cost effective and quality control/management of diabetes. Proceedings of the Business and Health Administration Association Annual Conference. 2016.

4. NICE. Type 2 diabetes in adults: Management [CG28]. National Institute of Clinical Excellence. 2015.

5. Bantle JP, Thomas W. Glucose measurement in patients with diabetes mellitus with dermal interstitial fluid. J Lab Clin Med. 1997;130(4):436-441.

6. Fogh-Andersen N, Altura BM, Altura BT, Siggaard-Andersen O. Composition of interstitial fluid. Clin Chem. 1995;41(10):1522-1525.

7. Ye Y, Yu J, Wang C, et al. Microneedles integrated with pancreatic cells and synthetic glucose‐signal amplifiers for smart insulin delivery. Adv Mater. 2016;28(16):3115-3121.

8. Mo R, Jiang T, Di J, Tai W, Gu Z. Emerging micro-and nanotechnology based synthetic approaches for insulin delivery. Chem Soc Rev. 2014;43(10):3595-3629.

9. Chang H, Zheng M, Yu X, et al. A swellable microneedle patch to rapidly extract skin interstitial fluid for timely metabolic analysis. Adv Mater. 2017;29(37):1702243.

10. Caffarel-Salvador E, Brady AJ, Eltayib E, et al. Hydrogel-forming microneedle arrays allow detection of drugs and glucose in vivo: Potential for use in diagnosis and therapeutic drug monitoring. PloS one. 2015;10(12):e0145644.

11. Hajdu SI. The discovery of blood cells. Ann Clin Lab Sci. 2003;33(2):237-238.

12. Berger D. A brief history of medical diagnosis and the birth of the clinical laboratory. Part 1—Ancient times through the 19th century. MLO Med Lab Obs. 1999;31(7):28-30.

13. Hajdu SI. A note from history: The discovery of blood cells. Ann Clin Lab Sci. 2003;33(2):237-238.

14. Kay H. Plasma phosphatase in osteitis deformans and in other diseases of bone. Br J Exp Pathol. 1929;10(4):253.

15. Cherry IS, Crandall Jr LA. The specificity of pancreatic lipase: Its appearance in the blood after pancreatic injury. Am J Phys-Legacy Content. 1932;100(2):266-273.

16. Peitzman SJ. The flame photometer as engine of nephrology: A biography. Am J Kidney Dis. 2010;56(2):379-386.

17. MacIntyre I. Flame photometry. In: Adv Clin Chem. Vol 4. Elsevier; 1961:1-28.

18. Broughton P. Instrumentation—past and present. Ann Clin Biochem. 1974;11(1-6):146-149.

19. NHS. Reference costs 2014 to 2015. https://www.gov.uk/government/publications/nhs-reference-costs-2014-to-2015. Accessed 09/18.

20. Jatlow P, Costa JC. Chapter 4: An overview of diagnostic laboratory testing. In: Zaret BL, ed. Yale university school of medicine patient's guide to medical tests. Boston, MA.: Houghton Mifflin Company; 1997:62-72.

21. Mathers CD, Loncar D. Projections of global mortality and burden of disease from 2002 to 2030. PLoS med. 2006;3(11):e442.

22. NHS. Quality and outcomes framework - 2012-13. https://digital.nhs.uk/data-and-information/publications/statistical/quality-and-outcomes-framework-achievement-data/quality-and-outcomes-framework-2012-13 Accessed 09/18

23. Rodriguez-Calvo T, Ekwall O, Amirian N, Zapardiel-Gonzalo J, von Herrath MG. Increased immune cell infiltration of the exocrine pancreas: A possible contribution to the pathogenesis of type 1 diabetes. Diabetes. 2014;63(11):3880-3890.

24. Todd JA. Genetic control of autoimmunity in type 1 diabetes. Immunol Today. 1990;11:122-129.

25. WHO. Definition, diagnosis and classification of diabetes mellitus and its complications - Part 1. 1999;WHO/NCD/NCS/99.2.

26. Eiselein L, Schwartz HJ, Rutledge JC. The challenge of type 1 diabetes mellitus. ILAR journal. 2004;45(3):231-236.

27. Karvonen M, Tuomilehto J, Libman I, LaPorte R. A review of the recent epidemiological data on the worldwide incidence of type 1 (insulin-dependent) diabetes mellitus. Diabetologia. 1993;36(10):883-892.

28. Barnett A, Eff C, Leslie RD, Pyke D. Diabetes in identical twins. Diabetologia. 1981;20(2):87-93.

29. Wen L, Ley RE, Volchkov PY, et al. Innate immunity and intestinal microbiota in the development of type 1 diabetes. Nature. 2008;455(7216):1109.

30. Stene L, Rewers M. Immunology in the clinic review series; focus on type 1 diabetes and viruses: The enterovirus link to type 1 diabetes: Critical review of human studies. Clin Exp Immunol. 2012;168(1):12-23.

31. Harder T, Roepke K, Diller N, Stechling Y, Dudenhausen JW, Plagemann A. Birth weight, early weight gain, and subsequent risk of type 1 diabetes: Systematic review and meta-analysis. Am J Epidemiol. 2009;169(12):1428-1436.

32. Chatterjee S, Khunti K, Davies MJ. Type 2 diabetes. Lancet. 2017;389(10085):2239-2251.

33. Holt RI, Cockram C, Flyvbjerg A, Goldstein BJ. Textbook of diabetes. John Wiley & Sons; 2017.

34. Donath MY, Shoelson SE. Type 2 diabetes as an inflammatory disease. Nat Rev Immunol. 2011;11(2):98.

35. Kampmann U, Madsen LR, Skajaa GO, Iversen DS, Moeller N, Ovesen P. Gestational diabetes: A clinical update. World J Diabetes. 2015;6(8):1065-1072.

36. Bellamy L, Casas J, Hingorani AD, Williams D. Type 2 diabetes mellitus after gestational diabetes: A systematic review and meta-analysis. Lancet. 2009;373(9677):1773-1779.

37. Giacco F, Brownlee M. Oxidative stress and diabetic complications. Circ Res. 2010;107(9):1058-1070.

38. Jakus V, Rietbrock N. Advanced glycation end-products and the progress of diabetic vascular complications. Physiol Res. 2004;53(2):131-142.

39. Nishikawa T, Edelstein D, Du XL, et al. Normalizing mitochondrial superoxide production blocks three pathways of hyperglycaemic damage. Nature. 2000;404(6779):787.

40. Hietala K, Harjutsalo V, Forsblom C, Summanen P, Groop PH, FinnDiane Study Group. Age at onset and the risk of proliferative retinopathy in type 1 diabetes. Diabetes Care. 2010;33(6):1315-1319.

41. UK Prospective Diabetes Study (UKPDS) Group. Intensive blood-glucose control with sulphonylureas or insulin compared with conventional treatment and risk of complications in patients with type 2 diabetes (UKPDS 33). Lancet. 1998;352(9131):837-853.

42. Holl R, Lang GE, Grabert M, Heinze E, Lang G, Debatin K. Diabetic retinopathy in pediatric patients with type-1 diabetes: Effect of diabetes duration, prepubertal and pubertal onset of diabetes, and metabolic control. J Pediatr. 1998;132(5):790-794.

43. Diabetic Retinopathy Study Research Group. Four risk factors for severe visual loss in diabetic retinopathy. the third report from the diabetic retinopathy study. Arch Ophthalmol. 1979;97:654-655.

44. Ritz E, Orth SR. Nephropathy in patients with type 2 diabetes mellitus. N Engl J Med. 1999;341(15):1127-1133.

45. Vithian K, Hurel S. Microvascular complications: Pathophysiology and management. Clin Med (Lond). 2010;10(5):505-509.

46. Tesfaye S, Boulton AJ, Dickenson AH. Mechanisms and management of diabetic painful distal symmetrical polyneuropathy. Diabetes Care. 2013;36(9):2456-2465.

47. Vas PR, Sharma S, Rayman G. Distal sensorimotor neuropathy: Improvements in diagnosis. Rev Diabet Stud. 2015;12(1-2):29-47.

48. Boulton A. The diabetic foot: From art to science. the 18th camillo golgi lecture. Diabetologia. 2004;47(8):1343-1353.

49. Shojaiefard A, Khorgami Z, Larijani B. Independent risk factors for amputation in diabetic foot. Int J Diabetes Dev Ctries. 2008;28(2):32-37.

50. Skyler JS, Bergenstal R, Bonow RO, et al. Intensive glycemic control and the prevention of cardiovascular events: Implications of the ACCORD, ADVANCE, and VA diabetes trials: A position statement of the american diabetes association and a scientific statement of the american college of cardiology foundation and the american heart association. J Am Coll Cardiol. 2009;53(3):298-304.

51. Holman RR, Paul SK, Bethel MA, Matthews DR, Neil HAW. 10-year follow-up of intensive glucose control in type 2 diabetes. N Engl J Med. 2008;359(15):1577-1589.

52. Lusis AJ. Atherosclerosis. Nature. 2000;407(6801):233-41.

53. Conti P, Shaik-Dasthagirisaeb Y. Atherosclerosis: A chronic inflammatory disease mediated by mast cells. Cent Eur J Immunol. 2015;40(3):380-386.

54. Parks BW, Lusis AJ. Macrophage accumulation in atherosclerosis. N Engl J Med. 2013;369(24):2352-2353.

55. Beckman JA, Creager MA, Libby P. Diabetes and atherosclerosis: Epidemiology, pathophysiology, and management. JAMA. 2002;287(19):2570-2581.

56. Haffner SM, Lehto S, Rönnemaa T, Pyörälä K, Laakso M. Mortality from coronary heart disease in subjects with type 2 diabetes and in nondiabetic subjects with and without prior myocardial infarction. N Engl J Med. 1998;339(4):229-234.

57. Kohnert K, Augstein P, Heinke P, et al. Chronic hyperglycemia but not glucose variability determines HbA1c levels in well-controlled patients with type 2 diabetes. Diabetes Res Clin Pract. 2007;77(3):420-426.

58. Bunn HF, Haney DN, Kamin S, Gabbay KH, Gallop PM. The biosynthesis of human hemoglobin A1c. slow glycosylation of hemoglobin in vivo. J Clin Invest. 1976;57(6):1652-1659.

59. Seaman C, Wyss S, Piomelli S. The decline in energetic metabolism with aging of the erythrocyte and its relationship to cell death. Am J Hematol. 1980;8(1):31-42.

60. Koenig RJ, Peterson CM, Kilo C, Cerami A, Williamson JR. Hemoglobin AIc as an indicator of the degree of glucose intolerance in diabetes. Diabetes. 1976;25(3):230-232.

61. NICE. Type 1 diabetes in adults: Diagnosis and management [NG17].

National Institute of Clinical Excellence. 2015.

62. Young JK, Ellison JM, Marshall R. Performance evaluation of a new blood glucose monitor that requires no coding: The OneTouch® vita™ system. J Diabetes Sci Technol. 2008;2(5):814-818.

63. Bankar SB, Bule MV, Singhal RS, Ananthanarayan L. Glucose oxidase—an overview. Biotechnol Adv. 2009;27(4):489-501.

64. Clarke S, Foster J. A history of blood glucose meters and their role in self-monitoring of diabetes mellitus. Br J Biomed Sci. 2012;69(2):83-93.

65. Tang Z, Lee JH, Louie RF, Kost GJ. Effects of different hematocrit levels on glucose measurements with handheld meters for point-of-care testing. Arch Pathol Lab Med. 2000;124(8):1135-1140.

66. Hortensius J, Kars MC, Wierenga WS, Kleefstra N, Bilo HJ, van der Bijl, Jaap J. Perspectives of patients with type 1 or insulin-treated type 2 diabetes on self-monitoring of blood glucose: A qualitative study. BMC Pub Health. 2012;12(1):167.

67. Tong WT, Vethakkan SR, Ng CJ. Why do some people with type 2 diabetes who are using insulin have poor glycaemic control? A qualitative study. BMJ Open. 2015;5(1):e006407-2014-006407.

68. Ramchandani N, Cantey-Kiser JM, Alter CA, et al. Self-reported factors that affect glycemic control in college students with type 1 diabetes. Diabetes Educ. 2000;26(4):656-666.

69. Moström P, Ahlén E, Imberg H, Hansson P, Lind M. Adherence of self-monitoring of blood glucose in persons with type 1 diabetes in Sweden. BMJ Open Diabetes Res Care. 2017;5(1):e000342.

70. Keenan DB, Mastrototaro JJ, Voskanyan G, Steil GM. Delays in minimally invasive continuous glucose monitoring devices: A review of current technology. J Diabetes Sci Technol. 2009;3(5):1207-1214.

71. Klonoff DC. Noninvasive blood glucose monitoring. Diabetes Care. 1997;20(3):433-437.

72. Gerstel MSP, V.A., Inventor. Drug delivery device. US Patent 1976.

73. Henry S, McAllister DV, Allen MG, Prausnitz MR. Microfabricated microneedles: A novel approach to transdermal drug delivery. J Pharm Sci. 1998;87(8):922-925.

74. Tuan-Mahmood T, McCrudden MT, Torrisi BM, et al. Microneedles for intradermal and transdermal drug delivery. Eur J Pharm Sci. 2013;50(5):623-637.

75. Donnelly RF, Singh TRR, Morrow DI, Woolfson AD. Microneedle-mediated transdermal and intradermal drug delivery. John Wiley & Sons; 2012.

76. Amsden B, Goosen M. Transdermal delivery of peptide and protein drugs: An overview. AIChE J. 1995;41(8):1972-1997.

77. McAllister DV, Wang PM, Davis SP, et al. Microfabricated needles for transdermal delivery of macromolecules and nanoparticles: Fabrication methods and transport studies. Proc Natl Acad Sci U S A. 2003;100(24):13755-13760.

78. Oh J, Park H, Do K, et al. Influence of the delivery systems using a microneedle array on the permeation of a hydrophilic molecule, calcein. Eur J Pharm Biopharm. 2008;69(3):1040-1045.

79. Wermeling DP, Banks SL, Hudson DA, et al. Microneedles permit transdermal delivery of a skin-impermeant medication to humans. Proc Natl Acad Sci U S A. 2008;105(6):2058-2063.

80. Ikejiri A, Ito Y, Naito S, Takada K. Two-and three-layered dissolving microneedles for transcutaneous delivery of model vaccine antigen in rats. J Biomat Nanobiotech. 2012;3(03):325.

81. Koutsonanos DG, del Pilar Martin M, Zarnitsyn VG, et al. Transdermal influenza immunization with vaccine-coated microneedle arrays. PloS one. 2009;4(3):e4773.

82. Cormier M, Johnson B, Ameri M, et al. Transdermal delivery of desmopressin using a coated microneedle array patch system. J Controlled Release. 2004;97(3):503-511.

83. Daddona PE, Matriano JA, Mandema J, Maa Y. Parathyroid hormone (1-34)-coated microneedle patch system: Clinical pharmacokinetics and pharmacodynamics for treatment of osteoporosis. Pharm Res. 2011;28(1):159-165.

84. Chabri F, Bouris K, Jones T, et al. Microfabricated silicon microneedles for nonviral cutaneous gene delivery. Br J Dermatol. 2004;150(5):869-877.

85. Coulman SA, Barrow D, Anstey A, et al. Minimally invasive cutaneous delivery of macromolecules and plasmid DNA via microneedles. Curr drug deliv. 2006;3(1):65-75.

86. Lee JW, Choi S, Felner EI, Prausnitz MR. Dissolving microneedle patch for transdermal delivery of human growth hormone. Small. 2011;7(4):531-539.

87. Lahiji SF, Dangol M, Jung H. A patchless dissolving microneedle delivery system enabling rapid and efficient transdermal drug delivery. Scientific reports. 2015;5:7914.

88. Lee K, Lee CY, Jung H. Dissolving microneedles for transdermal drug administration prepared by stepwise controlled drawing of maltose. Biomaterials. 2011;32(11):3134-3140.

89. Chen M, Ling M, Lai K, Pramudityo E. Chitosan microneedle patches for sustained transdermal delivery of macromolecules. Biomacromolecules. 2012;13(12):4022-4031.

90. Chu LY, Choi S, Prausnitz MR. Fabrication of dissolving polymer microneedles for controlled drug encapsulation and delivery: Bubble and pedestal microneedle designs. J Pharm Sci. 2010;99(10):4228-4238.

91. Chu LY, Prausnitz MR. Separable arrowhead microneedles. J Controlled Release. 2011;149(3):242-249.

92. González-Vázquez P, Larrañeta E, McCrudden MT, et al. Transdermal delivery of gentamicin using dissolving microneedle arrays for potential treatment of neonatal sepsis. J Controlled Release. 2017;265:30-40.

93. Prins JM, Buller HR, Speelman P, Kuijper E, Tange R. Once versus thrice daily gentamicin in patients with serious infections. Lancet. 1993;341(8841):335-339.

94. Ling M, Chen M. Dissolving polymer microneedle patches for rapid and efficient transdermal delivery of insulin to diabetic rats. Acta biomaterialia. 2013;9(11):8952-8961.

95. Ganji F, Vasheghani FS, Vasheghani FE. Theoretical description of hydrogel swelling: A review. Iran Polymer J. 2010.

96. Yang S, Feng Y, Zhang L, Chen N, Yuan W, Jin T. A scalable fabrication process of polymer microneedles. Int J Nanomed. 2012;7:1415.

97. McGrath J, Eady R, Pope F. Anatomy and organization of human skin. Rook's Textbook of Dermatology. 2004;3:1-15.

98. Barker JN, Griffiths C, Nickoloff BJ, Mitra R, Dixit VM. Keratinocytes as initiators of inflammation. Lancet. 1991;337(8735):211-214.

99. Hill MA. Embryology Adult epidermis histology 02. https://embryology.med.unsw.edu.au/embryology/index.php/File:Adult_epidermis _histology_02.jpg. Updated 2012. Accessed 08/18, 2018.

100. Losquadro WD. Anatomy of the skin and the pathogenesis of nonmelanoma skin cancer. Facial Plast Surg Clin North Am. 2017;25(3):283-289.

101. Chapman S, Walsh A. Desmosomes, corneosomes and desquamation. an ultrastructural study of adult pig epidermis. Arch Dermatol Res. 1990;282(5):304-310.

102. Mclafferty E, Hendry C, Farley A. The integumentary system: Anatomy, physiology and function of skin. Nursing Standard (through 2013). 2012;27(3):35.

103. Tortora GJ, Derrickson BH. Principles of anatomy and physiology. John Wiley & Sons; 2008.

104. Chomiczewska D, Trznadel-Budzko E, Kaczorowska A, Rotsztejn H. The role of langerhans cells in the skin immune system. Pol Merkur Lekarski. 2009;26(153):173-177.

105. Lucarz A, Brand G. Current considerations about merkel cells. Eur J Cell Biol. 2007;86(5):243-251.

106. Ashok NG, Ramasubramanian A. Merkel cells: A review on role of merkel cells in histology and disease. Int J Orofacial Res. 2017;2(2):45.

107. Yousef H, Sharma S. Anatomy, skin (integument), epidermis. In: StatPearls. Treasure Island (FL): StatPearls Publishing LLC; 2018. NBK470464

108. Hamelin ND, Wong AK. Flaps and skin grafts. In: Hamm RL, ed. Text and atlas of wound diagnosis and treatment. McGraw-Hill; 2015:255-280.

109. Imanishi N, Kishi K, Chang H, Nakajima H, Aiso S. Three‑dimensional venous anatomy of the dermis observed using stereography. J Anat. 2008;212(5):669-673.

110. Melzack R. The short-form McGill pain questionnaire. Pain. 1987;30(2):191-197.

111. Aitken RC. Measurement of feelings using visual analogue scales.

Proc Roy Soc Med. 1969;62(10):989-993.

112. Hawker GA, Mian S, Kendzerska T, French M. Measures of adult pain: Visual analog scale for pain (vas pain), numeric rating scale for pain (nrs pain), mcgill pain questionnaire (mpq), short‐form mcgill pain questionnaire (sf‐mpq), chronic pain grade scale (cpgs), short form‐36 bodily pain scale (sf‐36 bps), and measure of intermittent and constant osteoarthritis pain (icoap). Arthritis Care Res. 2011;63(S11):S240-S252

113. Kaushik S, Hord AH, Denson DD, et al. Lack of pain associated with microfabricated microneedles. Anesth & Analg. 2001;92(2):502-504.

114. Cheung K, Han T, Das DB. Effect of force of microneedle insertion on the permeability of insulin in skin. J Diabetes Sci Technol. 2014;8(3):444-452.

115. Bal SM, Caussin J, Pavel S, Bouwstra JA. In vivo assessment of safety of microneedle arrays in human skin. Eur J Pharm Sci. 2008;35(3):193-202.

116. Haq M, Smith E, John DN, et al. Clinical administration of microneedles: Skin puncture, pain and sensation. Biomed Microdevices. 2009;11(1):35-47.

117. Van Damme P, Oosterhuis-Kafeja F, Van der Wielen M, Almagor Y, Sharon O, Levin Y. Safety and efficacy of a novel microneedle device for dose sparing intradermal influenza vaccination in healthy adults. Vaccine. 2009;27(3):454-459.

118. Smart WH, Subramanian K. The use of silicon microfabrication technology in painless blood glucose monitoring. Diabetes Technol Ther. 2000;2(4):549-559.

119. Kermani SK, Khatony A, Jalali R, Rezaei M, Abdi A. Accuracy and precision of measured blood sugar values by three glucometers compared to the standard technique. J Clin Diagn Res. 2017;11(4):OC05-OC08.

120. Hu X, Yu J, Qian C, et al. H2O2-responsive vesicles integrated with transcutaneous patches for glucose-mediated insulin delivery. ACS nano. 2017;11(1):613-620.

121. Yu J, Qian C, Zhang Y, et al. Hypoxia and H2O2 dual-sensitive vesicles for enhanced glucose-responsive insulin delivery. Nano letters. 2017;17(2):733-739.

122. Wang J, Ye Y, Yu J, et al. Core–Shell microneedle gel for self-regulated insulin delivery. ACS nano. 2018;12(3):2466-2473.

123. Saravanakumar G, Kim J, Kim WJ. Reactive‐Oxygen‐Species‐Responsive drug delivery systems: Promises and challenges. Adv Sci. 2017;4(1):1600124.

124. Xu B, Jiang G, Yu W, et al. H 2 O 2-responsive mesoporous silica nanoparticles integrated with microneedle patches for the glucose-monitored transdermal delivery of insulin. J Mat Chem B. 2017;5(41):8200-8208.

125. Mukerjee E, Collins S, Isseroff R, Smith R. Microneedle array for transdermal biological fluid extraction and in situ analysis. Sens Actuators A: Phys. 2004;114(2-3):267-275.

126. Sakaguchi K, Hirota Y, Hashimoto N, et al. A minimally invasive system for glucose area under the curve measurement using interstitial fluid extraction technology: Evaluation of the accuracy and usefulness with oral glucose tolerance tests in subjects with and without diabetes. Diabetes Technol Ther. 2012;14(6):485-491.

127. Caffarel-Salvador E, Brady AJ, Eltayib E, et al. Hydrogel-forming microneedle arrays allow detection of drugs and glucose in vivo: Potential for use in diagnosis and therapeutic drug monitoring. PloS one. 2015;10(12):e0145644.

128. Romanyuk AV, Zvezdin VN, Samant P, Grenader MI, Zemlyanova M, Prausnitz MR. Collection of analytes from microneedle patches. Anal Chem. 2014;86(21):10520-10523.

129. Chang H, Zheng M, Yu X, et al. A swellable microneedle patch to rapidly extract skin interstitial fluid for timely metabolic analysis. Adv Mater. 2017;29(37):1702243.

130. Hachet E, Van den Berghe H, Bayma E, Block MR, Auzély-Velty R. Design of biomimetic cell-interactive substrates using hyaluronic acid hydrogels with tunable mechanical properties. Biomacromolecules. 2012;13(6):1818-1827.

131. Abbott Diabetes Care Inc. How does the freestyle libre system measure my glucose? . https://freestylediabetes.co.uk/freestyle-thinking/post/FreeStyle-Libre-system-measure. Updated 20172019.

132. Bolinder J, Antuna R, Geelhoed-Duijvestijn P, Kröger J, Weitgasser R. Novel glucose-sensing technology and hypoglycaemia in type 1 diabetes: A multicentre, non-masked, randomised controlled trial. Lancet. 2016;388(10057):2254-2263

133. Workgroup on Hypoglycemia, American Diabetes Association. Defining and reporting hypoglycemia in diabetes: A report from the american diabetes association workgroup on hypoglycemia. Diabetes Care. 2005;28(5):1245-1249.

134. Bailey T, Bode BW, Christiansen MP, Klaff LJ, Alva S. The performance and usability of a factory-calibrated flash glucose monitoring system. Diabetes Technol Ther. 2015;17(11):787-794.

135. Crabtree TS, Sathyapalan T, Wilmot E. Freestyle libre: Available on the NHS? Brit J Diabetes. 2018;18(1):3-6.

136. Stout PJ, Peled N, Erickson BJ, Hilgers ME, Racchini JR, Hoegh TB. Comparison of glucose levels in dermal interstitial fluid and finger capillary blood Diabetes Technol Ther. 2001;3(1):81-90.

137. Bailey T, Bode BW, Christiansen MP, Klaff LJ, Alva S. The performance and usability of a factory-calibrated flash glucose monitoring system. Diabetes Technol Ther. 2015;17(11):787-794.

138. Donnelly RF, Singh TRR, Garland MJ, et al. Hydrogel‐forming microneedle arrays for enhanced transdermal drug delivery. Adv Funct Mater. 2012;22(23):4879-4890.

139. Donnelly RF, McCrudden MT, Alkilani AZ, et al. Hydrogel-forming microneedles prepared from "super swelling" polymers combined with lyophilised wafers for transdermal drug delivery. PLoS One. 2014;9(10):e111547.

140. Leonards JR. Evaluation of enzyme tests for urinary glucose. J Am Med Assoc. 1957;163(4):260-260.

141. Josephy PD, Eling T, Mason RP. The horseradish peroxidase-catalyzed oxidation of 3,5,3',5'-tetramethylbenzidine. free radical and charge-transfer complex intermediates. J Biol Chem. 1982;257(7):3669-3675.

142. Lhernould MS, Deleers M, Delchambre A. Hollow polymer microneedles array resistance and insertion tests. Int J Pharm. 2015;480(1-2):152-157.

143. Larrañeta E, Moore J, Vicente-Pérez EM, et al. A proposed model membrane and test method for microneedle insertion studies. Int J Pharm. 2014;472(1-2):65-73.

144. McCarron PA, Woolfson AD, Donnelly RF, Andrews GP, Zawislak A, Price JH. Influence of plasticizer type and storage conditions on properties of poly (methyl vinyl ether‐co‐maleic anhydride) bioadhesive films. J Appl Polym Sci. 2004;91(3):1576-1589.

145. Liana DD, Raguse B, Gooding JJ, Chow E. Recent advances in paper-based sensors. Sensors. 2012;12(9):11505-11526.

146. Gillespie T, Johnson T. The penetration of aqueous surfactant solutions and non-newtonian polymer solutions into paper by capillary action. J Colloid Interface Sci. 1971;36(2):282-285.

147. Larrañeta E, Henry M, Irwin NJ, Trotter J, Perminova AA, Donnelly RF. Synthesis and characterization of hyaluronic acid hydrogels crosslinked using a solvent-free process for potential biomedical applications. Carbohydr Polym. 2018;181:1194-1205.

148. Demir YK, Metin AÜ, Şatıroğlu B, Solmaz ME, Kayser V, Mäder K. Poly (methyl vinyl ether-co-maleic acid)–Pectin based hydrogel-forming systems: Gel, film, and microneedles. Eur J Pharm Biopharm. 2017;117:182-194.

149. Mansoor I, Liu Y, Häfeli U, Stoeber B. Arrays of hollow out-of-plane microneedles made by metal electrodeposition onto solvent cast conductive polymer structures. J Micromech Microengineering. 2013;23(8):085011.

150. Ranamukhaarachchi SA, Padeste C, Dübner M, Häfeli UO, Stoeber B, Cadarso VJ. Integrated hollow microneedle-optofluidic biosensor for therapeutic drug monitoring in sub-nanoliter volumes. Scientific reports. 2016;6:29075.

151. Liu L, Kai H, Nagamine K, Ogawa Y, Nishizawa M. Porous polymer microneedles with interconnecting microchannels for rapid fluid transport. RSC Adv. 2016;6(54):48630-48635.

152. Olatunji O, Das DB, Garland MJ, Belaid L, Donnelly RF. Influence of array interspacing on the force required for successful microneedle skin penetration: Theoretical and practical approaches. J Pharm Sci. 2013;102(4):1209-1221.

153. Ochoa M, Zhou J, Rahimi R, Badwaik V, Thompson D, Ziaie B. Rapid 3D-print-and-shrink fabrication of biodegradable microneedles with complex geometries. Bioengineering. 2015:1251-1254.

154. Farias C, Lyman R, Hemingway C, et al. Three-dimensional (3D) printed microneedles for microencapsulated cell extrusion. Bioengineering. 2018;5(3):59.

155. Luzuriaga MA, Berry DR, Reagan JC, Smaldone RA, Gassensmith JJ. Biodegradable 3D printed polymer microneedles for transdermal drug delivery. Lab Chip. 2018;18(8):1223-1230.

156. Strambini L, Longo A, Scarano S, et al. Self-powered microneedle-based biosensors for pain-free high-accuracy measurement of glycaemia in interstitial fluid. Biosens Bioelect. 2015;66:162-168.

157. Dardano P, Caliò A, Di Palma V, Bevilacqua M, Di Matteo A, De Stefano L. Multianalyte biosensor patch based on polymeric microneedles. Convegno Nazionale Sensori. 2016:73-81.

158. Soni A, Jha SK. A paper strip based non-invasive glucose biosensor for salivary analysis. Biosens Bioelect. 2015;67:763-768.

159. O'Mahony C. Structural characterization and in-vivo reliability evaluation of silicon microneedles. Biomed Microdevices. 2014;16(3):333-343.

160. Finley J, Knabb J. Cutaneous silica granuloma. Plast Reconstr Surg. 1982;69(2):340-343.

161. Salmon JK, Armstrong CA, Ansel JC. The skin as an immune organ. West J Med. 1994;160(2):146-152.

162. Geetha M, Singh AK, Asokamani R, Gogia AK. Ti based biomaterials, the ultimate choice for orthopaedic implants–a review. Prog Mater Sci. 2009;54(3):397-425.

163. Donnelly RF, Singh TRR, Tunney MM, et al. Microneedle arrays allow lower microbial penetration than hypodermic needles in vitro. Pharm Res. 2009;26(11):2513-2522.

164. Prausnitz MR, Mikszta JA, Cormier M, Andrianov AK. Microneedle-based vaccines. In: Vaccines for pandemic influenza. Springer; 2009:369-393.

165. Rotblatt MD, Koda-Kimble MA. Review of drug interference with urine glucose tests. Diabetes Care. 1987;10(1):103-110.

166. Badrick TC, Campbell B. Effects of intravenous infusion of ascorbate on common clinical chemistry tests. Clin Chem. 1992;38(10):2160.

167. White-Stevens RH. Interference by ascorbic acid in test systems involving peroxidase. I. reversible indicators and the effects of copper, iron, and mercury. Clin Chem. 1982;28(4 Pt 1):578-588.

168. Martinello F, da Silva EL. Mechanism of ascorbic acid interference in biochemical tests that use peroxide and peroxidase to generate chromophore. Clinica Chimica Acta. 2006;373(1-2):108-116.

169. Samant PP, Prausnitz MR. Mechanisms of sampling interstitial fluid from skin using a microneedle patch. Proc Nat Acad Sci. 2018:201716772.

170. Deutsch JC. Ascorbic acid oxidation by hydrogen peroxide. Anal Biochem. 1998;255(1):1-7.

171. National Institutes of Health. ImageJ analyze menu. https://imagej.nih.gov/ij/docs/menus/analyze.html. Accessed 09/15, 2018.

171. Miller PR, Taylor RM, Tran BQ, et al. Extraction and biomolecular analysis of dermal interstitial fluid collected with hollow microneedles. Nat Commun Bio. 2018;1(1):173.

172. Taylor RM, Miller PR, Ebrahimi P, Polsky R, Baca JT. Minimally-invasive, microneedle-array extraction of interstitial fluid for comprehensive biomedical applications: Transcriptomics, proteomics, metabolomics, exosome research, and biomarker identification. Lab Anim. 2018:0023677218758801.